



**HAL**  
open science

## Carboniferous high- P metamorphism and deformation in the Belledonne Massif (Western Alps)

Jean-baptiste Jacob, Stéphane Guillot, Daniela Rubatto, Emilie Janots,  
Jérémie Melleton, Michel Faure

► **To cite this version:**

Jean-baptiste Jacob, Stéphane Guillot, Daniela Rubatto, Emilie Janots, Jérémie Melleton, et al..  
Carboniferous high- P metamorphism and deformation in the Belledonne Massif (Western Alps).  
Journal of Metamorphic Geology, 2021, 39 (8), pp.1009-1044. 10.1111/jmg.12600 . hal-03746434

**HAL Id: hal-03746434**

**<https://brgm.hal.science/hal-03746434v1>**

Submitted on 5 Aug 2022

**HAL** is a multi-disciplinary open access archive for the deposit and dissemination of scientific research documents, whether they are published or not. The documents may come from teaching and research institutions in France or abroad, or from public or private research centers.

L'archive ouverte pluridisciplinaire **HAL**, est destinée au dépôt et à la diffusion de documents scientifiques de niveau recherche, publiés ou non, émanant des établissements d'enseignement et de recherche français ou étrangers, des laboratoires publics ou privés.

Corresponding author email id: jean-baptiste.jacob@univ-grenoble-alpes.fr

# Carboniferous high pressure metamorphism and deformation in the Belledonne Massif (Western Alps)

Jacob Jean-Baptiste<sup>1</sup>, Guillot Stéphane<sup>1</sup>, Rubatto Daniela<sup>2,3</sup>, Janots Emilie<sup>1</sup>, Melleton Jérémie<sup>3</sup>, Faure Michel<sup>4</sup>

<sup>1</sup>Univ. Grenoble Alpes, Univ. Savoie Mont Blanc, CNRS, IRD, Univ. Gustave Eiffel, ISTerre, 38000 Grenoble, France

<sup>2</sup>Institute of Geological Sciences, University of Bern, Baltzerstrasse 1-3, CH-3012 Bern, Switzerland

<sup>3</sup>Institut des Sciences de La Terre, University of Lausanne, CH-1015 Lausanne, Switzerland.

<sup>4</sup>Bureau de Recherches Géologiques et Minières, 3 avenue Claude-Guillemin, BP 36009, 45060 Orléans Cedex 2, France

<sup>5</sup>Institut des Sciences de la Terre d'Orléans, Université d'Orléans, CNRS, 45071 Orléans Cedex 2, France

Short running title : Variscan HP metamorphism the western Alps

This article has been accepted for publication and undergone full peer review but has not been through the copyediting, typesetting, pagination and proofreading process, which may lead to differences between this version and the [Version of Record](#). Please cite this article as [doi: 10.1111/jmg.12600](https://doi.org/10.1111/jmg.12600)

This article is protected by copyright. All rights reserved

## ABSTRACT

The age and P-T conditions of Variscan high pressure (HP) metamorphism in the Paleozoic basement of the western Alps remain poorly constrained, but is nevertheless crucial to build a consistent tectonic scenario for the southeastern domain of the Variscan Belt. We report here the results of a structural, petrological, thermobarometric and geochronological investigation of an eclogite-bearing unit exposed in the northeastern part of the Belledonne Massif (France). This unit is mostly composed of metasediments, that are locally migmatized and contain decameter-to-hectometer-scale lenses of orthogneiss and amphibolites. SIMS U-Pb dating of magmatic zircon cores in two retrogressed ecogites yields ages at  $456\pm 4$  Ma and  $448\pm 6$  Ma, which are interpreted to date the emplacement of the magmatic protoliths. The peak pressure stage in the retrogressed ecogites is estimated to be  $>1.4$  GPa at  $690\text{--}740^\circ\text{C}$ , and was followed by decompression from 1.4 to ca. 1.0 GPa at  $700\text{--}800^\circ\text{C}$ . By contrast, the investigated migmatitic metasediment does not present any trace of HP metamorphism, but instead preserves prograde evolution from sub-solidus conditions (ca. 0.8–1.1 GPa and  $600\text{--}700^\circ\text{C}$ ) to supra-solidus conditions (1.1–1.4 GPa and  $700\text{--}780^\circ\text{C}$ ). A later stage of retrogression below ca. 0.5–0.8 GPa and  $570\text{--}610^\circ\text{C}$  is recorded in both lithologies, and is taken to indicate cooling and exhumation to upper crustal levels. Metamorphism was roughly coeval in the retrogressed ecogites and in the migmatitic metasediment. Metamorphic zircon rims yield U-Pb dates scattering between 340–310 Ma in both lithologies. In the migmatitic metasediment, a distinct younger age at  $306\pm 3$  Ma is interpreted to represent late stages of melt crystallization. In the retrogressed ecogites, zircon zoning and chemical composition (Th/U and REE) indicate initial crystallization of the rims during the HP stage followed by protracted growth during decompression to granulitic / amphibolitic conditions. Rutile U-Pb dating in one eclogite sample yields an age of  $340\pm 11$  Ma similar to the oldest zircon ages and is interpreted to approximate the age of the peak pressure metamorphism. Retrogression in the amphibolite facies is correlated with the development of a penetrative,  $N30^\circ$  subvertical mylonitic S2 foliation. Regionally, this deformation occurs in a dextral transpressive corridor interpreted to represent a crustal-scale shear zone active during the mid-late Carboniferous. We therefore suggest that this structure has driven the exhumation of ecogites from the lower crust and their mixing with mid-crustal felsic lithologies devoid of HP assemblages.

**key words:** Variscan orogeny, External Crystalline Massifs, High pressure metamorphism, U-Pb geochronology, Phase equilibria modeling

## 1. INTRODUCTION

High pressure (HP) metamorphic rocks, namely eclogites and HP granulites, are widespread in the Variscan Belt of Europe (Catalán et al., 2009; Faure et al., 2009; J.-L. Paquette et al., 2017; Schulmann et al., 2009). They are exposed in the Saxo-Thuringian zone and in the high grade metamorphic domains of the allochthonous Galicia-Moldanubian zone, which forms the core of the belt and exposes deep portions of the orogenic crust. These rocks only form minor portions of the exposed high grade units, but they are nevertheless important geodynamical markers, which provide crucial information to reconstruct the dynamics of the Variscan Belt. They are commonly associated with small ultramafic bodies, and may represent dismembered meta-ophiolites, which could possibly mark suture zones formed by the closure of an oceanic basin or a domain of hyperextended continental crust, as it has been inferred for the “Leptyno-amphibolic complexes” in the French Massif Central and in the Armorican Massif (Ballèvre et al., 2009; Faure et al., 2009; Lardeaux et al., 2014). Alternatively, some eclogite-bearing units may also represent deep portions of the orogenic lower crust extruded during the collision, as it has been inferred for the UHT-HP granulites in the Bohemian Massif (Schulmann et al., 2008) or in the eclogites from the Montagne Noire Axial Zone (Roger et al., 2020; Donna L. Whitney et al., 2020).

Independently of their origin, thermobarometric and geochronological information recorded in these HP rocks is crucial to constrain relevant parameters such as exhumation rates, age of peak pressure, and maximal pressure and temperature reached during the collision. The ability to test different geodynamical scenarios with thermomechanical models strongly depends on the quality of the pressure-temperature (P-T) and geochronological data (time) obtained from these HP rocks. However, constraining the P-T-time evolution in complex metamorphic rocks such as eclogites is far from being trivial. Analytical developments made over the past few decades have significantly improved the ability to extract geologically meaningful information from the metamorphic rocks. In particular, the development of high spatial resolution techniques (particularly Secondary Ion Mass Spectrometry (SIMS), Laser Ablation ICP-MS, and to a lesser extent Electron Microprobe) has allowed microscale dating and trace elements analyses on mineral domains to be performed, which can then be used to obtain multiple ages from one single sample and to correlate them with particular

magmatic or metamorphic stages. Prior petrological and geochronological studies of eclogites, which did not benefit from these analytical improvements, are less likely to provide geologically accurate age information. In particular, many ages on high-grade metamorphic samples obtained by ID-TIMS bulk zircon dating are likely a mix between metamorphic and inherited components. This has been for example shown in the recent study of Paquette et al. (2017) for the eclogites and blueschists from the Armorican massif. In the Massif Central, Silurian-Devonian ages (ca. 400–420 Ma) inferred for the HP stage in eclogites has recently been re-estimated at ca. 360–385 Ma by Lu-Hf dating and in situ U-Pb dating of zircon (Benmammar et al., 2020; Lotout et al., 2018; 2020). Many eclogites in the Variscan Belt still lack recent petrological investigation in order to solidly anchor geodynamic models that are based on possibly outdated constraints (e.g. Regorda et al., 2019).

In the Alpine domain, numerous bodies of Variscan eclogites and HP granulites are exposed in the Paleozoic basement, especially in the External Crystalline Massifs (ECM), which form the exposed parts of the basement in the external Western Alps (Von Raumer et al., 2013). Most of the geochronological data available for the HP rocks of the ECM were obtained by multigrain ID-TIMS dating of zircon (e.g. Paquette et al., 1989; Schaltegger, 1993; Schaltegger et al., 2003), which constrained the age of emplacement of the magmatic protoliths to the early-mid Ordovician (ca. 480–450 Ma) and the age of HP metamorphism to the early Devonian (ca. 395–425 Ma). These age constraints have been used in several tectonic studies (Fréville et al., 2018; Guillot & Ménot, 2009; Von Raumer et al., 2009) to argue for the existence of a Devonian oceanic suture across the ECMs, possibly marking the southern prolongation of the Saxo-Thuringian suture (Guillot & Ménot, 2009). However, in the southernmost ECM of Argentera, more recent studies have re-estimated the age of the HP stage to the early-mid Carboniferous (ca. 340 Ma, Jouffray et al., 2020; Rubatto et al., 2010), questioning the previous geodynamic interpretation. Similar studies are lacking for the northern part of the ECM and remain crucial for informing tectonic models. This study aims to provide new thermobarometric and geochronological data on HP rocks and contiguous metasediments exposed in the northeastern Belledonne massif. A detailed structural investigation of the eclogite-bearing unit has also been undertaken in order to better constrain the tectonic setting associated with exhumation of these rocks.

## **2. GEOLOGICAL SETTING**

## 2.1. The External Crystalline Massifs

The External Crystalline Massifs (ECM) represent exposed portions of the European Paleozoic basement involved in the Alpine Orogeny. They form a discontinuous arcuate alignment of massifs along the central and western external Alps, and consist, from the northeast to the south, in the massifs of Aar-Gothard, Mont-Blanc, Aiguilles Rouges, Belledonne, Grandes-Rousses, Oisans-Pelvoux and Argentera-Mercantour (Figure 1). They are composed of (i) various early to mid-Paleozoic units, which were metamorphosed and intruded by granitoids during the Carboniferous and the early Permian, and (ii) non-metamorphic late Carboniferous to Permian sediments deposited over the older metamorphic sequences in small intra-continental basins. The basement is unconformably covered by a thick sedimentary sequence deposited between the Triassic and the Paleogene along the European margin of the Piemonte-Liguria Ocean (Lemoine et al., 1986). The ECM and their post-Permian cover were deformed and metamorphosed during the Alpine collision. Post-Permian deformation in the basement is generally localized. Stretching and thinning of the crust during the lower Jurassic rifting sliced the ECM basement into tens of kilometers wide tilted blocks, separated by kilometer-scale SW-NE-trending normal faults (Lemoine et al., 1986; Lemoine & Trümpy, 1987). The Alpine collision in the External domain was accompanied by ca. 20 to 27% shortening from South to North (Bellahsen et al., 2014). This shortening was accommodated by buckle folding and thrusting in the sedimentary cover and by the development of an anastomosing network of decameter to hectometer-scale shear zones in the basement, with only little tectonic reactivation of older structures (Bellahsen et al., 2012, 2014; Bellanger et al., 2014; Marquer et al., 2006). These shear zones delimit low-strain domains in which Paleozoic structures remained largely preserved. The Alpine metamorphic overprint is mild: metamorphic conditions recorded in Alpine shear zones range from the lower greenschist facies (0.3-0.4 GPa, 300–350 °C, Simon-Labric et al., 2009) in Oisans-Pelvoux to the upper greenschist facies in the Aar-Gothard Massif (0.6 GPa, 400–450 °C, Challandes et al., 2008).

## 2.2. The Belledonne massif

The Belledonne massif forms a 15-20 km wide strip of crustal basement, which extends over more than 100 km from the southwest to the northeast (Figure 1-b). Petrographic and structural

investigation carried out since the 1950<sup>s</sup> (e.g. Bordet, 1961; Bordet & Bordet, 1963; Gros, 1974; Ménot, 1987; Ménot et al., 1987; Verjat, 1981; Vivier et al., 1987) has led to subdivide this massif into three distinct tectono-stratigraphic domains, namely the western, the southwestern and the northeastern domains, separated by late Paleozoic strike-slip faults (Guillot et al., 2009). The western domain is composed of a series of medium to low grade micaschists with minor intercalations of metasediments (“Série Satinée”, Bordet & Bordet, 1963), interpreted as deriving from a thick sequence of deep-sea turbiditic sediments. U-Pb dating of detrital zircons from this series (Fréville et al., 2018) yielded mostly Ediacaran-Cryogenian ages (ca. 550-700 Ma), with subordinate populations of Mesoarchean (ca. 2.8-3.1 Ga) and Paleoproterozoic (ca. 2.0-2.2 Ga) zircons and a youngest population of late Cambrian-Ordovician age (540–463 Ma), which places the maximal deposition age for this series to middle-lower Ordovician. The prevalence of Neoproterozoic zircons suggests this series is mostly composed of material eroded from the peri-Gondwanan Neoproterozoic “Cadomian” belts, with minor contribution of cratonic Gondwanan material.

The southwestern domain consists of different nappes stacked during the Variscan collisional stages (ca. 350–330 Ma, Fréville et al., 2018; Guillot & Ménot, 2009; Ménot et al., 1987) and capped by a sequence of mid-late Devonian metaconglomerates (Taillefer series, Fréville et al., 2018). The uppermost unit is composed of the Chamrousse ophiolitic complex, a well-preserved witness of Cambrian oceanic lithosphere (ca. 500 Ma, Ménot et al., 1988; Pin & Carme, 1987), and regarded as the relic of a short-lived marginal basin that opened in a back-arc setting (Guillot et al., 1992). It is thrust over the late Devonian-Tournaisian magmatic complex of Rioupéroux-Livet (R.-P. Ménot, 1986, 1987) composed of a mafic-felsic bimodal suite of volcanic and plutonic rocks emplaced at ca. 360-350 Ma and attributed to continental extension in a back-arc setting (Fréville et al., 2018; Guillot et al., 2009). This magmatic complex overlies the migmatitic gneisses of the Allemont series. The lower series (Rioupéroux-Livet-Allemont) have been metamorphosed to amphibolite facies during the Variscan nappe stacking events, with peak T conditions increasing from ca. 0.6 GPa and 600 °C in the upper series to ca. 0.8 GPa and 680 °C in the lower migmatitic series (Fernandez et al., 2002; Fréville et al., 2018; Guillot & Ménot, 2009).

Finally, the northeastern domain mostly consists of high grade metamorphic sequences composed of metasediments, orthogneisses and amphibolites, with sporadic occurrence of

retrogressed eclogites that are the main focus of this study. These sequences are intruded by Carboniferous granitoids and overlain by low grade volcano-sedimentary sequences that post-date the granitoids (Vivier et al., 1987). Two main generations of granitoids are identified (Debon et al., 1998; Debon & Lemmet, 1999): a Mg-K-rich suite emplaced during Visean (ca. 340–330 Ma) and a ferriferous low-Mg suite emplaced during upper Carboniferous-early Permian (ca. 310–295 Ma). The Mg-K series predominates in Belledonne (Figure 1-b), and forms the largest Sept Laux, Saint-Colomban and Lauzière plutons emplaced syn-tectonically in strike-slip shear zones (Guillot & Ménot, 2009). Little is known about the old metamorphic sequences. The metasediments presumably derive from a lower Paleozoic series in which mafic and felsic intrusives were emplaced during the Ordovician. The metamorphic evolution is also poorly constrained. The eclogite relics formed at HP were overprinted by high temperature metamorphism, which culminated with partial melting of the most fertile metasedimentary and metaigneous protoliths. However, no quantitative thermobarometry has been carried so far to constrain more precisely this P-T evolution in NE Belledonne.

### **2.3. Structural evolution in the Belledonne massif**

The Variscan collision in Belledonne occurred at ca. 350–295 Ma and is characterized by a succession of different tectono-metamorphic stages, which have been summarized in Guillot & Ménot (2009) and more recently in Fréville et al. (2018). These authors use different labeling for the successive tectono-metamorphic stages, which partly overlap, and also partly disagree between each other. The choice has been made here to group them into four different stages D0 to D3.

- D0 (Dx in Fréville et al., 2018) is poorly constrained and corresponds to the early thrusting of the Chamrousse ophiolitic unit, which presumably occurred during the Devonian (ca. 360–380 Ma). D1 is an early collisional stage which formed E-W directed nappes, mainly visible in the southwestern domain, and was associated with the development of amphibolite-facies assemblages (garnet ± kyanite ± staurolite) at ca. 600–700 °C and 0.6–0.9 GPa (Fréville et al., 2018; Guillot et al., 2009).

The age of D1 is constrained between ca. 350–330 Ma by U-Pb dating on monazite and K/Ar-Ar dating on mica and amphibole (Fréville, 2016; Fréville et al., 2018; R.-P. Ménot et al., 1987)

Following D1, D2 is a transpressive phase associated with the development of N-N30 oriented strike-slip shear zones, which formed a penetrative steeply dipping foliation S2, mostly visible in the

northeastern domain. It has been correlated in the ECMs as well as in the Maures-Tanneron massif and corresponds to a regional-scale dextral shear zone system known as the East Variscan Shear Zone (EVSZ; Corsini & Rolland, 2009; Guillot et al., 2009; Rossi et al., 2009; Simonetti et al., 2018, 2020). Deformation in the EVSZ started from ca. 320 Ma under amphibolite-facies conditions, and lasted at least for 10–15 Ma (Simonetti et al., 2018, 2020). Finally, a stage of D3 extension occurred at ca. 310–295 Ma, associated with the development of SW-NE oriented ductile-brittle normal faults and shear zones (Fernandez et al., 2002). It resulted in the opening of kilometer to ten-kilometer scale coal-bearing half-graben and pull-apart basins, which preserved sedimentological and paleontological evidence for syntectonic sedimentation during the late Westphalian – Stephanian (Ballèvre et al., 2018, and references therein).

### **3. FIELD DESCRIPTION AND STRUCTURAL ANALYSIS**

#### **3.1 Field description**

The area investigated in this study is located North of the Isère Valley, in the high grade metamorphic formations of the northeast Belledonne massif (Figure 1-b). It mostly consists of a ca. 2-3 km thick series composed of biotite-poor metagreywackes with intercalated orthogneisses and amphibolites, which form decameter to hectometer scale lenses elongated along the main foliation (Figure 2-a) (Gros, 1974). Migmatization occurs mostly in the central part of the domain, and is confined to the most fertile lithologies. This metamorphic formation is cut by a kilometer scale intrusive complex composed of microgranites and rhyolites (Grand Mont intrusive complex). It forms steeply-dipping sheets oriented parallel to the main foliation and crossed by N30° oriented shear bands, which argues for a strong tectonic control of the emplacement. The retrogressed eclogites are only found in a hectometer scale amphibolic body exposed near the Lacs de la Tempête (Figure 2-a,b). They form unfoliated meter-size *boudins* preserved in the main metamorphic foliation. The geochemical and geochronological study (ID-TIMS bulk zircon dating) of the eclogites from the ECM done by Paquette et al. (1989) included samples from the Lacs de la Tempête body (reported as samples B7751 to B7755 in the original paper). According to this study, this amphibolite body derives from N/E-MORB like tholeiites emplaced at  $473 \pm 28$  Ma in a thinned continental crust, and metamorphosed to HP ( $> 1.4$  GPa) at  $395 \pm 2$  Ma. Regarding the mode of exposure of eclogites (isolated lenses within

felsic lithologies devoid of HP assemblages) and the geochemical signature and age of the mafic magmatic protoliths, the investigated metamorphic unit presents striking similarities with other Variscan eclogite-bearing units in the Massif Central and the Armorican Massif, commonly referred as “Leptyno-Amphibolic Complexes” (Ballèvre et al., 2009; Faure et al., 2009; Lardeaux et al., 2014; Ménot et al., 1988; Santallier et al., 1988). New U-Pb data presented in this paper will precise both the age of the protolith and the peak of metamorphism.

### **3.2. Structural analysis**

Careful investigation of structures in the field allows the identification of two generations of metamorphic foliation and two main episodes of deformation. The foliation trajectories were mapped and are reported on Figure 2. Field photos of the main structural features are shown on Figures 3 and 4. Labeling reflects our interpretations about how the different structures and deformation stages correlate with the general tectonic framework presented in section 2.3.

The earliest foliation S<sub>x</sub> is a low-angle (< 30°) North-dipping foliation (Figure 3-a), which is interpreted to be pre-D1. It is only preserved in decameter to hectometer wide low-strain domains, which are mostly exposed in the northeastern part of the investigated zone (Figure 2-a). Due to the poor preservation of the structures, the deformation that generated S<sub>x</sub> could not be precisely characterized. Gros (1974) reported evidence of cross laminated sedimentary structures, which suggests S<sub>x</sub> developed at low-grade metamorphic conditions. S<sub>x</sub> is impacted by decimeter to meter scale P1 folding (Figure 3 b,d), which did not generate any new foliation, but formed tight upright to slightly overturned folds oriented N-N15°, with axes slightly plunging to the North (<20°). The general E-W orientation of folding, and the presence of overturned E-vergent folds are consistent with the D1 nappe stacking phase. However, it cannot be excluded that these folds may be the result of shortening during the transpressive phase D2.

The second foliation S<sub>2</sub> is a pervasive, steeply dipping, N15-30° trending foliation that affects the largest part of the metamorphic sequence (Figure 2) and largely overprints the former S<sub>x</sub>, that we associate with D2 dextral strike-slip shearing. In the northeastern part of the field area, D2 is not pervasive and mostly formed localized brittle faults cutting through the low-strain domains. Toward the west, it becomes increasingly intense and pervasive. In the felsic gneisses, it formed the

blastomylonitic S2 foliation that totally obliterated the former structures, which only persist as small lenses and microfold relics (Figures 3-c and 4-a-b). In the mafic lenses, S2 is associated with the amphibolitization of the eclogite assemblages, which only persist in undeformed meter-scale *boudins* (Figure 4-e). Near subhorizontal stretching lineations L2 on S2 planes (Figure 4-g), shear bands and deformed clasts (Figure 4-a-b-c) clearly indicate a dominant dextral strike-slip kinematics. The presence of syn-folial P2 folds (Figure 4-d) with a steeply plunging axis, that developed parallel to S2, is also consistent with this kinematics. Deformation probably initiated at high temperature in the amphibolite facies, as indicated by: (i) the pervasive ductile deformation that affected a several kilometers wide unit; (ii) the development of hornblende oriented parallel to S2 planes in the amphibolites (Figure 4-f); (iii) the presence of sheared leucosomes in the migmatites (Figure 4-b), which suggest migmatization occurred just prior to or during shearing. D2 strike-slip shearing then localized in decameter to hectometer wide brittle fault zones during the latest stages of deformation. These fault zones are well visible in the western part of the metamorphic unit and near the Grand Mont summit (Figure 2).

## 4. METHODS

### 4.1 Mineral and whole rock analyses

Backscattered electron images were acquired at ISTERre Grenoble with a Tescan Vega 3 scanning electron microscope operated with an accelerating voltage of 16 kV and a beam current of 10 nA.

Mineral compositions were measured using a JEOL JXA-8230 electron microprobe at ISTERre Grenoble. Different protocols were used for garnet and the other silicates. Garnet analyses were performed with a 15 kV accelerating voltage, a 20 nA beam current and a counting times of 60s for the peak and 30s for the background. The other silicates were analyzed with a 15 kV accelerating voltage, a 10 nA beam current and counting times of 30s for the peak and 15s for the background. The spot size was set to 1-3  $\mu\text{m}$  depending on the size of minerals and the presence of volatile elements. X-ray element maps were acquired with a 15 kV accelerating voltage, a 100 nA beam current and a 100 ms counting time per pixel. Natural minerals and synthetic glass were used for standardization, and the ZAF matrix procedure was applied for data reduction. X-ray maps were processed using the

XmapTools software (Lanari et al., 2018, 2014). Details of abbreviations used for the mineral end-members are given in Table S1 in the online supplements. The concentration of Zr and other trace elements (Nb, Fe, Cr) in the rutile were measured *in situ* with an electron microprobe at ISTERre Grenoble. The instrument was operated with an acceleration voltage of 20 kV, a beam current of 600 nA, and a total counting time of 600s, with spot size set to 1–3  $\mu\text{m}$ . Standardization was done using a synthetic  $\text{TiO}_2$  glass. Accuracy check was done on standard rutile R632 (Axelsson et al., 2018), which returned accurate Zr concentrations within  $\pm 3\%$  interval. This uncertainty is consistent with counting error statistics returned by the JEOL microprobe software for the rutile analyses (R632 and unknowns), which varies between 2-8% and converts into an absolute uncertainty below 40 ppm in most of the cases. A conservative estimate of  $\pm 50$  ppm is therefore retained for electron microprobe analyses of rutile. This propagates to a ca.  $\pm 10^\circ\text{C}$  uncertainty for Zr in rutile temperatures, which is lower than the calibration uncertainty of the thermometer equation ( $\pm 30^\circ\text{C}$ , Tomkins et al., 2007). In addition, trace element analyses were performed by LA-ICPMS on separated rutile grains, some of which were subsequently dated (see below). Whole rock compositions were obtained on representative rock powders at the SARM laboratory (CNRS-CRPG) in Nancy, using a Thermo Fisher iCap6500 ICP-OES and an iCapQ ICP-MS.

#### **4.2. U-Pb dating and LA-ICPMS trace element analyses**

Zircon and rutile were separated using conventional rock crushing and heavy liquids. Crystals were mounted in epoxy resin and polished to expose the grain center for analysis. Charge contrast (CC) images of zircon grains were obtained with a ZEISS EV050 scanning electron microscope at the Institute of Geological Sciences, University of Bern, at low vacuum conditions (18 Pa), 12 kV, a beam current of 100 mA and a working distance of 9.5 mm. It has been previously demonstrated that CC images correlate exactly to cathodoluminescence (Watt et al., 2000), as also confirmed by checks in the Bern laboratory. Backscattered electron images of separated rutile grains were obtained at Isterre Grenoble using the same instrument and analytical conditions as described above (section 4-1).

Trace element spot analysis of separated zircon and rutile was performed with a RESOLUTION Laser System coupled to an Agilent 7900 quadrupole ICP-MS at the Institute of Geological Sciences (University of Bern). A He-H<sub>2</sub> gas mixture was used as the aerosol transport gas. Zircon trace

element analyses were performed with laser beam diameters of 24 and 20  $\mu\text{m}$ , rutile with a diameter of 38  $\mu\text{m}$ . The laser was set to 5 Hz repetition rate and an energy density on the sample of 4  $\text{J}/\text{cm}^2$ . Oxide interferences were reduced by maintaining  $\text{ThO}/\text{Th} < 0.2$ . Sample analyses were calibrated using NIST SRM 612 (Jochum et al., 2011). Accuracy was monitored using the reference material GSD-1G (Jochum et al., 2005) and zircon 91500 (Wiedenbeck et al., 2004), and was assessed to be better than 10% for all elements. Data reduction was performed using the software Iolite (Paton et al., 2011).

U-Pb dating of rutile was performed with the same LA-ICP-MS system at the University of Bern with the laser operating at a repetition rate of 5 Hz and an energy density on the sample of 3.5  $\text{J}/\text{cm}^2$ . The count rate ratio for  $\text{Th}/\text{U}$  was 98-97 and the  $\text{ThO}/\text{Th} < 0.2$ . Measurements consisted of 30s background and 30s signal acquisition sweeping through the masses  $^{206}\text{Pb}$ ,  $^{207}\text{Pb}$ ,  $^{208}\text{Pb}$ ,  $^{232}\text{Th}$  and  $^{238}\text{U}$ . Spot size was 50 $\mu\text{m}$  with a pre-cleaning with a 60 $\mu\text{m}$  beam. U-Pb ratios were standardized to rutile R10 (1091.6 $\pm$ 3.5 Ma, Luvizotto et al., 2009), whereas secondary reference material was rutile R632 (496 $\pm$ 2 Ma, Axelsson et al., 2018) which returned an average  $^{206}\text{Pb}/^{238}\text{U}$  of 496 $\pm$ 11 Ma. Data reduction was performed using the software Iolite (Paton et al., 2011) running the DRS VizualAge\_UcomPbine (Chew et al., 2014), although no common Pb correction was applied to the data of either standards or unknown. The single spot  $2\sigma$  standard error external on the primary standard was 7.5% and propagated in full to the unknowns.

U-Th-Pb geochronology of zircon was carried out with the SwissSIMS Cameca IMS 1280-HR at Université de Lausanne, which is equipped with an high-brightness Hyperion H201 RF plasma oxygen ion source. Basic instrument set up parameters were 6-8 nA, 20  $\mu\text{m}$   $\text{O}_2$ - primary beam, mass resolution  $M/\Delta M \sim 5000$ , energy window = 40 eV. Data were acquired in mono-collection, peak-hopping mode. U-Pb-Th data were standardized to TEM2 zircon (417 Ma, Black et al., 2003) and accuracy was checked with zircon standard Plešovice (337.17 $\pm$ 0.37 Ma, Sláma et al., 2008) which were cast in the same epoxy mount as the unknowns. Data were collected over 4 analytical sessions in which the Plešovice standard returned average ages between 335.7 $\pm$ 2.6 and 338.5 $\pm$ 3.6 Ma. Uncertainties on standard  $^{206}\text{Pb}/^{238}\text{U} - \text{UO}_2/\text{U}$  calibration were between 1.0 and 1.8% for each session and were propagated to the data. Common Pb correction was based on the measured  $^{204}\text{Pb}$  signal (when significant relative to background) assuming the present-day model terrestrial Pb composition

of Stacey & Kramers (1975). Radiogenic ratios and single ages were calculated using the CIPS program compiled by Martin Whitehouse. Age calculations use the decay constant recommendations of Steiger & Jäger (1977). The IsoplotR package (Vermeesch, 2018) was employed to plot the diagrams and calculate concordia and weighted average ages. Individual uncertainties are quoted at  $1\sigma$  level and the confidence level for weighted average is 95%.

### 4.3. Thermobarometry

The P-T evolution of the retrogressed eclogites and the migmatitic metasediments has been assessed using a combination of Zr-in-rutile thermometry and forward thermodynamic modeling with PerpleX 6.8.4 (Connolly, 2005, 2009). Zr-in-rutile temperatures were calculated using the calibration of Tomkins et al. (2007). Isochemical P-T phase diagrams were computed using the thermodynamic database of Holland & Powell (2011). The solution models used are from Fuhrman & Lindsley (1988); Green et al. (2007, 2016); Holland & Powell (1998, 2011); Newton et al. (1980); White et al. (2000, 2014). A detailed list of the solution models used to compute each phase diagram and the associated references is given in Table S3 in the online supplements. Input compositions used in PerpleX were determined either by ICP-OES analysis of the bulk rock, or on a local domain using the mineral compositions measured with the electron microprobe and mineral volume proportions estimated by point-counting on the thin section. The method and composition used for each calculation are summarized in Table S3. Because PerpleX inputs are specific to each sample, details about chemical systems, input composition and adjustments of fluid content and  $\text{Fe}^{3+}/\text{Fe}_{\text{tot}}$  ratios are specified for each calculation in the Thermobarometry section.

Phase assemblage stability fields and mineral composition have been used to assess the equilibrium P-T conditions of the different mineral assemblages. Predicted mineral compositions on the whole P-T grid have been extracted using the *werami* script (PerpleX) and compared with EPMA measurements. The match between observed and modeled mineral composition has been quantitatively assessed by introducing a misfit function  $\delta(P,T)$ , which measures the distance between observed and predicted composition over the entire P-T grid. Considering  $p$  composition parameters  $(1, \dots, p)$ , the misfit  $\delta(P,T)$  for a given mineral is defined as:

$$\delta(P,T) = 100 \cdot \sqrt{\sum_{i=1}^n \left[ \frac{x_{\text{measured}}^i - x_{P,T}^i}{x_{\text{measured}}^i} \right]^2}$$

where  $x_{measured}^i$  and  $x_{P,T}^i$  correspond respectively to the measured (EPMA) and predicted (PerpleX) values at given P and T for the composition parameter i. For instance, the composition parameters considered for garnet are the proportions of almandine, pyrope grossular and spessartine (when MnO is included in the calculation) end-members. Detail of all composition variables used for each mineral is given in Table S3 in the online supplements. A panel of  $\delta(P,T)$  maps is given on Figure 10.

## 5. PETROGRAPHY AND MINERAL COMPOSITION OF THE METAMORPHIC SAMPLES

Seven samples of retrogressed eclogite and one sample of migmatitic metasediment were collected for petrological investigation and U-Pb dating, after careful field investigation to select only the least retrogressed domains. The seven retrogressed eclogites (JB-18-03(A-F), JB-18-06, JB-18-49, JB-18-50, JB-19-01 and JB-19-02) come from the large amphibolic body near the Lacs de la Tempête. (Figure 2). The garnet-bearing migmatitic metasediment JB-18-46 was collected in the immediate vicinity of this mafic body. Location and main petrological features are summarized in Table 1. Electron probe mineral analyses data are available in Table S2 in the online supplements.

### 5.1. Retrogressed eclogites

The retrogressed eclogites are composed of garnet, clinopyroxene, amphibole, plagioclase and quartz, with accessory epidote-clinozoisite, actinolite, chlorite, rutile, titanite, ilmenite and rare zircon. The collected samples display various degrees of retrogression, and only sample JB-18-50 preserved a complete eclogitic assemblage, in a small centimeter-size fine-grained domain (Figure 5a-f).

Petrographic descriptions are therefore focused on this sample. Mineral compositions given below are only valid for this sample, except when stated otherwise. The complete set of mineral analyses for all the investigated samples is represented in various diagrams on Figure 7 and is also available in Table S2 in the online supplementary data.

Garnet forms millimeter to centimeter size grains, which have been partly resorbed. Two generations of garnet, Grt-1 and Grt-2, are identified based on composition and texture (Figures 5d,e and 7-b). Grt-1 forms the core of the grains, and has a composition of  $Alm_{52-56}Prp_{15-18}Grs_{25-31}Sps_{01-02}$ . It contains various inclusions of quartz, rutile and omphacite, titanite, ilmenite, hornblende and

rare zircon. Titanite, ilmenite and hornblende inclusions are commonly connected with cracks and may therefore not be primary inclusions, but would have rather developed during the subsequent metamorphic stages. In contrast, quartz, rutile, omphacite and zircon inclusions are generally isolated within garnet and are therefore unambiguously primary inclusions that grew together with garnet. Grt-2 forms Ca-rich inclusion-poor rims around Grt-1. It has a composition of  $\text{Alm}_{49-51}\text{Prp}_{15-16}\text{Grs}_{32-34}\text{Sps}_{01}$  and presents multiple concentric growth zones. The irregular boundary between Grt-1 and Grt-2 (Figure 5-e) suggests that resorption of Grt-1 occurred before the development of Grt-2 rims.

Several generations of clinopyroxene are identified (Figures 5d,f and 7a). Primary clinopyroxene (Cpx-1) is an omphacite ( $\text{Jd}_{22-26}$ ), with a  $\text{Mg}/(\text{Mg}+\text{Fe}^{2+})$  ratio (Mg#) between 0.71-0.75. It was generally destabilized following the reaction  $\text{Omph} + \text{Qtz} \rightarrow \text{Di} + \text{Pl}$ , and formed plagioclase + diopside (+ amphibole) symplectites. It is nevertheless preserved as relics in the fine-grained domain and as inclusions in garnet cores (Grt-1). Clinopyroxene formed by destabilization of the primary omphacite occurs in the symplectites, and has been subdivided into two groups, Cpx-2 and Cpx-3, based on its jadeite content (Cpx-2:  $\text{Jd}_{10-20}$ ,  $\text{Mg}\# = 0.70-0.78$ , Cpx-3:  $\text{Jd}_{03-08}$ ,  $\text{Mg}\# = 0.70-0.78$ ). This subdivision is somewhat artificial, as there is a continuous trend from omphacite to diopside measured in the symplectites (Figure 6-a), but it allows identification of successive stages of re-equilibration during the retrogression.

Amphibole occurs in different textural positions in the retrogressed eclogites (Figure 5-a,b,d,h). It mainly forms large millimeter to centimeter size grains associated with plagioclase, which grow in replacement of the symplectites. Amphibole-plagioclase assemblages also develop in coronas around resorbed garnet grains, and amphibole occurs as inclusions in garnet. There is no significant variation in Si-Al,  $\text{Fe}^{2+}$ -Mg and Na-K composition within the same sample, but variation is more significant between different samples (Figure 7e). Amphibole is a magnesian hastingsite in samples JB-18-50 and JB-18-06, whereas it mostly plots in the magnesian hornblende field in samples JB-18-03(A-F). Ti concentration varies over quite a large range. High Ti concentration ( $\text{Ti} > 0.15$  atom per formula) are generally correlated with the presence of Ti-rich minerals (titanite, rutile) bounding the amphibole grains, whereas Ti-poor grains are mostly in the symplectites. Actinolite is present in the most retrogressed samples and generally occurs in cracks together with greenschist-facies minerals (chlorite, epidote, albite).

Plagioclase occurs mostly in the symplectites and as millimeter to centimeter size grains associated with amphibole (Figure 5-a,b,d,h). It also forms thin rims around garnet. It displays a trend of composition in the range An<sub>10-25</sub> in sample JB-18-50, and over a wider range (from An<sub>25</sub> to pure albite) in the other samples (Figure 7f).

Rutile is the main Ti-bearing phase in the retrogressed eclogites. It forms grains of various sizes ranging from a few tens of micrometers to 200  $\mu\text{m}$  (Figure 5-c,d,g,h,i). It forms inclusions in garnet, and it is also found as inclusion in omphacite and amphibole, and within the symplectites. Rutile was partly replaced by titanite and ilmenite during retrogression. In samples JB-18-03A-F, ilmenite is the dominant retrogressive Ti-bearing phase (Figure 5-h,i), and partially replaces rutile, especially in the matrix. In sample JB-18-50 ilmenite is rare and titanite is the main retrogressive phase, which grows forming coronas around rutile (Figure 5-c). In the latter sample, some rutile grains are partly replaced by ilmenite, and the whole is surrounded by a corona of titanite, which gives the following sequence for the stability of Ti-bearing phases during retrogression:  $\text{Rt} \rightarrow \text{Ilm} \rightarrow \text{Ttn}$ .

Zircon is rare in the eclogites, and not all samples provided enough zircon grains for U-Pb dating. It forms grains of various sizes ranging from  $<10 \mu\text{m}$  to  $>200 \mu\text{m}$ , which are found as inclusions in different minerals (garnet, omphacite, hornblende) and within the symplectites. Detailed description of zircon internal textures is provided in Section 7 (U-Pb geochronology).

In summary, minerals observed in the retrogressed eclogites define three successive parageneses: (i) a relict eclogitic assemblage, (ii) a secondary amphibolite / granulitic assemblage that forms the majority of the rocks, and (iii) a later retrograde assemblage composed of greenschist-facies minerals. The eclogitic assemblage consists of garnet cores (Grt-1), omphacite (Cpx-1), quartz and rutile. Amphibole was possibly stable during this stage, but extensive recrystallization which occurred during retrogression makes the identification of possible relicts of HP amphibole difficult. The amphibolitic / granulitic assemblage consists of garnet rims (Grt-2), amphibole (hornblende / hastingsite), plagioclase and diopside (Cpx-2-3) + plagioclase symplectites. It is associated with resorption of rutile (although it was still probably stable at the onset of decompression) and development of ilmenite and then titanite. Finally, the late retrograde paragenesis was formed at greenschist-facies conditions and consists of actinolite, epidote, chlorite, albite and titanite. In the

least retrogressed sample (JB-18-50), this assemblage is restricted to small cracks in garnet, and to the development of pure albite at the expense of plagioclase in symplectites, while it pervasively replaces all the previous assemblages in the most retrogressed samples.

## 5.2. Migmatitic metasediment

Sample JB-18-46 is a migmatitic metasediment mostly composed of quartz, feldspar and biotite, with millimeter-size garnet and accessory rutile and ilmenite (Figure 6). Centimeter size domains interpreted as leucosomes are mainly composed of quartz and feldspar.

Garnet presents a complex zoning, revealed by composition profiles and backscattered electron images (Figures 6-b and 7-d). Three domains are identified, that are from core to rim: (i) a ca. 300  $\mu\text{m}$ -wide core domain with nearly flat Ca-Fe profiles; (ii) a ca. 200  $\mu\text{m}$ -wide mantle domain with Fe-Mg zoning and flat Ca profile; (iii) a 200  $\mu\text{m}$ -wide rim with a flat Fe profile and Ca-Mg zoning. This zoning is interpreted as the successive growth of two garnet generations: Grt-1 forms the core ( $\text{Alm}_{60-65}\text{Prp}_{19-24}\text{Grs}_{14-15}\text{Sps}_{0-1}$ ) and the mantle of the grains, and Grt-2 ( $\text{Alm}_{57-60}\text{Prp}_{21-24}\text{Grs}_{17-19}\text{Sps}_{1-2}$ ) forms the rim (Figure 7-d).

Biotite does not present major compositional variation. Most of the analyzed grains display Mg# of 0.54–0.56 and Ti concentration of 0.15–0.17 atom per formula (Figure 8-c). Feldspar is an andesine ( $\text{An}_{30-37}$ ). No K-feldspar was identified in this sample.

Rutile is observed both as inclusions in garnet, associated with quartz inclusions (Figure 6-a), and in the matrix, where it grows in replacement of ilmenite (Figure 6-c,d).

## 6. THERMOBAROMETRY

### 6.1. Thermodynamic modeling

#### 6.2.1 Retrogressed eclogite (JB-18-50)

Isochemical phase diagrams for the retrogressed eclogites have been calculated in the chemical system NCFMASHTO.  $\text{K}_2\text{O}$  has not been included because it represents a very minor proportion of the bulk rock (ca. 0.3 wt%  $\text{K}_2\text{O}$  in the bulk rock) and is concentrated in alteration phases.

Clinopyroxene stoichiometry indicates the presence of small amounts of Fe<sup>3+</sup> (up to 5% aegirine end-member, Figure 7-a), which could possibly affect the pressure estimation given by the proportion of the jadeite end-member in omphacite. A small amount of excess O<sub>2</sub> (0.15 mol%) has therefore been added, which has been adjusted so that Fe<sup>3+</sup> in modeled clinopyroxene fits with the amount estimated by stoichiometric balance of electron microprobe analyses. This converts into a Fe<sup>3+</sup>/Fe<sub>tot</sub> ratio of 0.047. The reactive bulk composition has been estimated on a small (5x20 mm) texturally homogeneous eclogitic domain which preserves relicts of omphacite (Figure 5-a). For most of the major elements, the composition estimated for this local domain is not significantly different from the bulk rock composition measured by ICP-OES (Table 2). It only appears to be slightly richer in Al and Ca and poorer in Si and Ti, which suggests it contains slightly more garnet than the bulk rock. The absence of strong chemical variation between the different grains cores (garnet and omphacite) suggests that thermodynamic equilibrium was reached at the scale of the local domain during the eclogitic stage. During the retrogression stages, many disequilibrium textures such as symplectites, coronas around garnet and mineral core-rim zoning appeared by destabilization of the eclogitic assemblage, so the assumption of thermodynamic equilibrium for the bulk domain cannot be assumed. Two different phase diagrams have therefore been computed, respectively for the prograde and the retrograde evolution.

The prograde P-T diagram has been computed using the composition of the local domain as the reactive bulk composition, and assuming fluid-saturated conditions to model progressive dehydration of the protolith during prograde metamorphism. Concerning the retrograde evolution, the modification of the reactive volume due to garnet fractionation has been partly taken into account by removing the garnet cores (Grt-1) from the reactive composition, but other disequilibrium may persist, especially regarding the destabilization of omphacite in plagioclase + diopside symplectites. H<sub>2</sub>O has been constrained to a fixed amount to prevent complete resorption of garnet and clinopyroxene during regression. This amount has been adjusted on a P-M<sub>H<sub>2</sub>O</sub> diagram (Figure S.2 in the supplements online) to fit with the observed modal proportions of amphibole, which is the main OH-bearing phase in the system.

The prograde evolution is characterized by progressive dehydration of the protolith and replacement of hydrous minerals (chlorite, epidote-clinozoisite) by garnet and omphacite. The

observed plagioclase-free eclogitic assemblage with co-existing garnet, omphacite, quartz and rutile is only stable above ca. 1.4 GPa and 600 °C (black contour on Figure 8-a). Small amounts of amphibole and epidote/zoisite are predicted in the lower P-T part of this domain. Considering uncertainties due to the calibration of solution models and to unconstrained assumptions concerning the fluid (assumption of fluid saturation during the prograde evolution is only a working hypothesis and not a constrained observation), the possible range of P-T conditions for the HP assemblage has been extended to the hornblende-epidote-bearing fields. Moreover, the presence of these minerals in the eclogitic assemblage cannot be completely ruled out based on petrographic observations (see section 5). At eclogitic conditions and with  $T > 600$  °C, garnet and omphacite are predicted to form respectively ca. 35-50 vol% and ca. 45-50 vol% of the assemblage, the rest being composed of quartz, rutile, and possibly hornblende and epidote/clinozoisite (Figure 9-a). The volume fraction of omphacite is in agreement with the observations (Table S4), assuming that the symplectites represent destabilized grains of omphacite (35% symplectites + 15% omphacite on the thin section = ca. 50% omphacite at HP). Predicted garnet fraction is higher than the fraction actually measured (35%), but this discrepancy probably results from resorption of garnet during retrogression.

At eclogite-facies conditions, garnet composition varies very smoothly with P and T, and it is therefore not a sensitive thermobarometer. There are two local minima for the misfit, one outside of the eclogitic domain which can be excluded, and the other one at ca. 600 °C and 1.7 GPa (Figure 10). However, the compositional isolines relatively widely spaced in the HP domain and do not allow precise P-T estimation. The composition of omphacite depends on its textural position, and inclusions in garnet tend to be more jadeitic than the grains in the matrix. The most jadeite-rich grain, which corresponds to a small inclusion in garnet has a composition consistent with equilibration in the eclogitic domain at  $T > 550-600$  °C (Figure 10). Taking the average of omphacite analyses, which includes relic grains in the matrix, the misfit becomes higher in the eclogitic facies and is minimal just below the Pl-out line. However, omphacite grains in the matrix show internal Na-Al / Ca-Fe-Mg zoning which may be due to post peak-P diffusion, and the most Al-rich cores are commonly replaced by very thin Pl+Cpx symplectites (Figure 5-e-f). The composition of omphacite at peak pressure is therefore rarely preserved in the matrix grains. The *Jd*-rich inclusions are taken to provide a more reliable estimation of the peak-P composition of omphacite.

The retrograde evolution is characterized by progressive resorption of garnet, clinopyroxene and quartz, and the development of hornblende and plagioclase. Rutile is also destabilized at lower pressure and is replaced by titanite and ilmenite at high temperature. However, the degree of retrogression and the stability field of Ti phases are strongly controlled by the amount of fluid in the system: more fluid results in larger resorption of garnet and clinopyroxene and larger development of hornblende and plagioclase. The stability field of rutile at low pressure and ilmenite at low temperature are also reduced at the expense of titanite for fluid-rich compositions.

The retrograde assemblage composed of garnet 2, clinopyroxene 2, hornblende, plagioclase, titanite, rutile, rare ilmenite and without quartz appears only below 1.3–1.0 GPa and 800 °C (black contour on Figure 8-b). The match between the observed and the modeled mineral proportions must be assessed considering that garnet cores (garnet-1) were excluded from the reactive composition. The recalculated mineral proportions are given on Table S4. The correspondence is not totally perfect, except for hornblende, which has been used to adjust the amount of H<sub>2</sub>O. The amount of garnet predicted is too low (ca. 15% instead of 25%) and the amounts of clinopyroxene and plagioclase are slightly too high in comparison with the measured proportions (respectively 45% and 20-25% predicted instead of 40% and 20% for the observed proportions, Figure 9-b and Table S4). These discrepancies may result from uncertainties in the estimation of the proportion of plagioclase vs clinopyroxene in the symplectites, and the proportion of core vs rim in garnet. Moreover, the retrogressed eclogites present disequilibrium textures (symplectites) and were probably not in a perfect state of thermodynamic equilibrium during retrogression.

The optimal fit for garnet composition (Grt-2) is obtained at ca. 1.3 GPa and 730 °C, but the modeled garnet composition remains compatible with the measured values for a large range of P-T conditions between ca. 650–800 °C and 0.9–1.4 GPa (Figure 10). Clinopyroxene Cpx-2 and Cpx-3 correspond to different stages of retrogression. Composition of Cpx-2 is compatible with a formation at relatively HP (ca. 1.3–1.4 GPa assuming T~730 °C), and has probably developed together with Grt-2 during the early stages of retrogression. Composition of Cpx-3 (late symplectites) is only compatible with much lower pressure and temperature (ca. 0.5–0.8 GPa and 550–650 °C). Ti in hornblende is strongly T-dependent and can therefore be used as a thermometer. X(Ti) in coarse grain hornblende ranges between 0.11–0.14 (Figure 7-d), excluding abnormally Ti-rich grains in contact

with rutile or titanite. This converts into a temperature range between ca. 740–810 °C assuming  $P = 1.3$  GPa, consistent with the temperature estimated for Grt-2. Some hornblende in the symplectites contains much less Ti ( $X(\text{Ti}) \sim 0.06\text{--}0.07$ ), which corresponds to  $T \sim 570\text{--}610$  °C, consistent with the P-T conditions estimated for Cpx-3.

### 6.2.2. Migmatitic metasediment (JB-18-46)

The P-T phase diagram for sample JB-18-46 has been computed in the chemical system MnNCKFMASHT. The addition of  $\text{O}_2$ , even in small amount, results in unrealistic stabilization of ilmenite toward high  $P$  ( $>1.0$  GPa) at the expense of rutile, which is not supported by the petrographic observations (in particular, garnet contains numerous inclusions of rutile but no inclusions of ilmenite). This component has therefore been excluded. The reactive composition corresponds to the bulk rock composition measured in sample JB-18-46. This sample is taken from a portion of the migmatite that is predominantly composed of mesosome and only contains minor portions of leucosome ( $<5\%$ ). Fractionation due to possible melt extraction has therefore been neglected.  $\text{H}_2\text{O}$  has been adjusted on a  $T\text{-}M_{\text{H}_2\text{O}}$  section (Figure S4 in the supplements) to fit with the observed amount of biotite (15–20 vol %), which is the main hydrous phase in the system. In contrast with the eclogites, the metasediment does not present significant disequilibrium textures. Garnet cores represent an insignificant proportion of the whole rock (3% of the rock volume for total garnet, probably  $<1\%$  for the garnet cores), so fractionation due to garnet growth has been neglected.

The presence of a small amount of granitic liquid formed by muscovite-breakdown reactions and the absence of K-feldspar constrains  $T$  between 700 and 800 °C (Figure 8-c). The composition of the garnet cores is consistent with sub-solidus growth ca. 1.0–1.15 GPa and 650–700 °C, while the composition of the garnet rims is more consistent with supra-solidus formation at ca. 1.1–1.4 GPa and 720–780 °C (Figure 10). The Ti concentration in biotite indicates temperatures between 720–740 °C consistent with those estimated for the garnet rims. However, the Mg/Fe ratio in biotite ( $\text{Mg}\# = 0.54\text{--}0.56$ ) is inconsistent with these P-T conditions, which may be due to diffusional resetting during retrogression. The modeled stable assemblage at peak-T conditions is composed of garnet, plagioclase, quartz, biotite, white mica and rutile, in equilibrium with ca. 5% of granitic liquid (Figure 8-c). The small amount liquid predicted is consistent with the presence of cm-size leucosomes

observed on the thin section. White mica has not been observed, but is predicted to be present only in small amounts (<5 vol%) at peak-T conditions, and disappears from the stable assemblage below 0.6–1.0 GPa. It may therefore have been completely resorbed during retrogression. The amount of garnet predicted to be stable at peak-T conditions (~8–12 vol%, Figure 9-c) is greater than the amount actually observed in the sample (~3–4 vol%). This may result from strong resorption of garnet during retrogression. Alternatively, it may also be due to different proportions of garnet in the thin section and in the whole rock. Finally, the presence of ilmenite in the matrix indicates that the rock experienced decompression down to ca. 0.6–0.7 GPa following the HP stage (Figure 8-c).

## 6.2. Zr-in-rutile (ZiR) thermometry

The retrogressed eclogites contain rutile in two different textural settings, either as inclusions in the eclogitic garnet 1 or in the matrix. *In situ* analyses of rutile grains performed with the electron microprobe show a distinction in Zr concentration between these two populations (Figure 11-a). The rutile inclusions contain between 370–500 ppm Zr (Table S5), while matrix rutile contains more Zr (550–670 ppm). In sample JB-18-50, a few analyses of rutile inclusions in one garnet grain yield higher Zr concentrations, closer to those of matrix rutile. The composition of rutile grains recovered as mineral separates and analyzed by LA-ICPMS are significantly different from matrix rutile and present Zr concentrations closer to the rutile included in garnet. The calibration of Tomkins et al. (2007) of the Zr-in-rutile thermometer was used to calculate temperatures, with an assumed pressure of 1.6 GPa constrained by the stability of the eclogitic assemblage. Calculated temperatures are in the range 690–730°C for the rutile inclusions and the separated grains, and in the range 720–740 °C for the matrix rutile (Figure 11-b). Instrumental uncertainty for Zr concentration is below 10 ppm for LA-ICPMS analyses and below 50 ppm for electron microprobe analyses. This propagates to an insignificant temperature uncertainty of  $\pm 1$ –2°C for LA-ICPMS data and  $\pm 10$ °C for electron microprobe data, which is in any case lower than the  $\pm 30$  °C uncertainty derived from the calibration of Tomkins et al. (2007). Considering a realistic uncertainty of  $\pm 30$ °C, the T estimates for rutile inclusions and rutile in the matrix are thus indistinguishable and plot between 690 and 740 °C.

In the metasediment, the two rutile populations (rutile inclusions in garnet and matrix rutile associated with ilmenite) present much larger compositional differences than in the retrogressed

eclogites. Rutile inclusions contain ca. 450–550 ppm Zr, while matrix rutile is much poorer in Zr (ca. 50–70 ppm Zr). This yields temperatures in the range 695–715 °C for the rutile inclusions and in the range 515–545 °C for the matrix rutile, assuming  $P = 1.3$  GPa for the rutile inclusions and  $P = 0.8$  GPa for the matrix rutile. For the Zr-poor rutile in the matrix, The  $\pm 50$  ppm on the Zr measurement translates into a temperature uncertainty larger than  $\pm 30$  °C (up to  $\pm 70$  °C), especially for the lower bound due to the logarithmic relation between Zr and T.

## **7. U-Pb GEOCHRONOLOGY**

### **7.1. Zircon and rutile description**

The zircon grains from the retrogressed eclogites are typically 100–150  $\mu\text{m}$  in size and have a slightly rounded shape (Figure 12-a). Most of the grains present a CC-dark core surrounded by a CC-brighter, 10–30  $\mu\text{m}$  wide rim. Grain cores can present oscillatory zoning, but most crystals are characterized by broad sector or fir-tree zoning. Metasediment JB-18-46 contains zircon crystals that vary in size (<100 to 400  $\mu\text{m}$ ) and shapes from rounded to euhedral (Figure 12-b). CC imaging reveals a variety of zoning patterns, with mainly rounded cores with sector or oscillatory zoning that are surrounded by multiple CC-bright overgrowths. Rutile separated for U-Pb dating forms 100–250  $\mu\text{m}$  wide homogeneous grains devoid of ilmenite exsolutions and containing rare inclusions of omphacite (Figure 12-c). Grains are often bordered by titanite and plagioclase.

### **7.2. Zircon composition**

Thorium and Uranium content were measured during SIMS analysis and values are generally consistent with LA-ICPMS data measured on the same domain, considering the different volume sampled. In the retrogressed eclogites, grain cores generally have high U concentrations of 50–900 ppm and Th/U ratios  $> 0.1$ , while rims generally contain 1–50 ppm U and show various Th/U ratios, from  $< 0.01$  to 0.5 (Figure 13-a, Table S6 in the online supplements). Some grain cores with low U and Th/U ratios yield U-Pb dates similar to the rims, and can be considered as belonging to the same population. In metasediment JB-18-46, zircons are richer in U than in the metabasic rocks. Zircon rims were targeted as a priority in order to date the metamorphic events. They contain 100–2000 ppm U with low Th/U ratios in the range 0.001–0.03. Only a few inherited cores yielded higher Th/U ratios.

Some of the zircons analyzed for trace elements by LA-ICPMS present an unusually high concentration of Ti (Table S6), probably due to the sampling of micro-inclusions of rutile or other Ti-bearing phases, and these analyses were therefore discarded. The remaining data were then sorted by  $^{206}\text{Pb}/^{238}\text{U}$  dates and sampling domain (core or rim). Chondrite normalized (Palme and O'Neill 2004) REE patterns are presented on Figure 13-b. Eu anomaly ( $\text{Eu}/\text{Eu}^* = \text{Eu}_\text{N}/(\text{Sm}_\text{N} \cdot \text{Gd}_\text{N})^{1/2}$ ) and  $(\text{Lu}/\text{Gd})_\text{N}$  are used as proxies to discriminate between different zircon populations (Figure 13-a). A summary of trace element data in zircon is available in Table S6 in the online supplements.

In the four samples of retrogressed eclogites, a clear distinction based on REE concentration exists between the old zircon domains (>400 Ma, mostly zircon cores) and the younger ones (300–350 Ma, mostly zircon rims): the younger zircon domains are generally poorer in REE than the older domains and have a flatter REE patterns (Figure 13-b). Zircon cores across samples are similar in REE composition. They have a negative Eu anomaly ( $\text{Eu}/\text{Eu}^* = 0.5\text{--}0.8$ ) and are enriched in HREE, with Lu-Yb concentrations close to 1000 times chondrite and a steep positive slope of the HREE pattern ( $(\text{Lu}/\text{Gd})_\text{N} = 40\text{--}120$ ). By contrast, zircon rims present more significant variation between samples. Zircon rims from sample JB-19-01 display flat or nearly flat HREE profiles at around 10–100 times chondrite composition, with moderated enrichment in HREE relative to MREE ( $(\text{Lu}/\text{Gd})_\text{N} = 4\text{--}12$  for the majority of analyses).  $\text{Eu}/\text{Eu}^*$  could not be calculated because Sm is below detection, but the smooth slope between Eu and Tb suggests the Eu anomaly is weak or absent. Zircon rims from the other retrogressed eclogites (JB-19-02, JB-18-49, JB-18-50) display steeper HREE profiles ( $(\text{Lu}/\text{Gd})_\text{N} > 20$ , and up to 270 in sample JB-18-50) and have a higher content in HREE (Lu-Yb concentrations >100 times chondrite). When it could be calculated,  $\text{Eu}/\text{Eu}^*$  is close to 1 (>0.8).

In metasediment JB-18-46, inherited zircon cores also have a distinctly different REE composition with respect to the rims (Figure 13-b). They zircon cores are ~1 order of magnitude richer in REE than the rims, present a pronounced Eu anomaly ( $\text{Eu}/\text{Eu}^* = 0.03\text{--}0.55$ ) and are strongly enriched in HREE (Lu-Yb concentration up to 5000 times chondrite). Zircon rims display important variations, with REE profiles ranging from flat HREE with a low Eu anomaly ( $(\text{Lu}/\text{Gd})_\text{N} < 10$ , Lu-Yb ~10 times chondrite concentration and  $\text{Eu}/\text{Eu}^* > 0.5$ ) to enriched HREE with a more pronounced Eu

anomaly  $((\text{Lu}/\text{Gd})_N = 10\text{--}60$ , Lu-Yb concentration = 50–100 times chondrite,  $\text{Eu}/\text{Eu}^* < 0.6$ ). There is no clear relation between the U-Pb age and the shape of REE profiles for the rims.

The Ti content in zircon ranges between 1.8–4.2 ppm for the cores and 1.3–5.0 ppm for the rims, with no significant difference between samples (Table S6). Using the calibration of Ferry & Watson (2007), this yields a temperature range of 600–680 °C for the cores and 560–680 °C for the rims (Figure 11-b). These temperatures are significantly lower than those given by Zr-in-rutile thermometry and those estimated for the crystallization of the main metamorphic assemblages. Possible explanations for these discrepancies are reviewed in the discussion.

### 7.3. Zircon U-Pb dating

#### 7.3.1. Retrogressed eclogites

Most of the U-Pb analyses of zircon cores are more than 95% concordant and yielded  $^{206}\text{Pb}/^{238}\text{U}$  dates in the range 440–465 Ma (Figure 14-a,b and Table S7). A few analyses yielded younger dates around 400–430 Ma, which have been excluded from further calculation since they are significantly discordant (up to 20% discordance) and may have been partially reset during metamorphism.

Fourteen zircon cores analyses from samples JB-19-01 and ten core analyses from sample JB-19-02 allowed to define two  $^{206}\text{Pb}/^{238}\text{U}$  weighted mean ages at respectively  $456 \pm 4$  Ma and  $448 \pm 6$  Ma, which are within uncertainty the same as the concordia ages.

Zircon rims were more challenging to analyze, because the U content is generally low (down to 1-2 ppm, Table S7) and rims are thin and difficult to target without overlapping with the core. The position of the SIMS spot has been checked after analysis and mixed analyses between core and rim have been discarded. Some of the remaining data show significant common Pb content, especially in sample JB-18-50. For this sample, uncorrected ratios are presented in a Terra-Wasserburg diagram, where the age is defined by a regression line anchored to the common Pb composition predicted by the model of Stacey & Kramers (1975) at 0 Ma ( $^{207}\text{Pb}/^{206}\text{Pb} = 0.8356$ ). Given the relatively low percent of initial Pb ( $f_{206} < 10\%$ ), the choice of initial Pb composition has little bearing on the age. Five analyses define an intercept age at  $332 \pm 19$  Ma (Figure 14-c). Zircon rims from samples JB-18-49 and JB-19-01 contain a lower percent of common Pb, so corrected ratios are presented in Wetherill concordia diagrams. The zircon rim analyses from sample JB-18-49 define a weighted mean

$^{206}\text{Pb}/^{238}\text{U}$  age of  $311\pm 7$  Ma (Figure 14-f). Analyses from sample JB-19-01 are over-dispersed between 314 Ma and 335 Ma (MSWD = 3.6) and therefore a meaningful average age cannot be calculated. (Figure 14-d-e). Finally, only two rims from sample JB-19-02 could be analyzed. They are slightly discordant ( $\sim 5\%$  discordance) and yield  $^{206}\text{Pb}/^{238}\text{U}$  dates of  $350\pm 7$  Ma and  $351\pm 7$  Ma (Table S7). However, two concordant data points are not enough to define a statistically robust population, and more analyses would be needed to confirm this date.

### 7.3.2. Migmatitic metasediment

Zircon rims in sample JB-18-46 yield  $^{206}\text{Pb}/^{238}\text{U}$  dates scattered between ca. 305-345 Ma (Figure 14-g-h + Table S8). A few inherited cores have older concordant dates at ca. 466 Ma and one younger rim analysis is discordant. The  $^{206}\text{Pb}/^{238}\text{U}$  dates of the zircon rims that are more than 95% concordant do not define a statistically consistent population but rather form three groups centered at ca. 305, 325 and 335 Ma (Figure 14-h). The six youngest dates are from rims with distinct CC that grew over older rims (Figure 12-b). We therefore consider them as a distinct population with an age at  $306\pm 3$  Ma. On the other hand, the dates between  $317\pm 3$  and  $343\pm 3$  Ma are from domains that are similar in CC zoning and in REE composition (Figure 13-b). In the lack of any criteria to define any sub-group, we consider these analyses as a dispersed population, that does not form a statistically homogeneous group and for which a geologically meaningful average age cannot be calculated.

### 7.4. Rutile U-Pb dating

The retrogressed eclogites derive from Fe-Ti rich tholeiites which are rather poor in U, and consequently the U content in rutile is generally low ( $< 1$  ppm). Only the rutile from sample JB-18-03B contained enough U (up to 3 ppm) to be dated (Table S9). The U-Pb analyses contain significant common Pb, so the U-Pb age has been assessed using a linear regression of the uncorrected U-Pb ratios plotted on a Terra-Wasserburg diagram (Figure 14-i). Two data points were excluded as they plot far from the regression line. The unconstrained regression and the regression anchored to the common Pb composition predicted by the model of Stacey & Kramers (1975) at 0 Ma yield identical ages within the uncertainty at  $340\pm 11$  Ma (MSWD = 1.8).

## 8. DISCUSSION

## 8.1. Conditions of metamorphism and P-T evolution

### 8.1.1. Zircon in rutile temperatures

The Zr-in-rutile (ZiR) thermometer has demonstrated to be resistant to diffusion resetting, and has proven its ability to retain ultra-high temperature conditions above 900 °C in granulitic terranes (e.g. Kooijman et al., 2012; Luvizotto & Zack, 2009). Therefore, the measured Zr concentration is interpreted to reflect accurately the actual amount of Zr incorporated in rutile at formation. In the retrogressed eclogites, rutile is stable only at HP (>1.4 GPa under water-saturated conditions, Figure 8-a). The ZiR thermometer is therefore taken to indicate temperature during the eclogitic stage. The rutile inclusions in garnet contain about 150 ppm less Zr than the matrix rutile. This difference may be due to the early entrapment of the rutile inclusions in garnet during the prograde to peak evolution. Such inclusions would have then been protected from further re-equilibration, whereas matrix rutile continued to equilibrate after peak P during decompression. The higher Zr concentration in matrix rutile may thus result either from equilibration at higher temperature, lower pressure or lower  $a_{\text{SiO}_2}$ , all of these changes resulting in more Zr being incorporated in the rutile. The difference induced by these effects on the calculated ZiR temperature is small (+30 °C at constant P or -0.5 GPa at constant T), and is close to the uncertainty of the calibration ( $\pm 30$  °C, Tomkins et al. 2007). The temperature range between 690–740 °C obtained by grouping all the rutiles together is taken to indicate conditions close to the peak pressure, from the late prograde evolution to the onset of decompression.

In the metasediments, the ZiR T for the rutile inclusions in garnet is estimated between 695 and 715 °C, and is within uncertainty the same as T obtained with Ti-in biotite and garnet thermobarometry for the supra-solidus stage. The ZiR T is interpreted as the peak T during the P-T evolution of the metasediment. In contrast, matrix rutile, which grows by replacement of ilmenite (Figure 5-i), records  $T < 550$  °C. At low T, the stability field of rutile extends down to 0.6 GPa in the metasediment (Figure 11). The partial resorption of ilmenite and its replacement by low-T rutile in the matrix has therefore occurred during the late cooling stage, and is a retrograde feature.

### 8.1.2. Possible P-T paths

The thermobarometric estimates obtained by ZiR thermometry and forward thermodynamic modeling indicate that the retrogressed eclogites and the metasediments underwent different P-T evolutions

(Fig. 15). The retrogressed eclogites experienced HP metamorphism during the lower-mid Carboniferous (see below), with minimal peak pressure conditions  $P > 1.4$  GPa and 690–740 °C. This stage was followed by decompression from 1.4 to 1.0 GPa at 700–800 °C, associated with the resorption of the eclogitic assemblage and the development of the secondary amphibolite / granulite-facies assemblage. In contrast, the investigated metasediment does not show any trace of a HP stage at eclogite facies. It records instead prograde evolution from sub-solidus conditions (0.8–1.1 GPa and 600–700 °C) to supra-solidus conditions (1.1–1.4 GPa and 700–780 °C) in upper amphibolite / HP granulite-facies, roughly coeval with the HP stage in the eclogites (see below). A later stage of retrogression in the amphibolite facies is recorded in both lithologies, associated with the development of Na-poor clinopyroxene and Ti-poor hornblende in the eclogites at ca. 0.5–0.8 GPa and 570–610 °C, and with retrograde replacement of ilmenite by rutile in the matrix of the metasediment below 550 °C and 0.6–0.7 GPa. .

In gneiss units that host eclogite relics, it is quite common for the host rock to record lower pressure than that of the enclosed eclogite lenses (Godard, 2001). Possible explanations for this discrepancy include: (i) the obliteration of the former HP assemblage in the host gneiss during retrogression, (ii) mixing of different crustal components with their own P-T history in a tectonic *mélange* zone, or (iii) tectonic overpressure caused by a difference in strain rates between the weak host gneiss and the stronger mafic bodies (Fig. 15).

(i) The obliteration of the HP assemblage in the host gneiss is quite plausible, especially considering the important strain rate associated with D2 dextral shearing, which affected the weak metasediments more intensely than the stronger mafic lenses (Figure 4). Moreover, the HP stage would not have been characterized by a readily identifiable mineral assemblage in the metasediments (Figure 8), which makes the identification of possible HP relics even more difficult. However, the metasediments record a prograde evolution from P-T conditions in the mid amphibolite facies that is roughly coeval (see below) with the development of HP assemblages in the retrogressed eclogite, which is not explained by this scenario.

(ii) The model of tectonic *mélange* provides a more consistent explanation to the absence of HP relics and the preservation of prograde evolution at lower pressure in the metasediments. The mafic protoliths would represent deep portions of the lower crust metamorphosed at eclogite-facies

conditions, while the felsic protoliths would represent portions of the middle crust metamorphosed at lower pressure. These two different crustal fragments would have come together in the middle crust during the high temperature amphibolite stage, before being exhumed to the upper crust.

(iii) Finally, it is possible that the recorded pressure difference between the retrogressed eclogites and the surrounding metasediments results from local tectonic overpressure in the mafic lenses. In terms of rheology, the Lacs de la Tempête unit is composed of a weak metasedimentary matrix containing strong elliptical bodies of amphibolite, which underwent pervasive strike-slip shearing during the D2 tectonic phase. A simple mechanical model which applies to this situation has been proposed by Moulas et al. (2014), which shows that significant deviation from the lithostatic pressure (up to one GPa) can occur, both in the strong bodies and in the surrounding matrix. The pressure excess in the eclogites relative to the metasediments is lower than 0.5–0.6 GPa and is therefore achievable with this process. However, this model implies that HP metamorphism in the strong mafic *boudins* is coeval with D2 dextral shearing, which is not supported by petrographic observations. Indeed, garnet in the retrogressed eclogites is clearly ante-kinematic, while hornblende is syn-D2 (Figure 4-f). D2 is therefore not associated with the development of the garnet-bearing HP assemblage, and more likely took place at amphibolite-facies conditions.

We therefore consider that mixing of HP lower crustal metabasic rocks with mid-crustal felsic gneisses in a tectonic *mélange* zone is the most likely scenario to explain the absence of an HP assemblage in the investigated metasediment.

## **8.2. Timing of the geological evolution**

### **8.2.1. Ordovician mafic intrusions**

The Ordovician zircon cores in the eclogites present typical features of magmatic zircon. They generally display oscillatory, broad sector or fir-tree zoning on CC images and contain more U than the rims, and present high Th/U typical of magmatic zircon (Corfu et al., 2003; Hoskin & Schaltegger, 2003). The steep REE patterns are consistent with crystallization from a gabbroic melt (Hoskin & Schaltegger, 2003). The magmatic cores present only a weak Eu anomaly typically observed in zircon from metagabbros (e.g. Kaczmarek et al., 2008). The calculated TiZ for the magmatic zircon cores are around 650 °C, which are significantly lower than what is expected for the crystallization of a

tholeiitic melt. This apparent T underestimation may be partly due to crystallization in a  $\text{TiO}_2$  undersaturated melt. However, assuming  $a_{\text{TiO}_2} = 0.5$  if ilmenite is the main stable Ti-bearing phase, results in an increase of only ca. 50 °C in the calculated T with the equation of Ferry & Watson (2007). Low TiZ temperatures been documented in other gabbroic rocks (e.g. Kaczmarek et al., 2008), and are attributed to the fact that in such systems, zircon is a late crystallizing phase, and its Ti content reflects the composition of the residual melt rather than that of the original magma. Decrease in Ti concentration in zircon correlated with melt fractionation has for instance been documented in MORB series from the Atlantic Ocean (Grimes et al., 2009), where Ti concentration in zircon decreases from 80–100 ppm in the least evolved rocks down to 5–10 ppm in the most differentiated ones, which results in TiZ temperatures as low as 700 °C in magmatic zircons.

The Ordovician ages of  $456 \pm 4$  Ma and  $448 \pm 6$  Ma are interpreted as the age of crystallization of the gabbroic magmatic protolith. These ages are consistent with the previous estimates at  $473 \pm 28$  Ma obtained by Paquette et al. (1989) using bulk ID-TIMS analysis for the same mafic body, and remain in the typical range of ages measured for Ordovician magmatism in the External western Alps (ca. 450–480 Ma, Bussy et al., 2011; Rubatto et al., 2001; Schaltegger & Gebauer, 1999). Similar Ordovician tholeiitic magmatism is commonly observed in all parts of the Variscan basement (Pin & Marini, 1993), and is generally attributed to a widespread extensional event which affected the northern part of Gondwana and resulted in the rifting of the Rheic and Saxo-Thuringian Oceans during the Early-Mid-Ordovician (Linnemann et al., 2007).

### **8.2.2. Carboniferous metamorphism**

Geochronological data on zircon rims indicate that crystallization took place over an extended period of time. Mid-Carboniferous ages between 340–300 Ma are recorded both in the metasediments and in the retrogressed eclogites, which shows that metamorphism is roughly coeval in the two lithologies.

In the metasediments, geochronological data in zircon rims can be however deconvoluted in three stages of crystallization with an early crystallization at around 340 Ma, a main growth stage at 320 Ma and a late stage at around 305 Ma. Geochronological data were interpreted based on trace element compositions. Three of the retrogressed eclogites (JB-18-49, JB-18-50, JB-19-01) contain zircon rims that are weakly zoned, have low Th/U below 0.1, low U and Th concentrations and contain 10-100

times less REE than the cores. The zircon rims from metasediment JB-18-46 display similar features (Th/U<1, low REE concentration) but with higher Th and U concentrations. These are typical features of metamorphic zircons in mafic rocks and metasediments (Hoskin & Schaltegger, 2003; Rubatto, 2017). However, zircon rims display a large range of REE patterns. The flat HREE patterns with weak or absent Eu anomaly (JB-19-01, plus one profile in JB-18-49) are characteristic of growth in presence of garnet and in a plagioclase-poor reactive bulk (Rubatto, 2002), which suggests that the zircon rims developed in a HP assemblage. Other REE patterns (JB-18-50, JB-18-49) display an enrichment in HREE and a more pronounced negative Eu anomaly, which is more consistent with a growth during garnet-breakdown reactions in presence of plagioclase. In the metasediment JB-18-46, REE patterns also display similar variations (flat to steep HREE, weak to strong negative Eu anomaly), although complete resorption of plagioclase is not expected in the metasediment even at HP (Figure 8-c), and garnet is stable within a larger P-T range than the eclogite. The coronitic and poorly equilibrated textures of the investigated samples may have prevented trace element re-equilibration at the sample scale, thus producing variable REE patterns in zircon rims that have grown (even at the same time) in different textural positions. Dispersion in REE composition of metamorphic zircon has been described in other coronitic metabasic HP rocks (Lotout, 2017; Phillips et al., 2015). The zircons which display HP signature would have crystallized in textural domains which contain a preserved eclogitic assemblage, while the other zircons would have crystallized in more retrogressed plagioclase-rich domains. Following this interpretation, zircon rims are considered to start growing near peak pressure in the eclogite (U-Pb dates at  $342\pm 3$  Ma) and then continue during decompression under granulitic / amphibolitic conditions. The lower T obtained by TiZ thermometer compared to those obtained with other thermobarometers, may be due to the pressure dependence of the TiZ thermometer (estimated to be around  $\pm 50$  °C/GPa, Ferry & Watson, 2007), but more importantly to reduced  $\text{TiO}_2$  and  $\text{SiO}_2$  activities in the reactive bulk that can underestimate T of up to 50°C. This effect is especially relevant for the eclogites, in which quartz is unstable below 1.2–1.3 GPa and rutile unstable below 1.0–1.4 GPa, depending on  $\text{H}_2\text{O}$  activity. In the metasediment, the three distinct age populations suggest rather for episodic zircon growth than continuous protracted growth. The distinct younger event at  $306\pm 3$  Ma was constrained by analyses of distinct metamorphic rims that grew over older rims (Figure 12). The boundary between the two rims is sharp and shown

embayments, suggesting that the older rims were partly resorbed, likely in a melt dominated environment, before the external rim grew. Therefore the younger age of  $306 \pm 3$  Ma from the external zircon rim is attributed to the final crystallization of melt during cooling.

Rutile U-Pb dating yielded an age at  $340 \pm 11$  Ma, which overlaps within uncertainty with the age of the oldest metamorphic zircon ( $< 329$  Ma), but is surprisingly older than most of zircon analyses. The phase diagrams computed for the eclogites (Figure 8-a) indicate that rutile grows at  $P > 1.4$  GPa and is resorbed with decreasing  $P$ . The peak  $T$  obtained for the HP stage and the following decompression is  $> 700$  °C and lasted over an extended period of time possibly exceeding 20 Ma, based on zircon ages. At these conditions, significant Pb diffusion in rutile is expected (Cherniak, 2000; Kooijman et al., 2010; Zack & Kooijman, 2017). Rutile U-Pb ages should therefore record cooling and thus be younger than in zircon, which instead constrains high temperature metamorphism. Given the small amount of U in the dated rutile, it is possible that the  $\pm 11$  Ma uncertainty has been underestimated, and that the rutile age is within uncertainty of that of most metamorphic zircon. However, the similarity between rutile and zircon ages indicate that Pb diffusion in rutile was significantly inhibited. There is a possibility that rutile has retained the age of crystallization because it is shielded in garnet. Diffusion calculations assume that the matrix around the crystal acts as a homogeneous infinite reservoir for the diffusing species. This assumption becomes unrealistic if the crystal is enclosed in another mineral, in which Pb diffusion is slow. In this case, Pb loss in the inclusion would be limited by the slow diffusion of Pb in the shielding mineral. In the retrogressed eclogites, many grains of rutile are enclosed in garnet (Figure 5-c). Electron microprobe analysis of rutile grains in their textural position has shown that inclusions in garnet and matrix grains have distinct Zr contents (Figure 10-a). Almost all the separated rutile analyzed by LA-ICPMS have a Zr content of rutile inclusion indicating that they were enclosed in garnet. This preferential separation of rutile inclusions was probably favoured by partial replacement of rutile by ilmenite and titanite in the strongly retrogressed matrix (Figure 5). Pb diffusion in garnet has been recognized to be slow to insignificant below 800 °C (Burton et al., 1995; Mezger et al., 1989, 1991). It is therefore possible that shielding by garnet has prevented Pb loss from the rutile inclusions, which would thus date the HP crystallization, even if other case studies have shown that this principle is not systematic (Zhou et al., 2020). Similar effects were found for preservation of REE primary compositions (magmatic and

granulitic) for apatite shielded as inclusions in ilmenite-hemanite and garnet from the Bergen eclogite in Norway (Janots et al., 2018).

### 8.3. P-T-t evolution and tectonic interpretation

The eclogite *boudins* and the host felsic gneisses record distinct P-T evolutions, which are roughly coeval between 340 and 310 Ma. In the eclogites, rutile sealed in HP garnet and the oldest metamorphic zircon rims have yielded ages at  $340 \pm 11$  Ma, interpreted to date the HP stage at eclogite-facies ( $>1.4$  GPa, 690–740 °C) and the onset of decompression under granulitic conditions. At the same time, the migmatitic metasediments underwent prograde metamorphism at lower pressure in the amphibolite facies. The two lithologies were amalgamated together between ca. 335–310 Ma at amphibolite / granulite-facies conditions (ca. 1.0–1.4 GPa, 700–780 °C) in the middle crust, and were subsequently exhumed to upper crustal levels. During this time interval, partial melting occurred in the most fertile metasediments and produced small amounts of leucogranite, some of which may have been extracted from the source to form the small granite plutons emplaced syn-tectonically in the upper crust (Figure 2-a). The younger age at  $306 \pm 3$  Ma recorded in the migmatitic metasediment likely corresponds to the final crystallization of melt during cooling, and is contemporaneous with emplacement of the ferriferous low-Mg granitoids in the ECMs (Debon & Lemmet, 1999). The penetrative metamorphic foliation S2, which formed by dextral strike-slip shearing, is correlated with amphibolitization of the eclogitic assemblage in the mafic *boudins* and partial melting in the metasediment. Exhumation therefore occurred in transpression during the D2 tectonic phase. Because of poor preservation of the older structures, it is difficult to correlate them with the P-T-t evolution. E-W folding during D1 may be a relic of the main collision and nappe stacking phase, which took place during the early Carboniferous (D1 phase between ca. 350–330 Ma). The late Carboniferous D2 phase of transpressive dextral shearing has been recognized in the entire ECM, from Argentera-Mercantour to the Mont-Blanc and Aiguilles Rouges massifs (Corsini & Rolland, 2009; Guillot et al., 2009), and is associated with the orogen-wide East-Variscan shear zone, which was active during the late Carboniferous (ca. 330–310 Ma, Simonetti et al., 2018, 2020). This shear zone was probably rooted in the lithospheric mantle and controlled the emplacement of several granitoid plutons (Bussy et al., 2000; Guillot et al., 2009) in the ECM, including the Mg-K rich granitoid series in the Belledonne massif, which partially derives from a subcontinental mantle source (Debon & Lemmet, 1999). This

shear zone may therefore have driven exhumation and mixing of various lithologies from different crustal levels, including the lower crustal eclogite *boudins* and the mid crustal gneisses exposed in the Lacs de la Tempête unit.

#### **8.4. Geodynamic significance of the Carboniferous HP metamorphism in the ECM**

The Variscan eclogites and HP granulites exposed in the other ECM of Argentera-Mercantour and Aiguilles-Rouges display remarkably similar features as those of the Belledonne eclogites presented here. They all derive from normal to enriched MORB-type tholeiites emplaced during the Ordovician between ca. 480 and 450 Ma (Jouffray et al., 2020; J. L. Paquette et al., 1989; Rubatto et al., 2010; Von Raumer & Bussy, 2004), presumably in a thinned continental crust during the opening of the Rheic and Saxo-Thuringian oceans. Peak pressure is constrained between 1.3–1.8 GPa and 650–750°C (Ferrando et al., 2008; Liégeois & Duchesne, 1981; Vanardois et al., 2020; this work), and is followed by near-isothermal decompression to ca. 1.0–0.8 GPa and later cooling in the amphibolite-facies below 600 °C and 0.6–0.7 GPa. The age of the HP stage is consistently recorded around 340 Ma by U-Pb chronometers (Rubatto et al., 2010; this work). Exhumation is constrained between 340–310 Ma, coeval with migmatization in the felsic hosts (Fréville et al., 2018; Jouffray et al., 2020; Rubatto et al., 2010; Von Raumer & Bussy, 2004)

The Carboniferous age recorded for the HP is consistent with that of other Variscan HP rocks in the basement of the Central and Eastern Alps, where the HP stage is constrained between ca. 350–330 Ma by Lu-Hf and U-Pb geochronology (Ladenhauf et al., 2001; Miller & Thöni, 1995; Sandmann et al., 2014; Thöni, 2006; Tumiati et al., 2003). In the more eastern Bohemian Massif, early-mid Carboniferous ages are also reported for the HP rocks of the Moldanubian domain and MORB-derived eclogites in the Erzgebirge (Bröcker et al., 2009; Schmädicke et al., 1995; Schulmann et al., 2005). The Carboniferous HP rocks are widespread in the Variscan Belt, especially in the high grade metamorphic allochthonous domains of the Galicia-Moldanubian zone, and are typically equilibrated at HP-HT/UHT conditions of ca. 700–1000°C and 1.4–2.2 GPa (Maierová et al., 2016; O'Brien, 2000). The Carboniferous eclogites contrast with the scarce mid-late Devonian (400–360 Ma) eclogites that are exposed in the Saxo-Thuringian zone of the Bohemian Massif (Collett et al., 2018;

Konopásek et al., 2019; Kryza & Fanning, 2007; Scherer et al., 2002), in the southern Armorican Massif (Bosse et al., 2000; Paquette et al., 2017), or in the Cabo Ortegal and upper allochthon in Iberia (Martínez Catalán et al., 2020). The latter are typically LT-MT eclogites associated with blueschists (Figure 1-a) and are interpreted as the relics of subduction complexes along the Saxo-Thuringian suture (e.g. Ballèvre et al., 2009; Franke, 2000).

Due to their equilibration at HP-HT/UHT conditions, the Carboniferous HP rocks of the European Variscan Belt rarely preserve prograde metamorphic evolution and only record exhumation from deep crustal levels (O'Brien, 2000). A possible interpretation is that these HP rocks represent deep portions of orogenic lower crust equilibrated at eclogitic/HP granulitic conditions during the main crustal thickening phases, which were then exhumed during the later stages of the collision and the post-orogenic collapse. In the Bohemian massif, a combination of active buckling and gravity-driven extrusion in diapir-like structures is proposed as a mechanism for exhumation, which may favor the mixing of eclogites and migmatites (Schulmann et al., 2005, 2009, 2014; Štípská et al., 2004). The setting in the Western Alps is somewhat different, as no UHT nor dome-like structures have been recognized. We speculate that the lower crust was probably too cold to produce gravity-driven diapirs, and exhumation was more probably driven by active deformation in a transpressive setting, presumably within the lithospheric scale East-Variscan shear zone. In this regard, eclogites exposed in the Montagne Noire Axial Zone (French Massif Central) may be a good analogue. Indeed, they present particularly young zircon U-Pb ages (ca. 310–315 Ma) and record HP conditions at moderate temperature (ca. 1.5 GPa and 700 °C, Whitney et al., 2015, 2020), which is consistent with equilibration in the orogenic lower crust, and similar to the P-T conditions recorded in the ECM eclogites. The mechanism that drove exhumation of lower and mid crustal lithologies in the Montagne Noire Axial Zone is still debated, and could correspond either to bulk extension or compression, but it has been recognized that non coaxial deformation in a large dextral shear zone played an important role (Rabin et al., 2015).

The evolution of the ECM eclogites prior to exhumation is not constrained, as no prograde assemblage has ever been identified. These eclogites, equilibrated in the lower crust, may initially derive from dismembered portions of a subducting slab. Deciphering the early prograde history will

require additional geochronological constraints, possibly by Sm-Nd and Lu-Hf garnet dating of the eclogites.

## 9. CONCLUSION

The eclogite-bearing amphibolite lenses exposed at the Lacs de la Tempête, in northeast Belledonne, derive from Ordovician mafic protoliths emplaced at ca. 450 Ma. They preserve evidence of Carboniferous HP metamorphism under eclogitic conditions ( $>1.4$  GPa and  $690\text{--}740$  °C), followed by decompression from 1.4 to 1.0 GPa at  $700\text{--}800$  °C. In contrast, the associated migmatitic metasediments are devoid of HP mineral assemblages, but records instead prograde evolution from sub-solidus conditions ( $0.8\text{--}1.1$  GPa and  $600\text{--}700$  °C) to supra-solidus conditions ( $1.1\text{--}1.4$  GPa and  $700\text{--}780$  °C). Metamorphism was roughly coeval in the two lithologies, and occurred between 340–310 Ma. Zircon zoning and chemical composition (Th/U and REE) indicate initial crystallization during the HP stage followed by protracted growth during decompression under granulitic / amphibolitic conditions. Rutile in one eclogite sample yields a U-Pb age of  $340\pm 11$  Ma, interpreted as the age of the HP stage, assuming that diffusion was inhibited by its textural position as garnet inclusion. Retrogression is correlated with the development of a penetrative,  $N30^\circ$  subvertical mylonitic S2 foliation, which is associated with the development of the orogen-wide East-Variscan shear zone during the mid-late Carboniferous. We therefore speculate that this shear zone has driven exhumation of the eclogites from the lower crust and their incorporation into felsic gneisses in the middle crust. Due to the absence of preserved prograde assemblages, it was only possible to constrain the exhumation path of the eclogites. The early pre-340 Ma history of these rocks therefore remains unclear. Additional petrochronological investigation is needed in order to better constrain this early evolution.

## ACKNOWLEDGEMENTS

This work was supported by the BRGM through the Référentiel Géologique de la France program (RGF). J-B Jacob was funded by a doctoral grant from the ENS de Lyon. Dr. Caroline Lotout and Dr. Stephen Collett are thanked for their insightful reviews, which greatly improved the quality of the final manuscript. We also thank Alex Bisch, a Bachelor student who was involved in the project during the summer 2018 and greatly helped with the field work. Finally, this work would not have

been possible without the involvement of many technicians and engineers, who were of great help in the preparation of the samples and the operation of the various analytical instruments. We wish to thank Valérie Magnin and Valentina Batanova at Isterre in Grenoble for operating the electron microprobe, and Anne-Sophie Bouvier at the university of Lausanne for her help with the SwissSIMS instrument.

## REFERENCES

- Axelsson, E., Pape, J., Berndt, J., Corfu, F., Mezger, K., & Raith, M. M. (2018). Rutile R632 - A New Natural Reference Material for U-Pb and Zr Determination. *Geostandards and Geoanalytical Research*, 42(3), 319–338. <https://doi.org/10.1111/ggr.12213>
- Ballèvre, M., Bosse, V., Ducassou, C., & Pitra, P. (2009). Palaeozoic history of the Armorican Massif: Models for the tectonic evolution of the suture zones. *Comptes Rendus Geoscience*, 341(2), 174–201. <https://doi.org/10.1016/j.crte.2008.11.009>
- Ballèvre, M., Manzotti, P., & Piazz, G. V. D. (2018). Pre-Alpine (Variscan) Inheritance: A Key for the Location of the Future Valaisan Basin (Western Alps). *Tectonics*, 37(3), 786–817. <https://doi.org/10.1002/2017TC004633>
- Bellahsen, N., Jolivet, L., Lacombe, O., Bellanger, M., Boutoux, A., Garcia, S., Mouthereau, F., Le Pourhiet, L., & Gumiaux, C. (2012). Mechanisms of margin inversion in the external Western Alps: Implications for crustal rheology. *Tectonophysics*, 560–561, 62–83. <https://doi.org/10.1016/j.tecto.2012.06.022>
- Bellahsen, N., Mouthereau, F., Boutoux, A., Bellanger, M., Lacombe, O., Jolivet, L., & Rolland, Y. (2014). Collision kinematics in the western external Alps. *Tectonics*, 33(6), 1055–1088. <https://doi.org/10.1002/2013TC003453>
- Bellanger, M., Bellahsen, N., Jolivet, L., Baudin, T., Augier, R., & Boutoux, A. (2014). Basement shear zones development and shortening kinematics in the Ecrins Massif, Western Alps. *Tectonics*, 33(2), 84–111. <https://doi.org/10.1002/2013TC003294>
- Benmammour, A., Berger, J., Triantafyllou, A., Duchene, S., Bendaoud, A., Baele, J.-M., Bruguier, O., & Diot, H. (2020). Pressure-temperature conditions and significance of Upper Devonian eclogite and amphibolite facies metamorphisms in southern French Massif central Evolution

pression-température et implications des métamorphismes amphibolitique et écolitique du Dévonien supérieur dans le sud du Massif central français. *Bulletin de La Société Géologique de France*, 191(1). <https://doi.org/10.1051/bsgf/2020033>

Black, L. P., Kamo, S. L., Allen, C. M., Aleinikoff, J. N., Davis, D. W., Korsch, R. J., & Foudoulis, C. (2003). TEMORA 1: a new zircon standard for Phanerozoic U–Pb geochronology.

*Chemical Geology*, 200(1), 155–170. [https://doi.org/10.1016/S0009-2541\(03\)00165-7](https://doi.org/10.1016/S0009-2541(03)00165-7)

Bordet, C. (1961). *Recherches géologiques sur la partie septentrionale du Massif de Belledonne (Alpes françaises)*. <https://hal-insu.archives-ouvertes.fr/insu-00720441>

Bordet, P., & Bordet, C. (1963). Belledonne-Grandes Rousses et Aiguilles Rouges-Mont Blanc: quelques données nouvelles sur leurs rapports structuraux. *Mém. H.s. Soc. Géol. Fr.*, 2, 309–316. Scopus.

Bosse, V., Feraud, G., Ruffet, G., Ballèvre, M., Peucat, J.-J., & De Jong, K. (2000). Late Devonian subduction and early-orogenic exhumation of eclogite-facies rocks from the Champtoceaux Complex (Variscan belt, France). *Geological Journal*, 35(3–4), 297–325.

Bröcker, M., Klemd, R., Cosca, M., Brock, W., Larionov, A. N., & Rodionov, N. (2009). The timing of eclogite facies metamorphism and migmatization in the Orlica–Śnieżnik complex, Bohemian Massif: constraints from a multimethod geochronological study. *Journal of Metamorphic Geology*, 27(5), 385–403. <https://doi.org/10.1111/j.1525-1314.2009.00823.x>

Burton, K. W., Kohn, M. J., Cohen, A. S., & O’Nions, R. K. (1995). The relative diffusion of Pb, Nd, Sr and O in garnet. *Earth and Planetary Science Letters*, 133(1–2), 199–211.

Bussy, F., Hernandez, J., & Von Raumer, J. (2000). Bimodal magmatism as a consequence of the post-collisional readjustment of the thickened Variscan continental lithosphere (Aiguilles Rouges-Mont Blanc Massifs, Western Alps). *Earth and Environmental Science Transactions of the Royal Society of Edinburgh*, 91(1–2), 221–233.

Bussy, F., Péronnet, V., Ulianov, A., Epard, J. L., & Raumer, J. (2011). Ordovician magmatism in the external French Alps: witness of a peri-gondwanan active continental margin. *International Symposium on the Ordovician System (11; 2011; Alcalá de Henares, Madrid)*.

Catalán, J. R. M., Arenas, R., Abati, J., Martínez, S. S., García, F. D., Suárez, J. F., Cuadra, P. G., Castiñeiras, P., Barreiro, J. G., & Montes, A. D. (2009). A rootless suture and the loss of the

roots of a mountain chain: the Variscan belt of NW Iberia. *Comptes Rendus Geoscience*, 341(2–3), 114–126.

Challandes, N., Marquer, D., & Villa, I. M. (2008). P-T-t modelling, fluid circulation, and <sup>39</sup>Ar-<sup>40</sup>Ar and Rb-Sr mica ages in the Aar Massif shear zones (Swiss Alps). *Swiss Journal of Geosciences*, 101(2), 269–288. <https://doi.org/10.1007/s00015-008-1260-6>

Cherniak, D. J. (2000). Pb diffusion in rutile. *Contributions to Mineralogy and Petrology*, 139(2), 198–207. <https://doi.org/10.1007/PL00007671>

Chew, D. M., Petrus, J. A., & Kamber, B. S. (2014). U–Pb LA–ICPMS dating using accessory mineral standards with variable common Pb. *Chemical Geology*, 363, 185–199. <https://doi.org/10.1016/j.chemgeo.2013.11.006>

Collett, S., Štípská, P., Schulmann, K., Peřestý, V., Soldner, J., Anczkiewicz, R., Lexa, O., & Kylander-Clark, A. (2018). Combined Lu-Hf and Sm-Nd geochronology of the Mariánské Lázně Complex: New constraints on the timing of eclogite- and granulite-facies metamorphism. *Lithos*, 304–307, 74–94. <https://doi.org/10.1016/j.lithos.2018.02.007>

Connolly, J. A. D. (2005). Computation of phase equilibria by linear programming: A tool for geodynamic modeling and its application to subduction zone decarbonation. *Earth and Planetary Science Letters*, 236(1–2), 524–541. <https://doi.org/10.1016/j.epsl.2005.04.033>

Connolly, J. A. D. (2009). The geodynamic equation of state: What and how. *Geochemistry, Geophysics, Geosystems*, 10(10), n/a-n/a. <https://doi.org/10.1029/2009GC002540>

Corfu, F., Hanchar, J. M., Hoskin, P. W., & Kinny, P. (2003). Atlas of zircon textures. *Reviews in Mineralogy and Geochemistry*, 53(1), 469–500.

Corsini, M., & Rolland, Y. (2009). Late evolution of the southern European Variscan belt: Exhumation of the lower crust in a context of oblique convergence. *Comptes Rendus Geoscience*, 341(2), 214–223. <https://doi.org/10.1016/j.crte.2008.12.002>

Debon, F., Guerrot, C., & Ménot, R.-P. (1998). Late Variscan granites of the Belledonne massif (French Western Alps) : an Early Visean magnesian plutonism. *Bis 1977 Leemann / Ab 1978 Stäubli*. <https://doi.org/10.5169/seals-59275>

Debon, F., & Lemmet, M. (1999). Evolution of Mg/Fe Ratios in Late Variscan Plutonic Rocks from the External Crystalline Massifs of the Alps (France, Italy, Switzerland). *Journal of Petrology*,

40(7), 1151–1185. <https://doi.org/10.1093/etroj/40.7.1151>

- Faure, M., Lardeaux, J.-M., & Ledru, P. (2009). A review of the pre-Permian geology of the Variscan French Massif Central. *Comptes Rendus Geoscience*, 341(2–3), 202–213.
- Fernandez, A., Guillot, S., Ménot, R.-P., & Ledru, P. (2002). Late Paleozoic polyphased tectonics in the SW Belledonne massif (external crystalline massifs, French Alps). *Geodinamica Acta*, 15(2), 127–139.
- Ferrando, S., Lombardo, B., & Compagnoni, R. (2008). Metamorphic history of HP mafic granulites from the Gesso-Stura terrain (Argentera Massif, western Alps, Italy). *European Journal of Mineralogy*, 20(5), 777–790.
- Ferry, J. M., & Watson, E. B. (2007). New thermodynamic models and revised calibrations for the Ti-in-zircon and Zr-in-rutile thermometers. *Contributions to Mineralogy and Petrology*, 154(4), 429–437. <https://doi.org/10.1007/s00410-007-0201-0>
- Franke, W. (2000). The mid-European segment of the Variscides: tectonostratigraphic units, terrane boundaries and plate tectonic evolution. *Geological Society, London, Special Publications*, 179(1), 35–61. <https://doi.org/10.1144/GSL.SP.2000.179.01.05>
- Fréville, K. (2016). *L'orogénèse varisque dans les massifs cristallins externes de Belledonne et du Pelvoux (Alpes occidentales françaises) : rôle de la fusion partielle et du plutonisme dans la structuration de la croûte continentale* [PhD Thesis, Université d'Orléans]. <https://tel.archives-ouvertes.fr/tel-01968058/document>
- Fréville, K., Trap, P., Faure, M., Melleton, J., Li, X.-H., Lin, W., Blein, O., Bruguier, O., & Pujol, M. (2018). Structural, metamorphic and geochronological insights on the Variscan evolution of the Alpine basement in the Belledonne Massif (France). *Tectonophysics*, 726, 14–42.
- Fuhrman, M. L., & Lindsley, D. H. (1988). Ternary-feldspar modeling and thermometry. *American Mineralogist*, 73(3–4), 201–215.
- Godard, G. (2001). Eclogites and their geodynamic interpretation: a history. *Journal of Geodynamics*, 32(1), 165–203. [https://doi.org/10.1016/S0264-3707\(01\)00020-5](https://doi.org/10.1016/S0264-3707(01)00020-5)
- Green, E. C. R., White, R. W., Diener, J. F. A., Powell, R., Holland, T. J. B., & Palin, R. M. (2016). Activity–composition relations for the calculation of partial melting equilibria in metabasic rocks. *Journal of Metamorphic Geology*, 34(9), 845–869. <https://doi.org/10.1111/jmg.12211>

- Green, E., Holland, T., & Powell, R. (2007). An order-disorder model for omphacitic pyroxenes in the system jadeite-diopside-hedenbergite-acmite, with applications to eclogitic rocks. *American Mineralogist*, 92(7), 1181–1189.
- Grimes, C. B., John, B. E., Cheadle, M. J., Mazdab, F. K., Wooden, J. L., Swapp, S., & Schwartz, J. J. (2009). On the occurrence, trace element geochemistry, and crystallization history of zircon from in situ ocean lithosphere. *Contributions to Mineralogy and Petrology*, 158(6), 757.
- Gros, Y. (1974). *Etude pétrologique et structurale du Beaufortin (Nord de Belledonne). Alpes françaises*. [Theses, Université Scientifique et Médicale de Grenoble]. <https://tel.archives-ouvertes.fr/tel-00556510>
- Guillot, S., di Paola, S., Ménot, R.-P., Ledru, P., Spalla, M. I., Gosso, G., & Schwartz, S. (2009). Suture zones and importance of strike-slip faulting for Variscan geodynamic reconstructions of the External Crystalline Massifs of the western Alps. *Bulletin de La Société Géologique de France*, 180(6), 483–500.
- Guillot, S., & Ménot, R.-P. (2009). Paleozoic evolution of the External Crystalline Massifs of the Western Alps. *Comptes Rendus Geoscience*, 341(2–3), 253–265. <https://doi.org/10.1016/j.crte.2008.11.010>
- Guillot, S., Ménot, R.-P., & Lardeaux, J.-M. (1992). Tectonique intra-océanique distensive dans l'ophiolite paléozoïque de Chamrousse (Alpes occidentales). *Bull. Soc. Geol. France*, 163, 229–240.
- Holland, T. J. B., & Powell, R. (2011). An improved and extended internally consistent thermodynamic dataset for phases of petrological interest, involving a new equation of state for solids. *Journal of Metamorphic Geology*, 29(3), 333–383. <https://doi.org/10.1111/j.1525-1314.2010.00923.x>
- Holland, T. J. B., & Powell, R. T. J. . (1998). An internally consistent thermodynamic data set for phases of petrological interest. *Journal of Metamorphic Geology*, 16(3), 309–343.
- Hoskin, P. W. O., & Schaltegger, U. (2003). The Composition of Zircon and Igneous and Metamorphic Petrogenesis. *Reviews in Mineralogy and Geochemistry*, 53(1), 27–62. <https://doi.org/10.2113/0530027>
- Janots, E., Austrheim, H., Spandler, C., Hammerli, J., Trepmann, C. A., Berndt, J., Magnin, V., &

- Kemp, A. I. S. (2018). Rare earth elements and Sm-Nd isotope redistribution in apatite and accessory minerals in retrogressed lower crust material (Bergen Arcs, Norway). *Chemical Geology*, 484, 120–135. <https://doi.org/10.1016/j.chemgeo.2017.10.007>
- Jochum, K. P., Nohl, U., Herwig, K., Lammel, E., Stoll, B., & Hofmann, A. W. (2005). GeoReM: A New Geochemical Database for Reference Materials and Isotopic Standards. *Geostandards and Geoanalytical Research*, 29(3), 333–338. <https://doi.org/10.1111/j.1751-908X.2005.tb00904.x>
- Jouffray, F., Spalla, M. I., Lardeaux, J. M., Filippi, M., Rebay, G., Corsini, M., Zanoni, D., Zucali, M., & Gosso, G. (2020). Variscan eclogites from the Argentera–Mercantour Massif (External Crystalline Massifs, SW Alps): a dismembered cryptic suture zone. *International Journal of Earth Sciences*. <https://doi.org/10.1007/s00531-020-01848-2>
- Kaczmarek, M.-A., Müntener, O., & Rubatto, D. (2008). Trace element chemistry and U–Pb dating of zircons from oceanic gabbros and their relationship with whole rock composition (Lanzo, Italian Alps). *Contributions to Mineralogy and Petrology*, 155(3), 295–312. <https://doi.org/10.1007/s00410-007-0243-3>
- Konopásek, J., Anczkiewicz, R., Jeřábek, P., Corfu, F., & Žáčková, E. (2019). Chronology of the Saxothuringian subduction in the West Sudetes (Bohemian Massif, Czech Republic and Poland). *Journal of the Geological Society*, 176(3), 492–504. <https://doi.org/10.1144/jgs2018-173>
- Kooijman, E., Smit, M. A., Mezger, K., & Berndt, J. (2012). Trace element systematics in granulite facies rutile: implications for Zr geothermometry and provenance studies. *Journal of Metamorphic Geology*, 30(4), 397–412. <https://doi.org/10.1111/j.1525-1314.2012.00972.x>
- Kooijman, Ellen, Mezger, K., & Berndt, J. (2010). Constraints on the U–Pb systematics of metamorphic rutile from in situ LA-ICP-MS analysis. *Earth and Planetary Science Letters*, 293(3), 321–330. <https://doi.org/10.1016/j.epsl.2010.02.047>
- Kryza, R., & Fanning, C. M. (2007). Devonian deep-crustal metamorphism and exhumation in the Variscan Orogen: evidence from SHRIMP zircon ages from the HT-HP granulites and migmatites of the Góry Sowie (Polish Sudetes). *Geodinamica Acta*, 20(3), 159–175. <https://doi.org/10.3166/ga.20.159-175>

Ladenhauf, C., Armstrong, R., Konzett, J., & Miller, C. (2001). The timing of pre-Alpine high pressure metamorphism in the Eastern Alps: constraints from U–Pb SHRIMP dating of eclogite zircons from the Austroalpine Silvretta nappe. *Journal of Conference Abstracts*, 6, 600.

Lardeaux, J. M., Schulmann, K., Faure, M., Janoušek, V., Lexa, O., Skrzypek, E., Edel, J. B., & Štípská, P. (2014). The moldanubian zone in the French Massif Central, Vosges/Schwarzwald and Bohemian Massif revisited: differences and similarities. *Geological Society, London, Special Publications*, 405(1), 7–44.

Lemoine, M., Bas, T., Arnaud-Vanneau, A., Arnaud, H., Dumont, T., Gidon, M., Bourbon, M., de Graciansky, P.-C., Rudkiewicz, J.-L., Megard-Galli, J., & Tricart, P. (1986). The continental margin of the Mesozoic Tethys in the Western Alps. *Marine and Petroleum Geology*, 3(3), 179–199. [https://doi.org/10.1016/0264-8172\(86\)90044-9](https://doi.org/10.1016/0264-8172(86)90044-9)

Lemoine, M., & Trümpy, R. (1987). Pre-oceanic rifting in the alps. *Tectonophysics*, 133(3), 305–320. [https://doi.org/10.1016/0040-1951\(87\)90272-1](https://doi.org/10.1016/0040-1951(87)90272-1)

Liégeois, J.-P., & Duchesne, J.-C. (1981). The Lac Cornu retrograded eclogites (Aiguilles Rouges massif, Western Alps, France): evidence of crustal origin and metasomatic alteration. *Lithos*, 14(1), 35–48. [https://doi.org/10.1016/0024-4937\(81\)90035-9](https://doi.org/10.1016/0024-4937(81)90035-9)

Linnemann, U., Gerdes, A., Drost, K., & Buschmann, B. (2007). The continuum between Cadomian orogenesis and opening of the Rheic Ocean: Constraints from LA-ICP-MS U-Pb zircon dating and analysis of plate-tectonic setting (Saxo-Thuringian zone, northeastern Bohemian Massif, Germany). *Special Papers - Geological Society of America*, 423, 61.

Lotout, C., Poujol, M., Pitra, P., Anczkiewicz, R., & Van Den Driessche, J. (2020). From Burial to Exhumation: Emplacement and Metamorphism of Mafic Eclogitic Terranes Constrained Through Multimethod Petrochronology, Case Study from the Lévézou Massif (French Massif Central, Variscan Belt). *Journal of Petrology*, 61(4). <https://doi.org/10.1093/petrology/egaa046>

Lotout, Caroline. (2017). *Âge, durée et enregistrement du métamorphisme de haute pression dans le massif Central* [PhD Thesis].

Lotout, Caroline, Pitra, P., Poujol, M., Anczkiewicz, R., & Van Den Driessche, J. (2018). Timing and

duration of Variscan high-pressure metamorphism in the French Massif Central: A multimethod geochronological study from the Najac Massif. *Lithos*, 308–309, 381–394. <https://doi.org/10.1016/j.lithos.2018.03.022>

Luvizotto, G. L., & Zack, T. (2009). Nb and Zr behavior in rutile during high-grade metamorphism and retrogression: An example from the Ivrea–Verbano Zone. *Chemical Geology*, 261(3), 303–317. <https://doi.org/10.1016/j.chemgeo.2008.07.023>

Luvizotto, G. L., Zack, T., Meyer, H. P., Ludwig, T., Triebold, S., Kronz, A., Münker, C., Stockli, D. F., Prowatke, S., Klemme, S., Jacob, D. E., & von Eynatten, H. (2009). Rutile crystals as potential trace element and isotope mineral standards for microanalysis. *Chemical Geology*, 261(3), 346–369. <https://doi.org/10.1016/j.chemgeo.2008.04.012>

Maierová, P., Schulmann, K., Lexa, O., Guillot, S., Štípská, P., Janoušek, V., & Čadek, O. (2016). European Variscan orogenic evolution as an analogue of Tibetan-Himalayan orogen: Insights from petrology and numerical modeling: Variscan and Himalayan Orogenies. *Tectonics*, 35(7), 1760–1780. <https://doi.org/10.1002/2015TC004098>

Marquer, D., Calcagno, P., Barfety, J.-C., & Baudin, T. (2006). 3D Modeling and Kinematics of the External Zone of the French Western Alps (Belledonne and Grand Châtelard Massifs, Maurienne Valley, Savoie). *Eclogae Geologicae Helvetiae*, 99(2), 211–222. <https://doi.org/10.1007/s00015-006-1183-z>

Martínez Catalán, J. R., Collett, S., Schulmann, K., Aleksandrowski, P., & Mazur, S. (2020). Correlation of allochthonous terranes and major tectonostratigraphic domains between NW Iberia and the Bohemian Massif, European Variscan belt. *International Journal of Earth Sciences*, 109(4), 1105–1131. <https://doi.org/10.1007/s00531-019-01800-z>

Ménot, R. ., Peucat, J. ., & Paquette, J. . (1988). Les associations magmatiques acide-basique paléozoïques et les complexes leptyno-amphiboliques: les corrélations hasardeuses. Exemples du massif de Belledonne (Alpes occidentales). *Bull Soc Géol Fr*, 8, 917–926.

Ménot, R.-P. (1986). Les formations plutono-volcaniques dévoniennes de Rioupéroux-Livet (Massifs cristallins externes des Alpes Françaises): nouvelles définitions lithostratigraphique et pétrographique. *Les Formations Plutono-Volcaniques Dévoniennes de Rioupéroux-Livet (Massifs Cristallins Externes Des Alpes Françaises): Nouvelles Définitions*

*Lithostratigraphique et Pétrographique*, 66(1–2), 229–258.

Ménot, R.-P. (1987). Magmatismes et structuration orogénique paléozoïques de la chaîne de Belledonne (Massifs cristallins externes alpins). Le domaine sud - occidental. *Magmatismes et Structuration Orogénique Paléozoïques de La Chaîne de Belledonne (Massifs Cristallins Externes Alpines)*. *Le Domaine Sud - Occidental*, 63, 55–93.

Ménot, R.-P., Bonhomme, M. G., & Vivier, G. (1987). Structuration tectono-métamorphique carbonifère dans le massif de Belledonne (Alpes Occidentales françaises), apport de la géochronologie K/Ar des amphiboles. *Schweizerische Mineralogische Und Petrographische Mitteilungen*, 67(3), 273–284.

Ménot, R.-P., Peucat, J. J., Scarenzi, D., & Piboule, M. (1988). 496 My age of plagiogranites in the Chamrousse ophiolite complex (external crystalline massifs in the French Alps): evidence of a Lower Paleozoic oceanization. *Earth and Planetary Science Letters*, 88(1–2), 82–92.

Mezger, K., Hanson, G. N., & Bohlen, S. R. (1989). U-Pb systematics of garnet: dating the growth of garnet in the late Archean Pikwitonei granulite domain at Cauchon and Natawahunan Lakes, Manitoba, Canada. *Contributions to Mineralogy and Petrology*, 101(2), 136–148.

<https://doi.org/10.1007/BF00375301>

Mezger, K., Rawnsley, C. M., Bohlen, S. R., & Hanson, G. N. (1991). U-Pb Garnet, Sphene, Monazite, and Rutile Ages: Implications for the Duration of High-Grade Metamorphism and Cooling Histories, Adirondack Mts., New York. *The Journal of Geology*, 99(3), 415–428.

<https://doi.org/10.1086/629503>

Miller, C., & Thöni, M. (1995). Origin of eclogites from the Austroalpine Ötztal basement (Tirol, Austria): geochemistry and Sm–Nd vs. Rb–Sr isotope systematics. *Chemical Geology*, 122(1), 199–225. [https://doi.org/10.1016/0009-2541\(95\)00033-I](https://doi.org/10.1016/0009-2541(95)00033-I)

Moulas, E., Burg, J.-P., & Podladchikov, Y. (2014). Stress field associated with elliptical inclusions in a deforming matrix: Mathematical model and implications for tectonic overpressure in the lithosphere. *Tectonophysics*, 631, 37–49. <https://doi.org/10.1016/j.tecto.2014.05.004>

Newton, R. C., Charlu, T. V., & Kleppa, O. J. (1980). Thermochemistry of the high structural state plagioclases. *Geochimica et Cosmochimica Acta*, 44(7), 933–941.

O'Brien, P. J. (2000). The fundamental Variscan problem: high-temperature metamorphism at

different depths and high-pressure metamorphism at different temperatures. *Geological Society, London, Special Publications*, 179(1), 369–386.

<https://doi.org/10.1144/GSL.SP.2000.179.01.22>

Paquette, J. L., Menot, R. P., & Peucat, J. J. (1989). REE, Sm-Nd and U-Pb zircon study of eclogites from the Alpine External Massifs (Western Alps): evidence for crustal contamination. *Earth and Planetary Science Letters*, 96(1–2), 181–198.

Paquette, J.-L., Ballèvre, M., Peucat, J.-J., & Cornen, G. (2017). From opening to subduction of an oceanic domain constrained by LA-ICP-MS U-Pb zircon dating (Variscan belt, Southern Armorican Massif, France). *Lithos*, 294–295, 418–437.

<https://doi.org/10.1016/j.lithos.2017.10.005>

Paton, C., Hellstrom, J., Paul, B., Woodhead, J., & Hergt, J. (2011). Iolite: Freeware for the visualisation and processing of mass spectrometric data. *Journal of Analytical Atomic Spectrometry*, 26(12), 2508–2518. <https://doi.org/10.1039/C1JA10172B>

Phillips, G., Offler, R., Rubatto, D., & Phillips, D. (2015). High-pressure metamorphism in the southern New England Orogen: Implications for long-lived accretionary orogenesis in eastern Australia. *Tectonics*, 34(9), 1979–2010. <https://doi.org/10.1002/2015TC003920>

Pin, C., & Carne, F. (1987). A Sm-Nd isotopic study of 500 Ma old oceanic crust in the Variscan belt of Western Europe: the Chamrousse ophiolite complex, Western Alps (France). *Contributions to Mineralogy and Petrology*, 96(3), 406–413.

Pin, C., & Marini, F. (1993). Early Ordovician continental break-up in Variscan Europe: Nd-Sr isotope and trace element evidence from bimodal igneous associations of the Southern Massif Central, France. *Lithos*, 29(3), 177–196. [https://doi.org/10.1016/0024-4937\(93\)90016-6](https://doi.org/10.1016/0024-4937(93)90016-6)

Rabin, M., Trap, P., Carry, N., Fréville, K., Cenko-Tok, B., Lobjoie, C., Goncalves, P., & Marquer, D. (2015). Strain partitioning along the anatectic front in the Variscan Montagne Noire massif (southern French Massif Central): Anatectic Front and Strain Partitioning. *Tectonics*, 34(8), 1709–1735. <https://doi.org/10.1002/2014TC003790>

Regorda, A., Lardeaux, J.-M., Roda, M., Marotta, A. M., & Spalla, M. I. (2019). How many subductions in the Variscan orogeny? Insights from numerical models. *Geoscience Frontiers*.

<https://doi.org/10.1016/j.gsf.2019.10.005>

- Roger, F., Teyssier, C., Whitney, D. L., Respaut, J.-P., Paquette, J.-L., & Rey, P. F. (2020). Age of metamorphism and deformation in the Montagne Noire dome (French Massif Central): Tapping into the memory of fine-grained gneisses using monazite U-Th-Pb geochronology. *Tectonophysics*, 228316.
- Rossi, P., Oggiano, G., & Cocherie, A. (2009). A restored section of the “southern Variscan realm” across the Corsica–Sardinia microcontinent. *Comptes Rendus Geoscience*, 341(2–3), 224–238.
- Rubatto, D. (2002). Zircon trace element geochemistry: partitioning with garnet and the link between U–Pb ages and metamorphism. *Chemical Geology*, 184(1), 123–138.  
[https://doi.org/10.1016/S0009-2541\(01\)00355-2](https://doi.org/10.1016/S0009-2541(01)00355-2)
- Rubatto, D. (2017). Zircon: the metamorphic mineral. *Reviews in Mineralogy and Geochemistry*, 83(1), 261–295.
- Rubatto, D., Ferrando, S., Compagnoni, R., & Lombardo, B. (2010). Carboniferous high-pressure metamorphism of Ordovician protoliths in the Argentera Massif (Italy), Southern European Variscan belt. *Lithos*, 116(1–2), 65–76.
- Rubatto, D., Schaltegger, U., Lombardo, D., Colombo, F., & Compagnoni, R. (2001). Complex Paleozoic magmatic and metamorphic evolution in the Argentera massif (Western Alps), resolved with U-Pb dating. *Schweizerische Mineralogische Und Petrographische Mitteilungen*, 81, 213–228.
- Sandmann, S., Nagel, T. J., Herwartz, D., Fonseca, R. O. C., Kurzwski, R. M., Münker, C., & Froitzheim, N. (2014). Lu–Hf garnet systematics of a polymetamorphic basement unit: new evidence for coherent exhumation of the Adula Nappe (Central Alps) from eclogite-facies conditions. *Contributions to Mineralogy and Petrology*, 168(5), 1075.  
<https://doi.org/10.1007/s00410-014-1075-6>
- Santallier, D., Briand, B., Menot, R. P., & Piboule, M. (1988). Les complexes leptyno-amphiboliques (CLA): revue critique et suggestions pour un meilleur emploi de ce terme. *Bulletin de La Société Géologique de France*, 4(1), 3–12.
- Schaltegger, U. (1993). The evolution of the polymetamorphic basement in the Central Alps unravelled by precise U- Pb zircon dating. *Contributions to Mineralogy and Petrology*, 113(4), 466–478.

- Schaltegger, U., Abrecht, J., & Corfu, F. (2003). The Ordovician orogeny in the Alpine basement: constraints from geochronology and geochemistry in the Aar Massif (Central Alps). *Swiss Bulletin of Mineralogy and Petrology*, 83(2), 183–239.
- Schaltegger, U., & Gebauer, D. (1999). Pre-Alpine geochronology of the central, western and southern Alps. *Schweizerische Mineralogische Und Petrographische Mitteilungen*, 79, 79–87.
- Scherer, E. E., Mezger, K., & Munker, C. (2002). Lu-Hf ages of high pressure metamorphism in the Variscan fold belt of southern Germany. *Geochimica et Cosmochimica Acta*, 66, A677–A677.
- Schmädicke, E., Mezger, K., Cosca, M. A., & Okrusch, M. (1995). Variscan Sm-Nd and Ar-Ar ages of eclogite facies rocks from the Erzgebirge, Bohemian Massif. *Journal of Metamorphic Geology*, 13(5), 537–552. <https://doi.org/10.1111/j.1525-1314.1995.tb00241.x>
- Schulmann, K., Catalán, J.-R. M., Lardeaux, J.-M., Janoušek, V., & Oggiano, G. (2014). The Variscan orogeny: extent, timescale and the formation of the European crust. *Geological Society, London, Special Publications*, 405(1), 1–6. <https://doi.org/10.1144/SP405.15>
- Schulmann, K., Konopásek, J., Janoušek, V., Lexa, O., Lardeaux, J.-M., Edel, J.-B., Štípská, P., & Ulrich, S. (2009). An Andean type Palaeozoic convergence in the Bohemian Massif. *Comptes Rendus Geoscience*, 341(2), 266–286. <https://doi.org/10.1016/j.crte.2008.12.006>
- Schulmann, K., Kröner, A., Hegner, E., Wendt, I., Konopásek, J., Lexa, O., & Štípská, P. (2005). Chronological constraints on the pre-orogenic history, burial and exhumation of deep-seated rocks along the eastern margin of the Variscan Orogen, Bohemian Massif, Czech Republic. *American Journal of Science*, 305(5), 407–448. <https://doi.org/10.2475/ajs.305.5.407>
- Schulmann, K., Lexa, O., Štípská, P., Racek, M., Tajčmanová, L., Konopásek, J., Edel, J.-B., Peschler, A., & Lehmann, J. (2008). Vertical extrusion and horizontal channel flow of orogenic lower crust: key exhumation mechanisms in large hot orogens? *Journal of Metamorphic Geology*, 26(2), 273–297. <https://doi.org/10.1111/j.1525-1314.2007.00755.x>
- Simonetti, M., Carosi, R., Montomoli, C., Cottle, J. M., & Law, R. D. (2020). Transpressive Deformation in the Southern European Variscan Belt: New Insights From the Aiguilles Rouges Massif (Western Alps). *Tectonics*, 39(6), e2020TC006153. <https://doi.org/10.1029/2020TC006153>
- Simonetti, Matteo, Carosi, R., Montomoli, C., Langone, A., D’Addario, E., & Mammoliti, E. (2018).

Kinematic and geochronological constraints on shear deformation in the Ferriere-Mollières shear zone (Argentera-Mercantour Massif, Western Alps): implications for the evolution of the Southern European Variscan Belt. *International Journal of Earth Sciences*, 107(6), 2163–2189. <https://doi.org/10.1007/s00531-018-1593-y>

Simon-Labric, T., Rolland, Y., Dumont, T., Heymes, T., Authemayou, C., Corsini, M., & Fornari, M. (2009).  $^{40}\text{Ar}/^{39}\text{Ar}$  dating of Penninic Front tectonic displacement (W Alps) during the Lower Oligocene (31–34 Ma). *Terra Nova*, 21(2), 127–136. <https://doi.org/10.1111/j.1365-3121.2009.00865.x>

Sláma, J., Košler, J., Condon, D. J., Crowley, J. L., Gerdes, A., Hanchar, J. M., Horstwood, M. S. A., Morris, G. A., Nasdala, L., Norberg, N., Schaltegger, U., Schoene, B., Tubrett, M. N., & Whitehouse, M. J. (2008). Plešovice zircon — A new natural reference material for U–Pb and Hf isotopic microanalysis. *Chemical Geology*, 249(1), 1–35. <https://doi.org/10.1016/j.chemgeo.2007.11.005>

Stacey, J., & Kramers, J. (1975). Approximation of terrestrial lead isotope evolution by a two-stage model. *Earth and Planetary Science Letters*, 26(2), 207–221.

Steiger, R. H., & Jäger, E. (1977). Subcommittee on geochronology: Convention on the use of decay constants in geo- and cosmochemistry. *Earth and Planetary Science Letters*, 36(3), 359–362. [https://doi.org/10.1016/0012-821X\(77\)90060-7](https://doi.org/10.1016/0012-821X(77)90060-7)

Štípská, P., Schulmann, K., & Kröner, A. (2004). Vertical extrusion and middle crustal spreading of omphacite granulite: a model of syn-convergent exhumation (Bohemian Massif, Czech Republic). *Journal of Metamorphic Geology*, 22(3), 179–198. <https://doi.org/10.1111/j.1525-1314.2004.00508.x>

Thöni, M. (2006). Dating eclogite-facies metamorphism in the Eastern Alps—approaches, results, interpretations: a review. *Mineralogy and Petrology*, 88(1–2), 123–148.

Tomkins, H. S., Powell, R., & Ellis, D. J. (2007). The pressure dependence of the zirconium-in-rutile thermometer. *Journal of Metamorphic Geology*, 25(6), 703–713. <https://doi.org/10.1111/j.1525-1314.2007.00724.x>

Tumiati, S., Thöni, M., Nimis, P., Martin, S., & Mair, V. (2003). Mantle–crust interactions during Variscan subduction in the Eastern Alps (Nonsberg–Ulten zone): geochronology and new

petrological constraints. *Earth and Planetary Science Letters*, 210(3–4), 509–526.

Vanardois, J., Trap, P., Roger, F., Barou, F., Lanari, P., Marquer, D., Paquette, J.-L., Melleton, J., & Fréville, K. (2020). *New deformation, metamorphic and geochronological data on the Aiguilles-Rouges massif (Alpine External Crystallin massifs, France). A reappraisal of the Variscan tectono-metamorphic evolution in the Alpine Western External Crystallin massifs*. 22, 8143. <http://adsabs.harvard.edu/abs/2020EGUGA..22.8143V>

Verjat, J. L. (1981). *Etude pétrologique et structurale des terrains cristallins du sud-est de Belledonne, à l'ouest du col du Glandon - Alpes françaises*. <https://tel.archives-ouvertes.fr/tel-00547453>

Vermeesch, P. (2018). Statistical models for point-counting data. *Earth and Planetary Science Letters*, 501, 112–118.

Vivier, G., Ménot, R.-P., & Giraud, P. (1987). Magmatismes et structuration orogénique Paléozoïques de la chaîne de Belledonne (Massifs cristallins externes alpins). Le domaine nord-oriental. *Géologie Alpine (Grenoble)*, 63, 25–53.

Von Raumer, J. F., & Bussy, F. (2004). Mont Blanc and Aiguilles Rouges geology of their polymetamorphic basement (external massifs, Westerns Alps, France-Switzerland). In *Mémoires de Géologie (Lausanne)* (Vol. 42, pp. 1–210).

Von Raumer, J. F., Bussy, F., Schaltegger, U., Schulz, B., & Stampfli, G. M. (2013). Pre-Mesozoic Alpine basements—their place in the European Paleozoic framework. *Bulletin*, 125(1–2), 89–108.

Von Raumer, J. F., Bussy, F., & Stampfli, G. M. (2009). The Variscan evolution in the External massifs of the Alps and place in their Variscan framework. *Comptes Rendus Geoscience*, 341(2–3), 239–252. <https://doi.org/10.1016/j.crte.2008.11.007>

Watt, G. R., Griffin, B. J., & Kinny, P. D. (2000). Charge contrast imaging of geological materials in the environmental scanning electron microscope. *American Mineralogist*, 85(11–12), 1784–1794. <https://doi.org/10.2138/am-2000-11-1221>

White, R. W., Powell, R., Holland, T. J. B., Johnson, T. E., & Green, E. C. R. (2014). New mineral activity–composition relations for thermodynamic calculations in metapelitic systems. *Journal of Metamorphic Geology*, 32(3), 261–286. <https://doi.org/10.1111/jmg.12071>

- White, R. W., Powell, R., Holland, T. J. B., & Worley, B. A. (2000). The effect of TiO<sub>2</sub> and Fe<sub>2</sub>O<sub>3</sub> on metapelitic assemblages at greenschist and amphibolite facies conditions: mineral equilibria calculations in the system K<sub>2</sub>O-FeO-MgO-Al<sub>2</sub>O<sub>3</sub>-SiO<sub>2</sub>-H<sub>2</sub>O-TiO<sub>2</sub>-Fe<sub>2</sub>O<sub>3</sub>. *Journal of Metamorphic Geology*, 18(5), 497–511.
- Whitney, D L., Roger, F., Teyssier, C., Rey, P. F., & Respaut, J.-P. (2015). Syn-collapse eclogite metamorphism and exhumation of deep crust in a migmatite dome: The P–T–t record of the youngest Variscan eclogite (Montagne Noire, French Massif Central). *Earth and Planetary Science Letters*, 430, 224–234. <https://doi.org/10.1016/j.epsl.2015.08.026>
- Whitney, Donna L., Hamelin, C., Teyssier, C., Raia, N. H., Korchinski, M. S., Seaton, N. C. A., Bagley, B. C., Handt, A. von der, Roger, F., & Rey, P. F. (2020). Deep crustal source of gneiss dome revealed by eclogite in migmatite (Montagne Noire, French Massif Central). *Journal of Metamorphic Geology*, 38(3), 297–327. <https://doi.org/10.1111/jmg.12523>
- Wiedenbeck, M., Hanchar, J. M., Peck, W. H., Sylvester, P., Valley, J., Whitehouse, M., Kronz, A., Morishita, Y., Nasdala, L., Fiebig, J., Franchi, I., Girard, J.-P., Greenwood, R. C., Hinton, R., Kita, N., Mason, P. R. D., Norman, M., Ogasawara, M., Piccoli, P. M., ... Zheng, Y.-F. (2004). Further Characterisation of the 91500 Zircon Crystal. *Geostandards and Geoanalytical Research*, 28(1), 9–39. <https://doi.org/10.1111/j.1751-908X.2004.tb01041.x>
- Zack, T., & Kooijman, E. (2017). Petrology and Geochronology of Rutile. *Reviews in Mineralogy and Geochemistry*, 83(1), 443–467. <https://doi.org/10.2138/rmg.2017.83.14>
- Zhou, T., Li, Q., Klemd, R., Shi, Y., Tang, X., Li, C., & Liu, Y. (2020). Multi-system geochronology of North Dabie eclogite: Ineffective garnet ‘shielding’ on rutile inclusions under multi-thermal conditions. *Lithos*, 368–369, 105573. <https://doi.org/10.1016/j.lithos.2020.105573>

## SUPPORTING INFORMATION

Additional Supporting Information may be found online in the supporting information tab for this article.

Description

Figure S1. Xray element maps of garnet in retrogressed eclogite JB-18-50

Figure S2. Xray element maps of clinopyroxene in retrogressed eclogite JB-18-50

Figure S3. Xray element maps of amphibole and plagioclase in retrogressed eclogite JB-18-50

Figure S4. P-MH<sub>2</sub>O diagram for eclogite JB-18-50 and T-MH<sub>2</sub>O diagram for metasediment JB-18-46, computed with the same bulk composition as diagrams on Figure 8 (main text). Modal proportions (vol%) of hornblende and biotite are displayed on the right.

Figure S5. P-T diagram with mineral isopleths for the prograde stage in the eclogites

Figure S6. P-T diagram with mineral isopleths for the retrorade stage in the eclogites

Figure S7. P-T diagram with mineral isopleths for the migmatitic metasediment

Table S1. Abbreviations used for mineral end-members

Table S2. Mineral EPMA data for the retrogressed eclogites and metasediment JB-18-46. (a) Garnet; - (b) Clinopyroxene; - (c) Amphibole; (d) Feldspar

Table S3. Settings and solution models used in PerpleX to compute the phase diagrams

Table S4. Observed mineral proportions (vol%)

Table S5. Summary of rutile analyses and zircon-in-rutile temperatures calculated with the calibration of Tomkins et al. (2007)

Table S6. Summary of trace element analyses in zircon, with Ti-in-zircon temperatures calculated with the calibration of Ferry and Watson (2007)

Table S7. SIMS U-Pb analyses of zircon in eclogites

Table S8. SIMS U-Pb analyses of zircon in metasediment

Table S9. LA-ICPMS U-Pb analyses of rutile

## **FIGURES AND TABLE CAPTIONS**

Figure 1. (a) Tectonic map of the Variscan belt of Europe, with marked the main position of the External Crystalline Massifs (ECM) and the main exposures of HP rocks (dots). (b) Geological map of the Paleozoic basement in the External Crystalline massifs, with marked the main locations where

HP rocks are exposed (red stars). modified from Guillot & Ménot (2009).

Figure 2. (a) Geological map of the studied area (modified from Gros (1974), showing the direction of planar structures and relationship between the early metamorphic foliation Sx and the steep S2 fabric. Position of the interpretative profile is also indicated. (b) Structural cross section showing the deformation in the metamorphic basement and its relationship with the Mesozoic cover.

Figure 3. Field photographs illustrating typical structural features of the early metamorphic foliation Sx. (a) - low angle open folds in Sx; (b) – East-verging P1 folds deforming Sx; (c) – Deformation of the early foliation Sx by D2 dextral shearing, resulting in the formation of a second S2 planar fabric; (d) - P1 upright fold

Figure 4. Field photographs illustrating typical structural features of the metamorphic foliation S2. (a) - Sx relics between S2 planes; (b) - contact between a leucocratic orthogneiss layer and migmatitic metasediments. The metasediments contain sheared leucosomes indicating a dextral strike-slip kinematics; (c)-(d) – S/C fabrics and P2 drag folds associated with D2 dextral shearing; (e) – preserved eclogitic boudin surrounded by foliated amphibolites; (f) – S2 fabrics in a deformed retrogressed eclogite. Hornblende growth is syn-D2, while garnet is ante-kinematic; (g) – L2 stretching lineation in a mylonitic orthogneiss.

Figure 5. Petrological features of the retrogressed eclogite samples JB-18-50 (a-g) and JB-18-03B (h-i). (a) – Scan image of a thin section of sample JB-18-50, which displays two textural domains; (i) a retrogressed coarse-grained domain and (ii) a fine-grained domain which preserved the relics of an eclogitic assemblage; (b) Microscope photograph in the fine-grained domain; (c) – Garnet grain containing numerous inclusions of quartz, omphacite and rutile. Rutile is partially resorbed and replaced by titanite; (d) - Backscattered electron image taken in the thin-grained eclogitic domain. Coarse grain omphacite is partially replaced by clinopyroxene-plagioclase-(hornblende) symplectites. Garnet contains numerous inclusions (see text for description); (e) – Xray map of grossular content in garnet, which shows the distinction between the Ca-poor inclusion-rich garnet core and the Ca-rich garnet rim. Additional Xray maps for other elements are available in the online supplements (Figures S1-3); (f) – Xray map of Na in clinopyroxene, which shows the distinction between coarse-grained

Na-rich omphacite and Na-poor augite in the symplectites; (g) – Backscattered electron image showing rutile grains in different textural positions, enclosed in garnet and in the matrix. Ilmenite and titanite developed at the expense of rutile during retrogression; (h) – Microscope photograph of the matrix in retrogressed eclogite sample JB-18-03B. Primary omphacite has almost been completely resorbed and replaced by the symplectites. Rutile is being replaced by titanite; – (i) Backscattered electron image of a garnet grain with large rutile inclusions.

Figure 6. Petrological features of the migmatitic metasediment JB-18-46. (a) Thin section scan of the migmatitic metasediment. The quartz-feldspar rich domain in the center is interpreted as a leucosome, and biotite-rich surrounding domains form the mesosome; (b) – Backscattered electron image of a garnet grains. Contrast has been increased to reveal internal zoning; (c) – Backscattered electron image of garnet containing inclusions of quartz and rutile; (d) – Backscattered electron image of a rutile grain in the matrix, which grows over ilmenite.

Figure 7. Mineral composition in the retrogressed eclogites and in the migmatitic metasediment.

Figure 8. Isochemical P-T phase diagrams computed with PerpleX for the prograde stage in the eclogites (a), the retrograde stage in the eclogites (b) and the metasediment (c); Gray tones represent the variance within each field. The P-T domain corresponding to the observed assemblage is highlighted with a bold line contour. T range obtained from Zr-in-Rutile thermometry is highlighted in purple.

Figure 9. Phase proportions computed with PerpleX for the P-T diagrams on Figure 8. Contour labels indicate the volume proportion (%) of the phase present in the system. Color scales also give a qualitative indication on the amount of the phase stable (the darker the tone, the greater amount of the phase). On each panel, the P-T domain corresponding to the observed assemblage is highlighted with a bold line contour.

Figure 10. Misfit  $\delta(P,T)$  between observed and predicted mineral composition for the P-T phase diagrams on Figure 8. Yellow corresponds to good fit with the measured composition, blue to poor fit. On each panel, the P-T domain corresponding to the observed assemblage is highlighted with a bold line contour. EP: Eclogite Prograde (Figure 8-a); ER: Eclogite Retrograde (Figure 8-b); MS: Metasediment (Figure 8-c). End-members considered in the calculation are given in Table S3 in the online supplements

Figure 11. Distribution of Zr concentration measured in rutile (a) and Ti-in-zircon and Zr-in-rutile temperatures (b), estimated with the calibration of Ferry & Watson (2007) for zircon and Tomkins et al. (2007) for rutile. Eclogites are figured with green tones, and the metasediment in orange.

Considering the calibration uncertainty of the Zr-in-rutile thermometer ( $\pm 30^\circ\text{C}$ ), the calculated T are indistinguishable for the different populations in the eclogites, which have therefore been merged together.

Figure 12. CC images of representative zircon grains separated from the retrogressed eclogites (a) and from the metasediment (b). (c) – Backscattered electron images of representative rutile grains separated from the retrogressed eclogites and analyzed for trace elements and U-Pb isotopes.

Figure 13. Th-U and REE composition of zircon cores and rims in both rock types. (a) – plots of Th vs U and  $(\text{Lu/Gd})_N$  vs Eu anomaly in analyzed zircon cores and rims. (b) – Chondrite normalized patterns for REE in zircon. The color scale indicates the common Pb corrected  $^{206}\text{Pb}/^{238}\text{U}$  date obtained by SIMS dating of the same domain.

Figure 14. Summary of U-Pb analyses in zircon and rutile plotted on Wetherill and Terra-Wasserburg (ratios uncorrected for common Pb) diagrams using the IsoplotR R package (Vermeesch, 2018); (a)–(b) – eclogite zircon cores; (c),(d),(f) – eclogite zircon rims; (g) – metasediment; (e),(h) – probability distribution and histogram of  $^{206}\text{Pb}/^{238}\text{U}$  dates in zircon rims from eclogite JB-19-01 (e) and metasediment JB-18-46 (h); (i) – rutile from the retrogressed eclogite JB-18-03B. In the Terra-Wasserburg diagram of (c), the regression is forced to the  $^{207}\text{Pb}/^{206}\text{Pb}$  value of present-day common Pb according to Stacey & Kramers (1975). Analyses excluded from age calculation are shown with dotted contours.

Figure 15. Possible P-T evolution for the eclogitic lenses and the surrounding gneisses corresponding to the three presented scenarios. See discussion in text.

Table 1. List of collected samples, with summary of age and P-T data

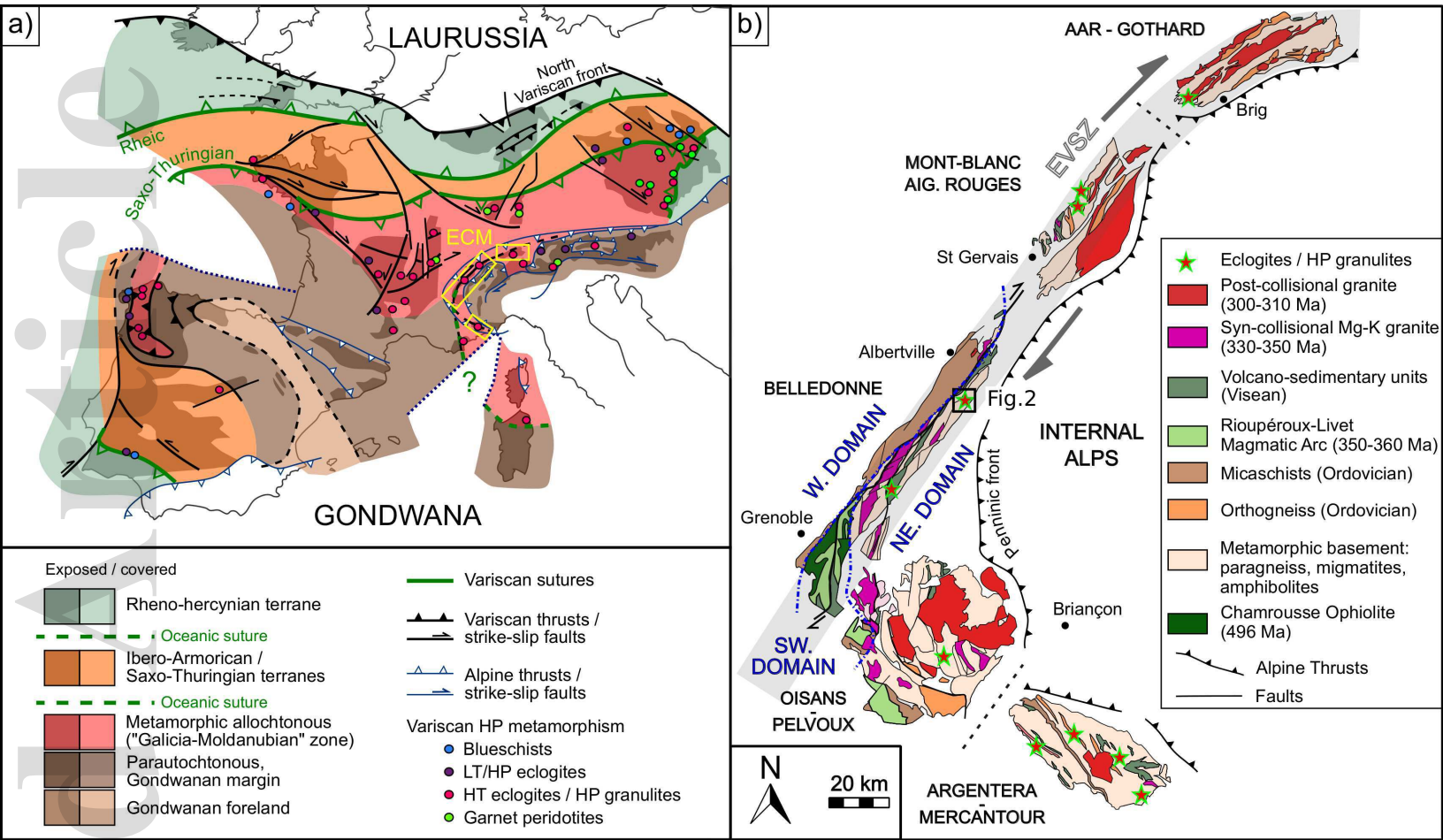
Sample	JB-18-03 (A-F)	JB-18-06	JB-18-49	JB-19-01	JB-19-02	JB-18-50	JB-18-46
Lithology	Retrogressed Eclogites						Migmatitic Metasediment
Field Relations	Core of an eclogite boudin	Core of an eclogite boudin	Core of an eclogite boudin	not in place	not in place	Core of an eclogite boudin	Border of the large Amphibolitic lense

Coordinates WGS84	Long °	6.53014	6.53072	6.52928	6.52928	6.53014	6.52928	6.52975
	Lat °	45.62189	45.62250	45.62131	45.62131	45.62189	45.62131	45.62069
	Alt (m)	2026	2066	2051	2051	2026	2051	2013
Mineralogy		<b>I – eclogitic assemblage: Grt-1+Omp+Qtz+Rt (+Hbl)</b>  <b>II – HT amphibolitic / granulitic assemblage:</b> <b>Grt-2+Cpx-2+Hbl+Pl+Ilm/Ttn (+Rt)</b>  <b>III – retromorphic greenschist assemblage:</b> <b>Act+Ep+Chl+Ab+Ttn</b>  <b>Accessory minerals: Zrc, Ap</b>						<b>Main Assemblage:</b> <b>Qtz+Pl+Bt</b> <b>+Grt+Rt+Ilm</b>  <b>Accessory Minerals:</b> <b>Ap, Zrc, Mnz</b>
U-Pb ages (Ma)	Zrc core	-	-	-	448 ± 6	456 ± 4	-	-
	Zrc rim	-	-	311 ± 7	314-335	-	332 ± 19	317-343 305 ± 3
	Rt	340 ± 11	-	-	-	-	-	-
P-T Estimates	Prograde	-	-	-	-	-	-	0.8-1.1 GPa 600-700 °C
	Peak P	-	-	-	-	-	>1.4 GPa 690-740 °C	Same as peak T
	Peak T	-	-	-	-	-	0.8-1.4 GPa 700-800 °C	1.1-1.4 GPa 700-780 °C

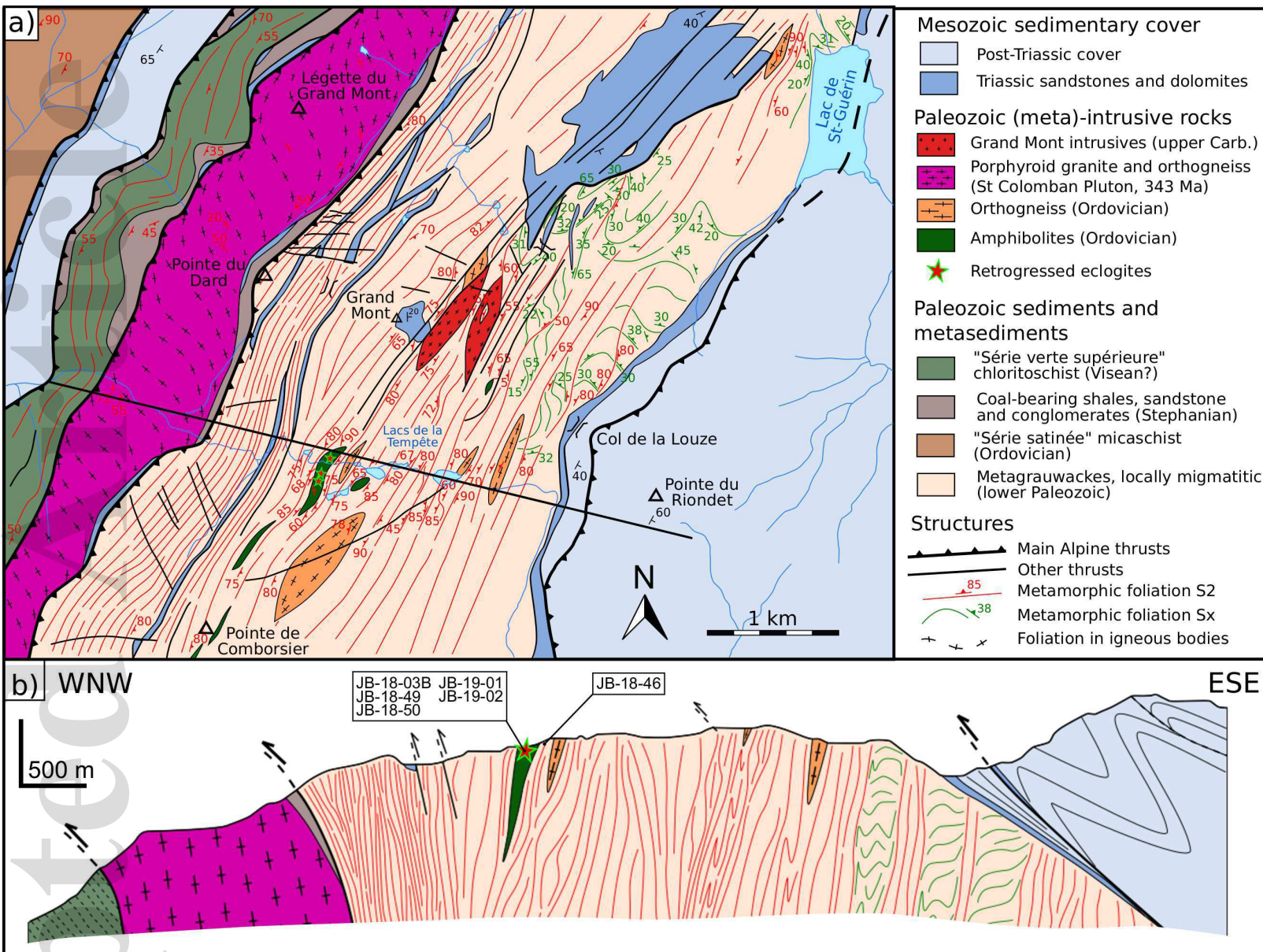
Table 2. Bulk compositions measured by ICP-OES on the bulk rock and determined by re-integration of electron microprobe analyses on a local domain, in oxide weight %. Compositions used as input in PerpleX are given below in oxide mole %.

Sample	JB-18-50	JB-18-50	JB-18-50	JB-18-46
Domain	Bulk rock	Microdomain (Fig.5-a)	Microdomain (Fig.5-a) Without Grt1	Bulk rock
Method	ICP-OES	EPMA	EPMA	ICP-OES
Measured compositions (wt %)				
SiO <sub>2</sub>	48.85	46.79	49.91	62.34
TiO <sub>2</sub>	1.95	1.15	1.58	0.96
Al <sub>2</sub> O <sub>3</sub>	13.47	14.84	12.52	15.10
FeO	13.61	14.65	10.61	7.09
MnO	0.26	0.30	0.21	0.13
MgO	6.60	6.50	7.15	3.78
CaO	11.00	13.49	14.99	2.67

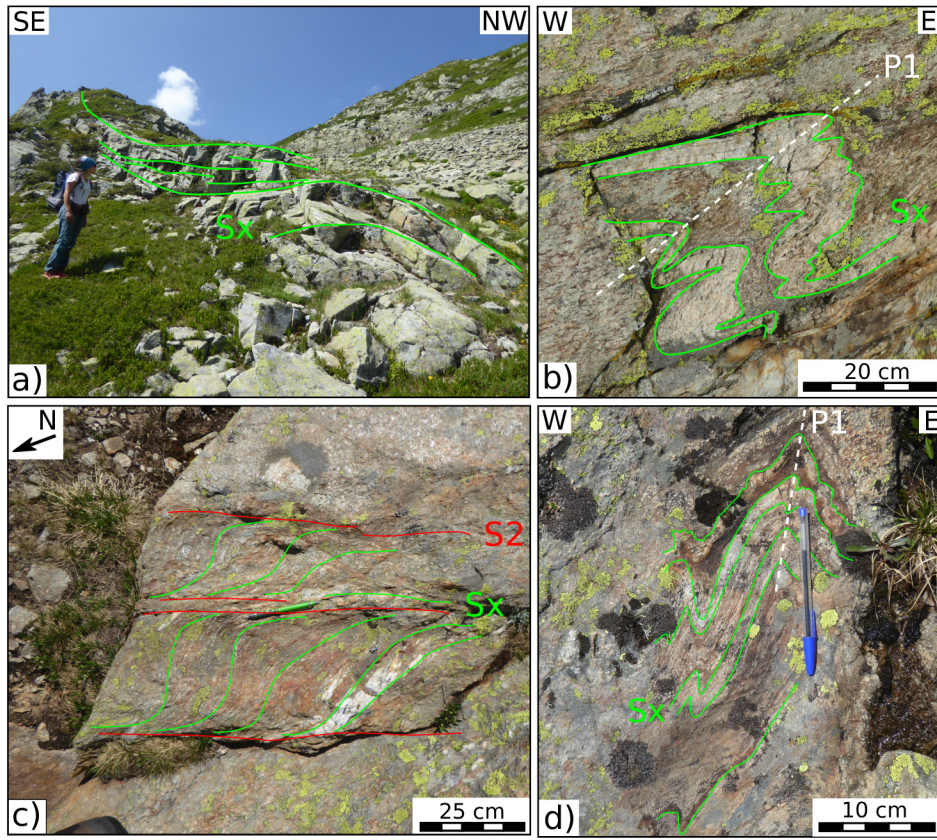
Na2O	2.13	2.18	2.95	2.55
K2O	0.28	0.08	0.08	2.67
P2O5	0.14	not analyzed	not analyzed	0.18
L.O.I.	0.32	not analyzed	not analyzed	1.50
Total	98.61	99.99	100.00	98.97
	Perplex input (mol%)			
SiO2	-	49.14	51.22	65.11
TiO2	-	0.91	1.22	0.75
Al2O3	-	9.18	7.57	9.29
FeO	-	12.87	9.11	6.19
MnO	-	excluded	excluded	0.11
MgO	-	10.18	10.94	5.89
CaO	-	15.18	16.48	2.99
Na2O	-	2.22	2.94	2.58
K2O	-	excluded	excluded	1.78
P2O5	-	excluded	excluded	excluded
H2O	-	excess	0.80	3.50
O2	-	0.15	0.15	excluded



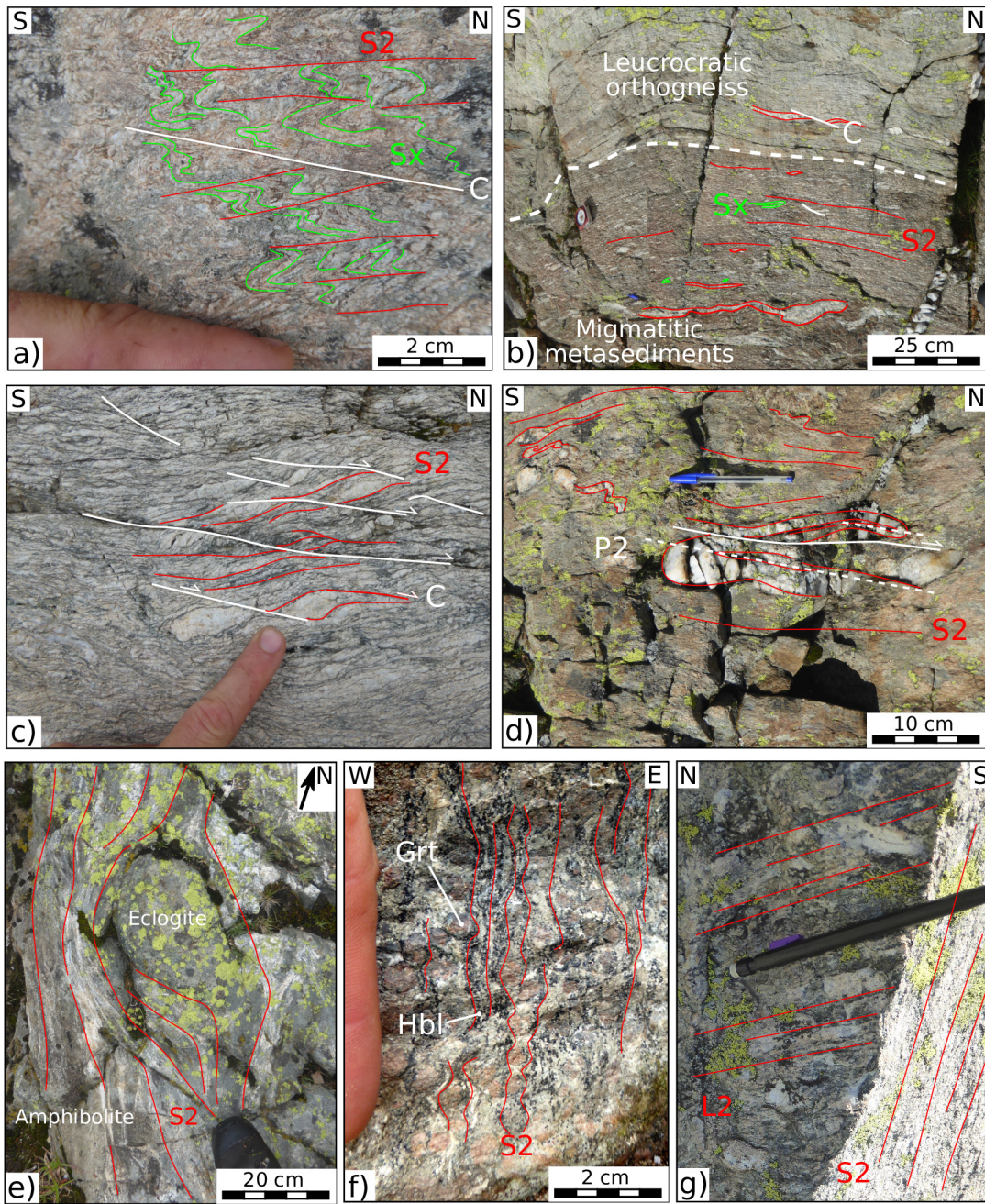
jmg\_12600\_f1.eps



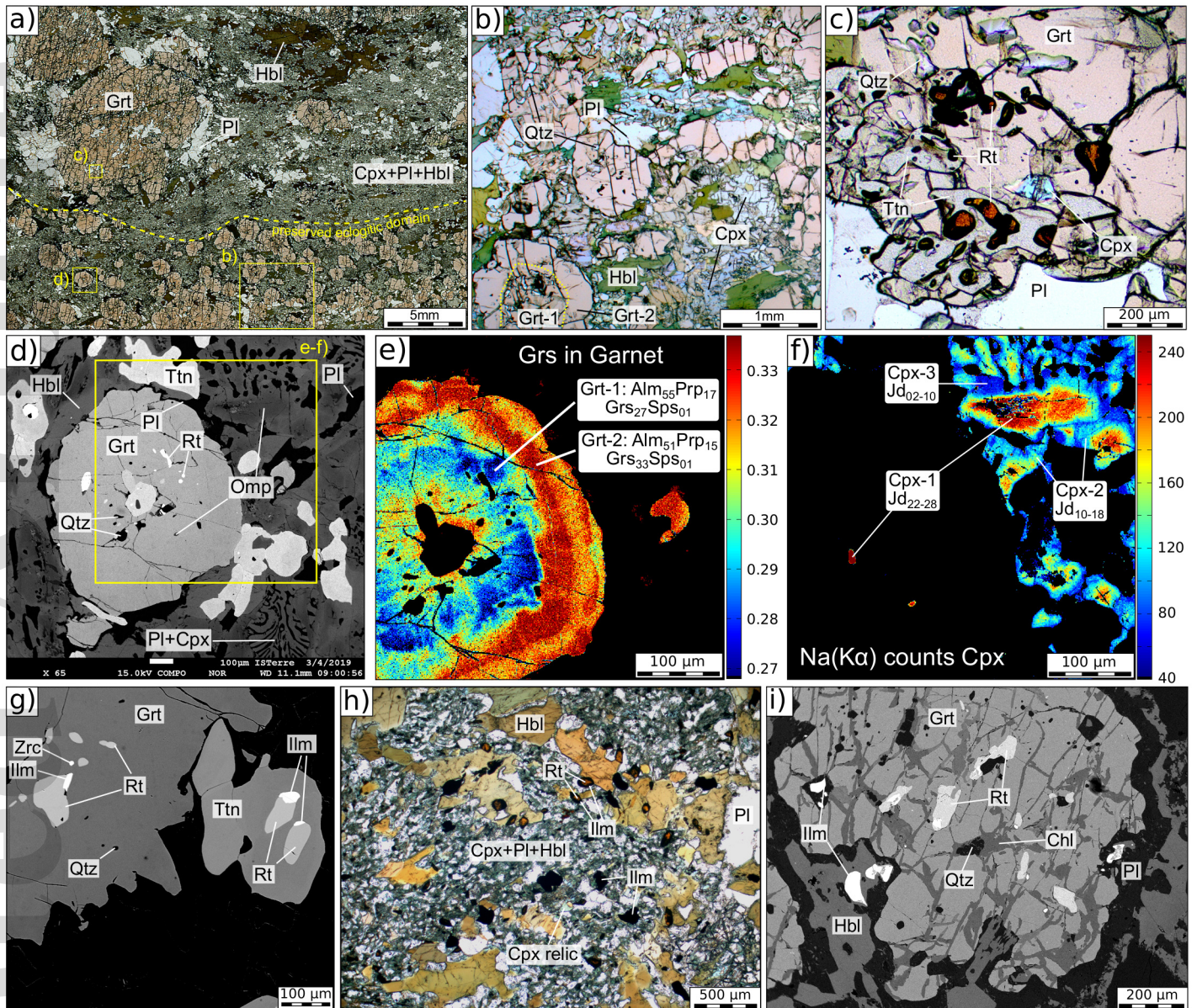
jmg\_12600\_f2.eps



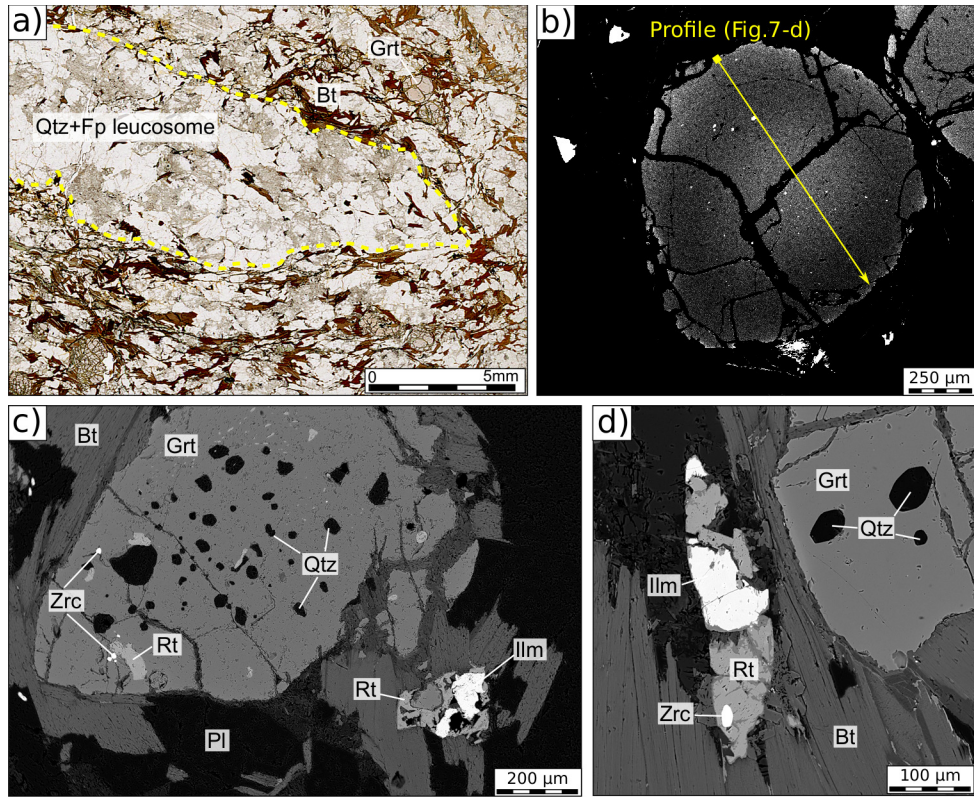
jmg\_12600\_f3.tif



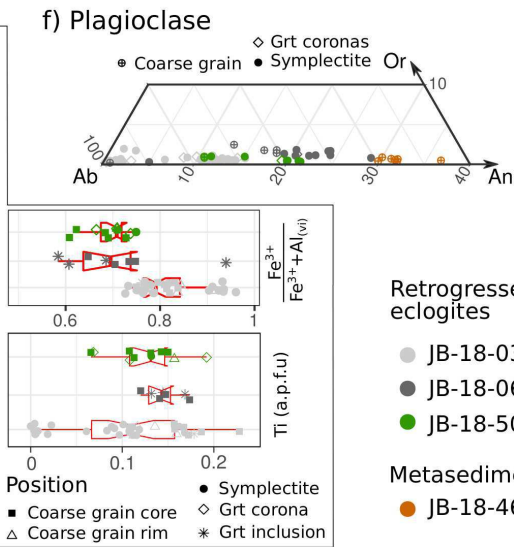
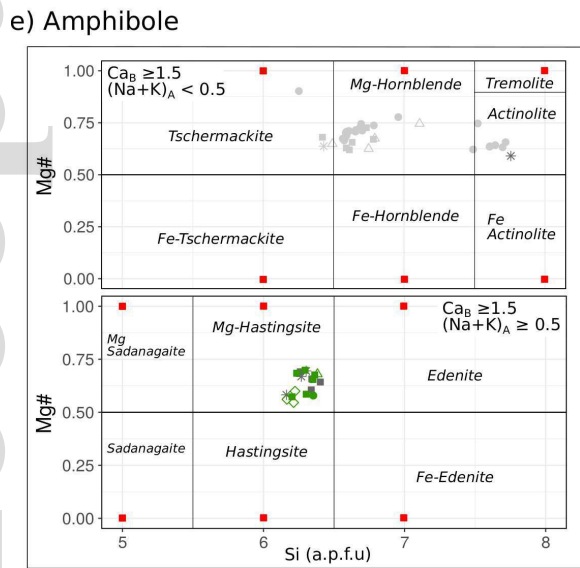
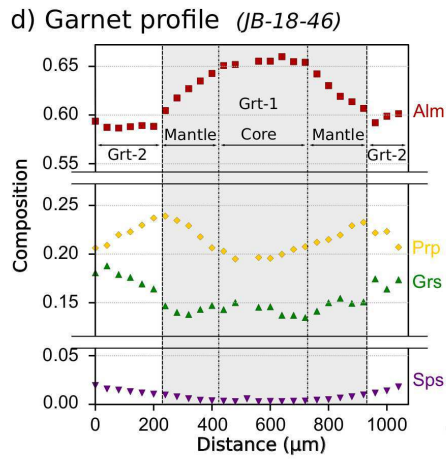
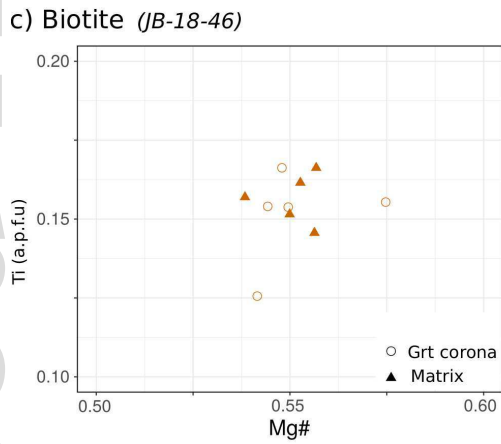
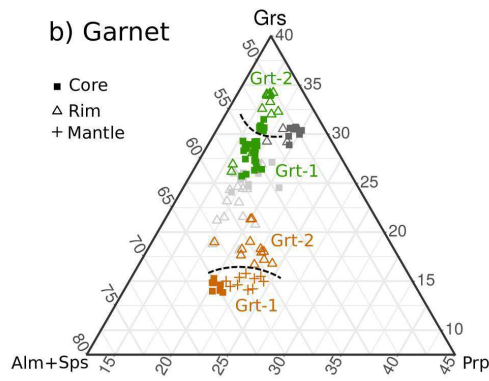
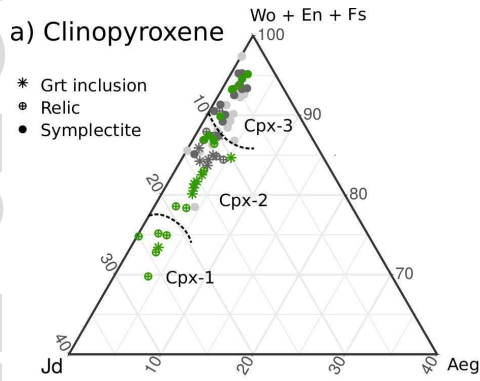
jmg\_12600\_f4.tif



jmg\_12600\_f5.tif

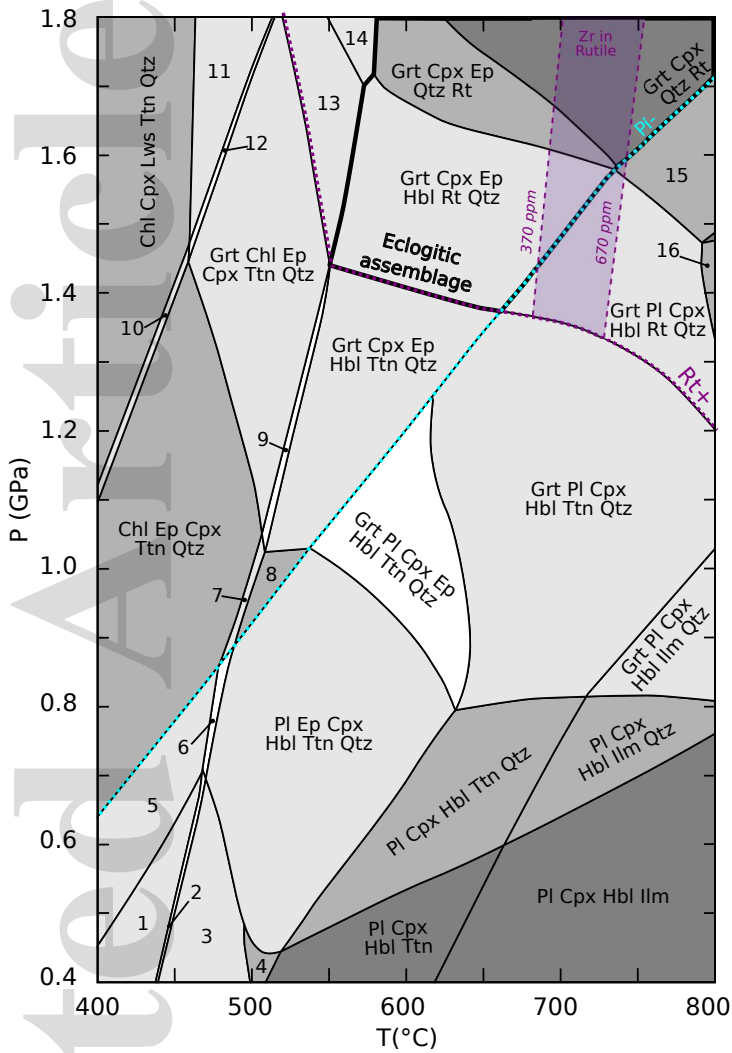


jmg\_12600\_f6.tif



- Retrogressed eclogites**
- JB-18-03(A-F)
  - JB-18-06
  - JB-18-50
- Metasediment**
- JB-18-46

a) Eclogite - Prograde (H<sub>2</sub>O saturated)



a) Eclogite prograde

- 1 - Pl Chl Ep Act Cpx Ttn
- 2 - Pl Chl Ep Act Hbl Cpx Ttn
- 3 - Pl Ep Act Hbl Cpx Ttn
- 4 - Pl Ep Cpx Hbl Ttn
- 5 - Pl Chl Ep Cpx Ttn Qtz
- 6 - Pl Chl Ep Cpx Hbl Ttn Qtz
- 7 - Chl Ep Cpx Hbl Ttn Qtz
- 8 - Ep Cpx Hbl Ttn Qtz
- 9 - Grt Chl Ep Hbl Cpx Ttn Qtz
- 10 - Chl Ep Cpx Lws Ttn Qtz
- 11 - Grt Chl Cpx Lws Ttn Qtz
- 12 - Grt Chl Ep Cpx Lws Ttn Qtz
- 13 - Grt Chl Ep Cpx Rt Qtz
- 14 - Grt Chl Tlc Ep Cpx Rt Qtz
- 15 - Grt Pl Cpx Rt Qtz
- 16 - Grt Pl Cpx Hbl Rt

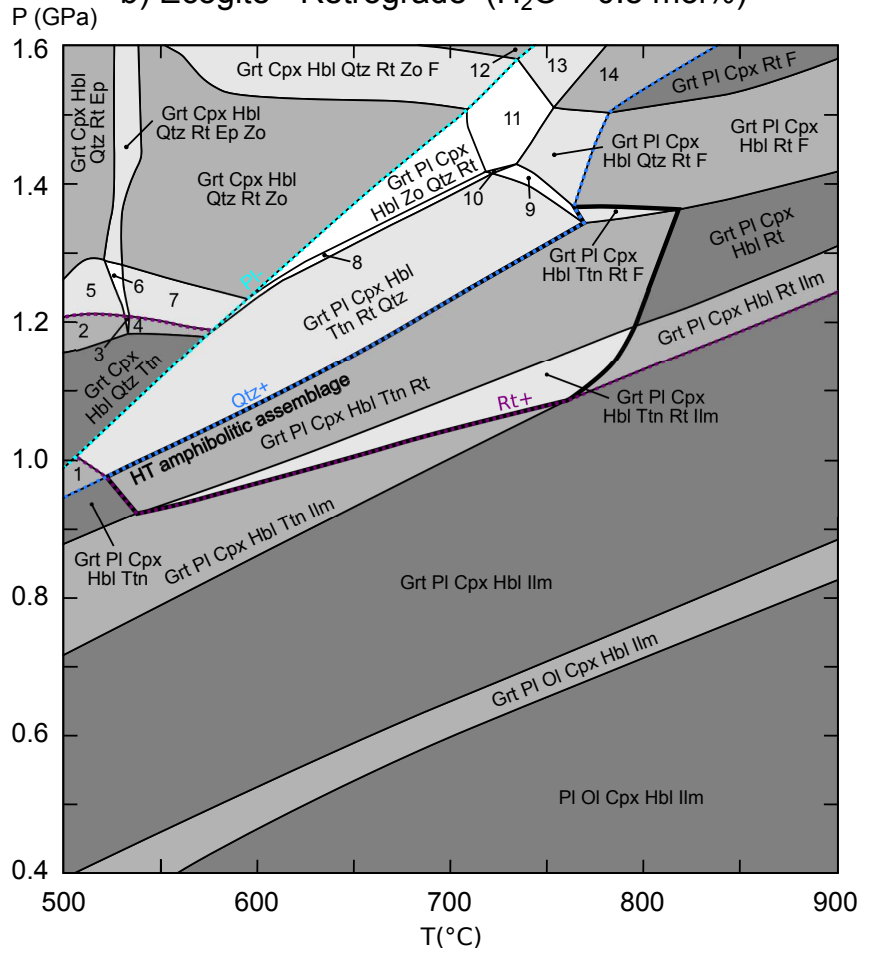
b) Eclogite retrograde

- 1 - Grt Pl Cpx Hbl Ttn Qtz
- 2 - Grt Cpx Hbl Qtz Ttn Ep
- 3 - Grt Cpx Hbl Qtz Ttn Ep Zo
- 4 - Grt Cpx Hbl Qtz Ttn Zo
- 5 - Grt Cpx Hbl Qtz Ttn Rt Ep
- 6 - Grt Cpx Hbl Qtz Ttn Rt Ep Zo
- 7 - Grt Cpx Hbl Qtz Ttn Rt Zo
- 8 - Grt Pl Cpx Hbl Zo Ttn Qtz Rt
- 9 - Grt Pl Cpx Hbl Ttn Qtz Rt F
- 10 - Grt Pl Cpx Hbl Zo Ttn Qtz Rt F
- 11 - Grt Pl Cpx Hbl Zo Qtz Rt F
- 12 - Grt Cpx Zo Qtz Rt F
- 13 - Grt Pl Cpx Qtz Rt Zo F
- 14 - Grt Pl Cpx Qtz Rt F

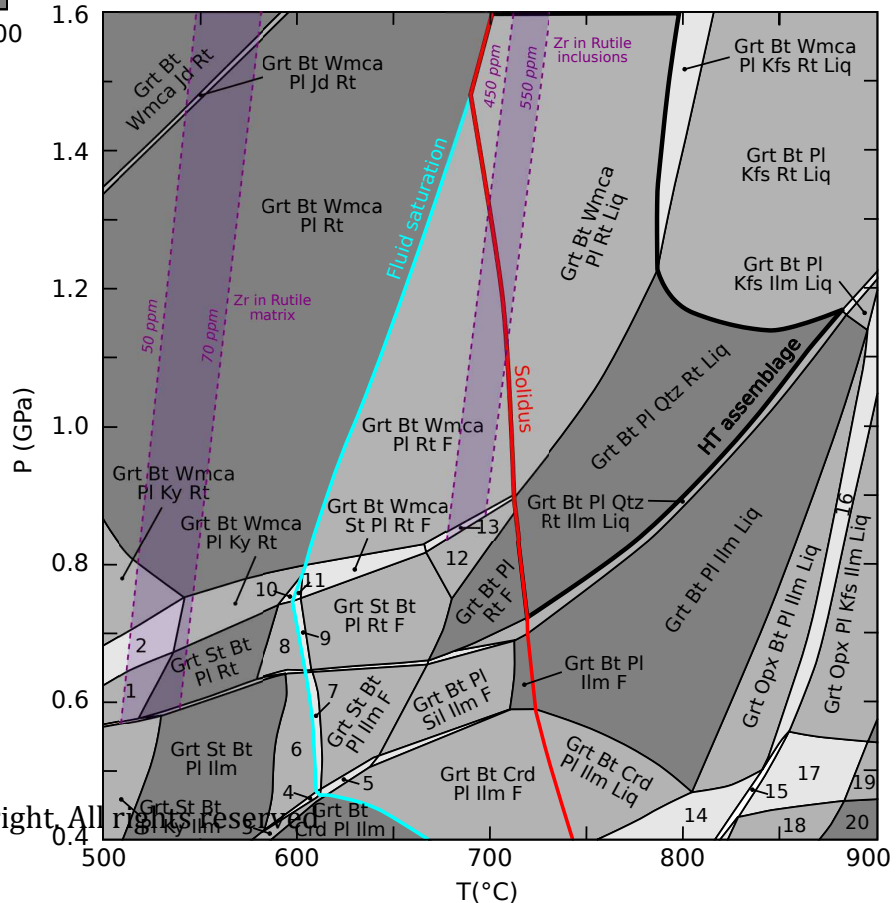
c) Metasediment

- 1 - Grt St Bt Pl Ky Rt
- 2 - Grt St Bt Wmca Pl Ky Rt
- 3 - Grt St Bt Crd Pl Ilm
- 4 - Grt St Bt Chl Crd Pl Ilm
- 5 - Grt St Bt Crd Pl Ilm F
- 6 - Grt St Bt Chl Pl Ilm
- 7 - Grt St Bt Chl Pl Ilm F
- 8 - Grt St Bt Chl Pl Rt
- 9 - Grt St Bt Chl Pl Rt F
- 10 - Grt St Bt Chl Wmca Pl Rt
- 11 - Grt St Bt Chl Wmca Pl Rt F
- 12 - Grt Ky Bt Pl Rt F
- 13 - Grt Ky Bt Pl Wmca Rt F
- 14 - Grt Opx Bt Crd Pl Ilm Liq
- 15 - Grt Opx Bt Crd Pl Kfs Ilm Liq
- 16 - Grt Opx Bt Pl Kfs Ilm Liq
- 17 - Grt Opx Crd Pl Kfs Ilm Liq
- 18 - Opx Crd Pl Kfs Ilm Liq
- 19 - Grt Opx Crd Kfs Ilm Liq
- 20 - Opx Crd Kfs Ilm Liq

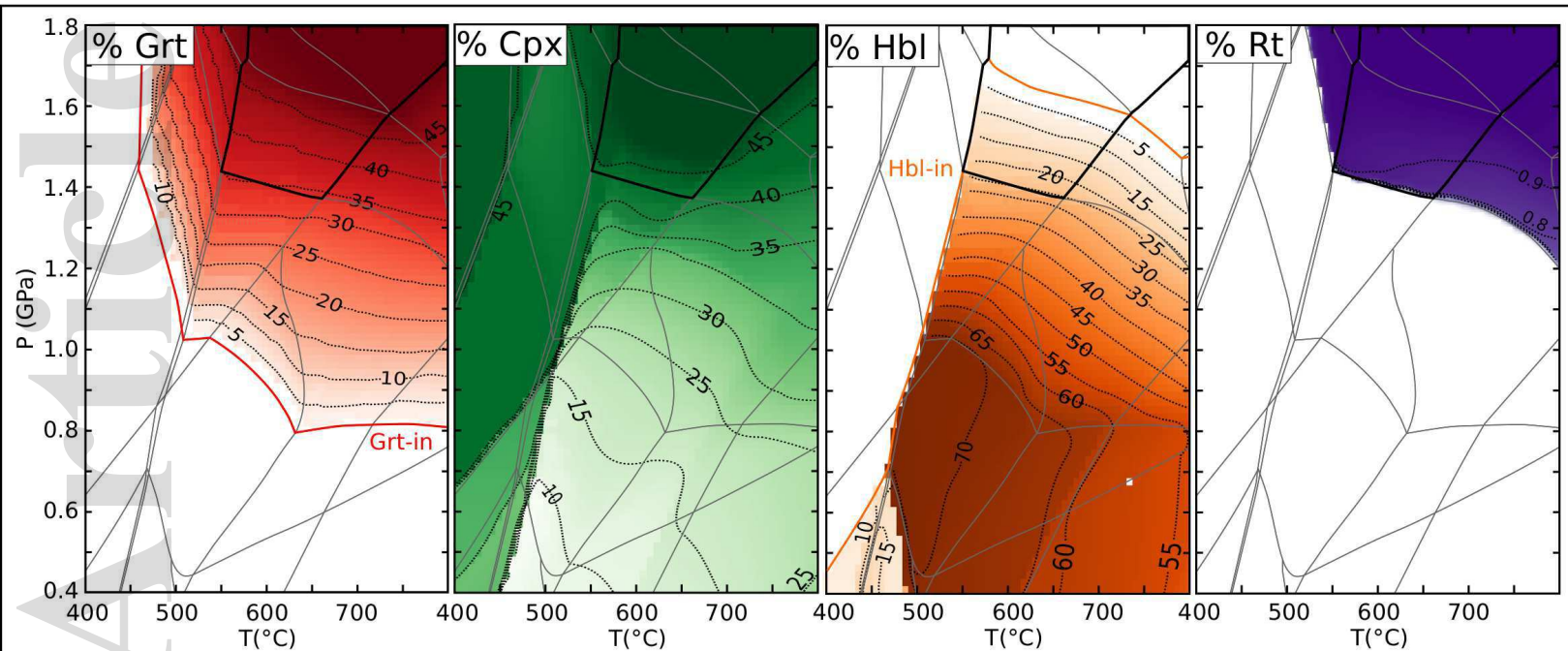
b) Eclogite - Retrograde (H<sub>2</sub>O = 0.8 mol%)



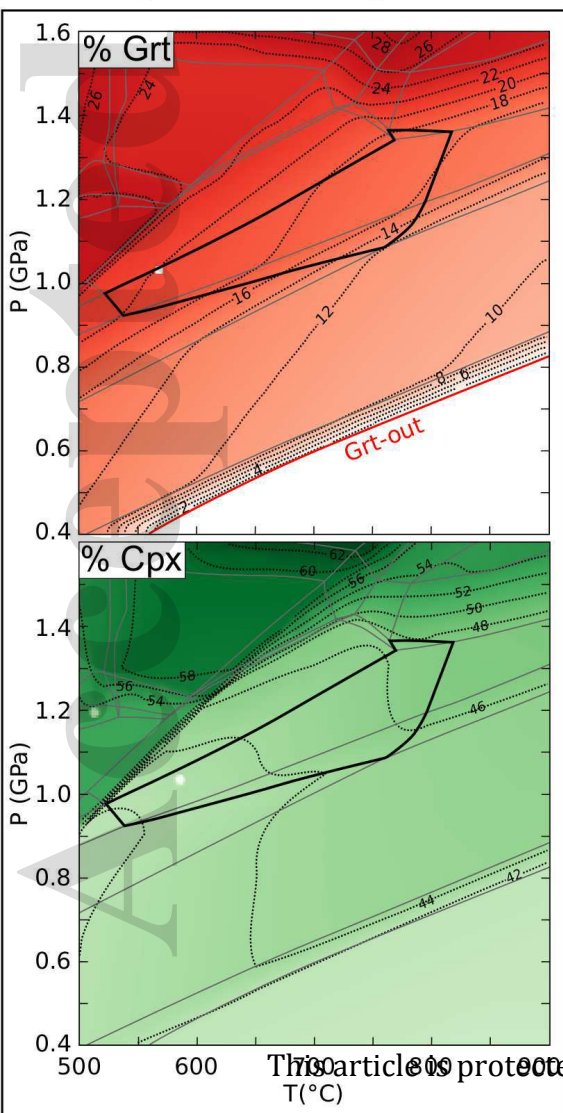
c) Metasediment (Qtz saturated, H<sub>2</sub>O = 3.5 mol%)



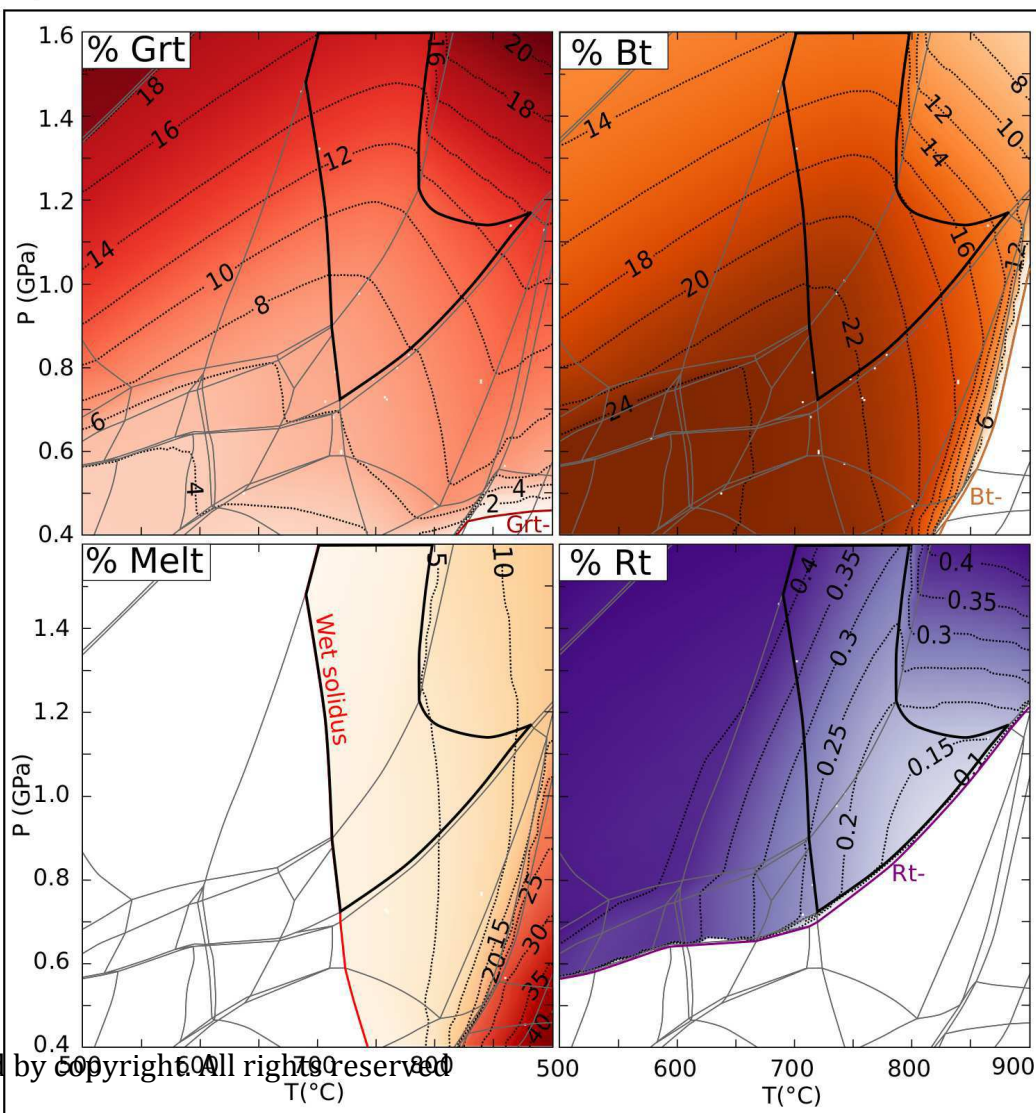
a) Eclogite - Prograde



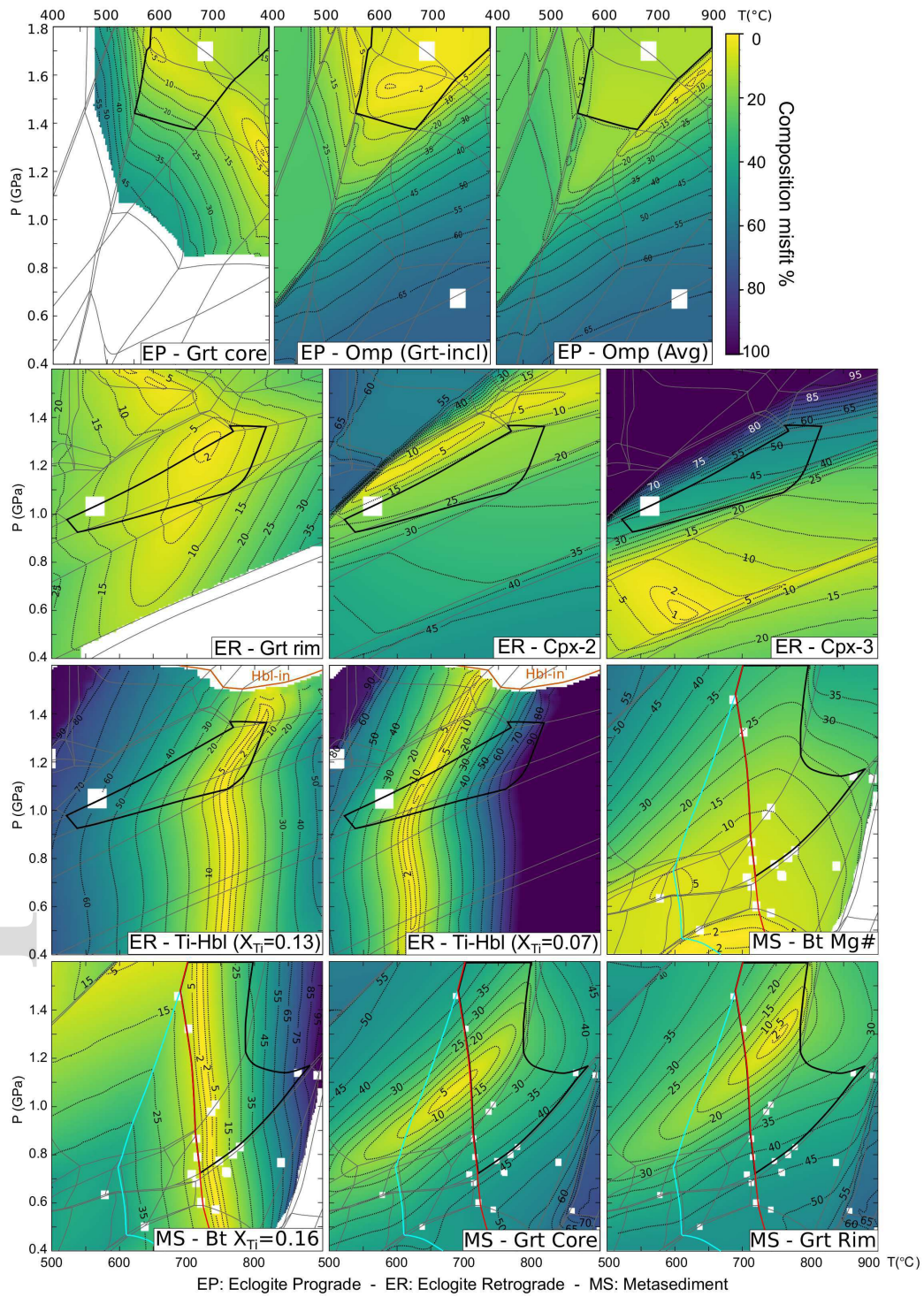
b) Eclogite - Retrograde

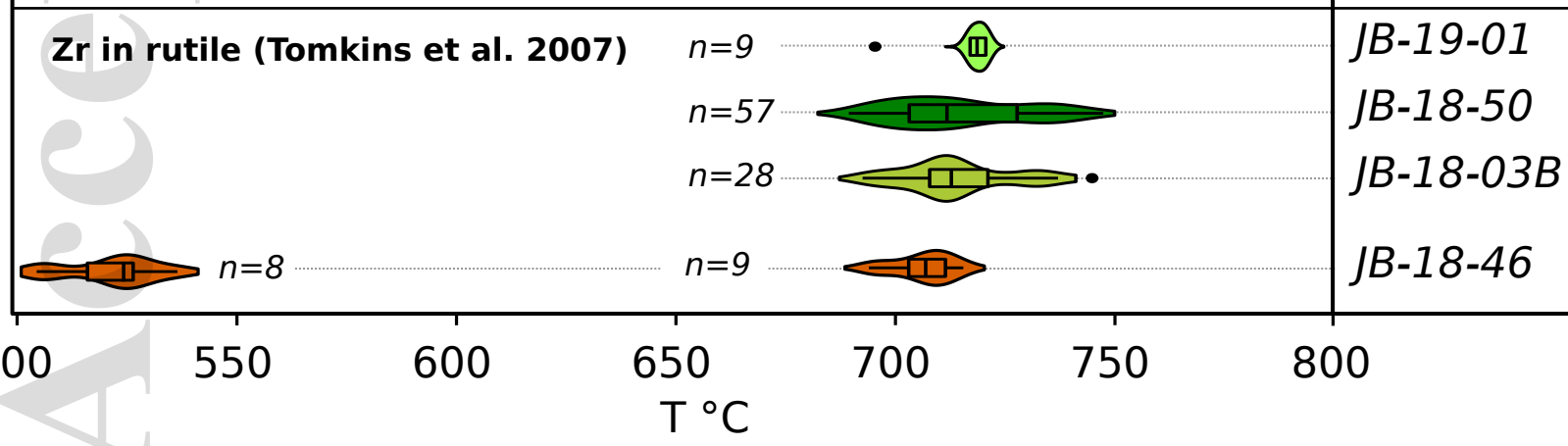
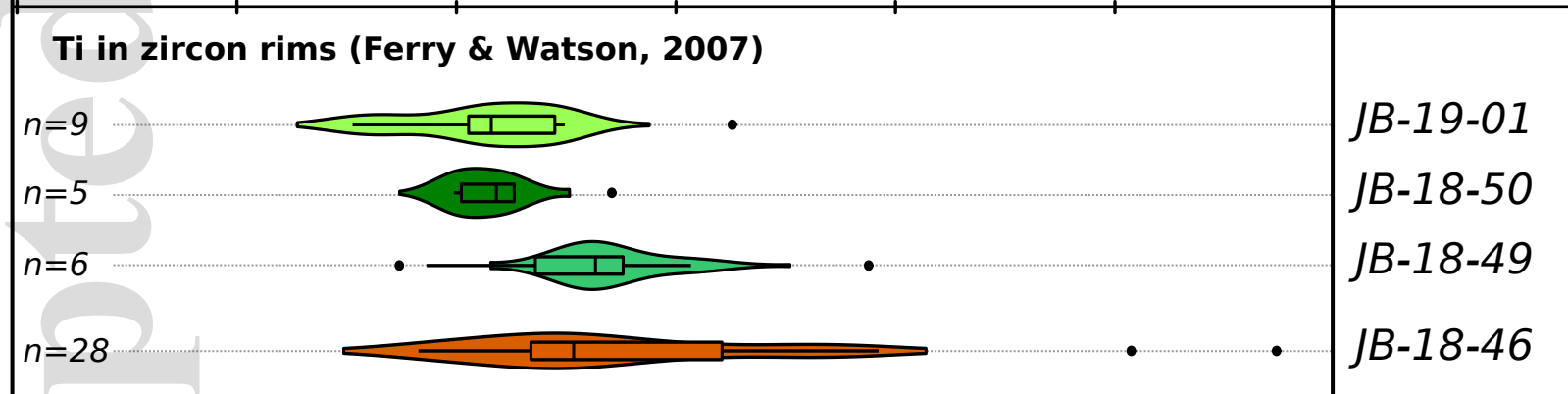
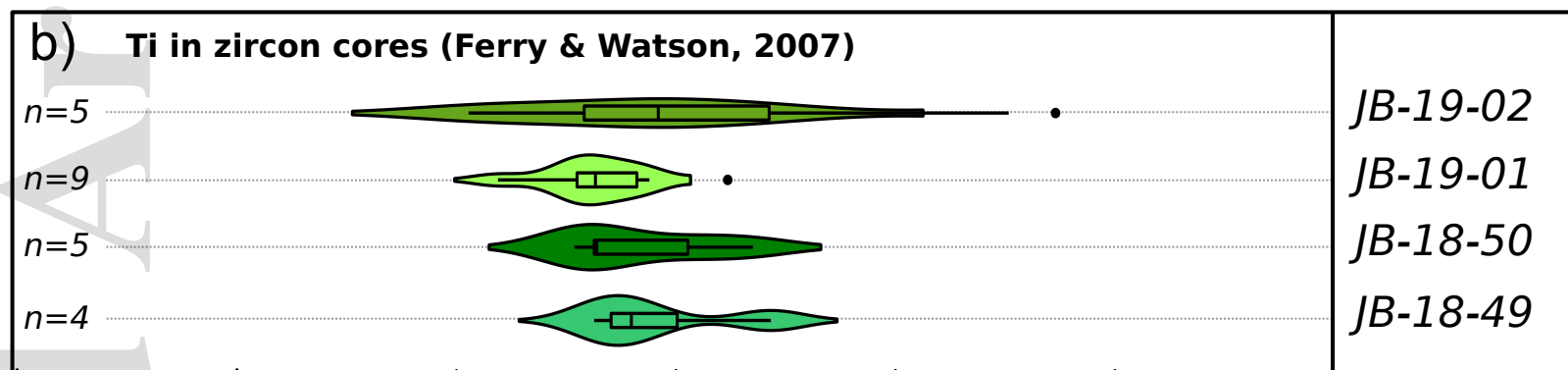
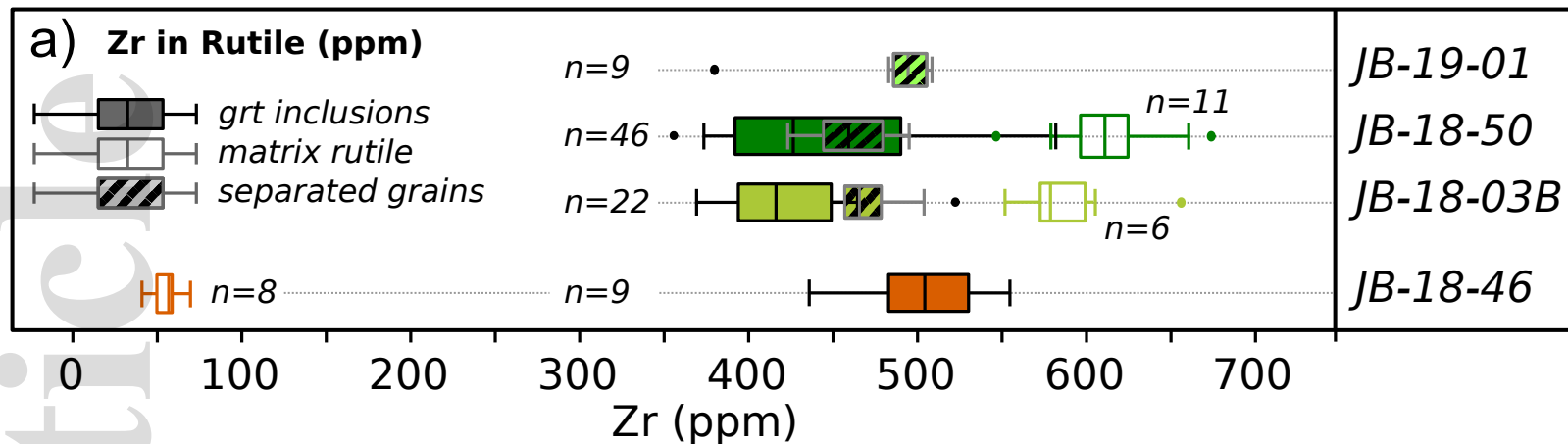


c) Metasediment

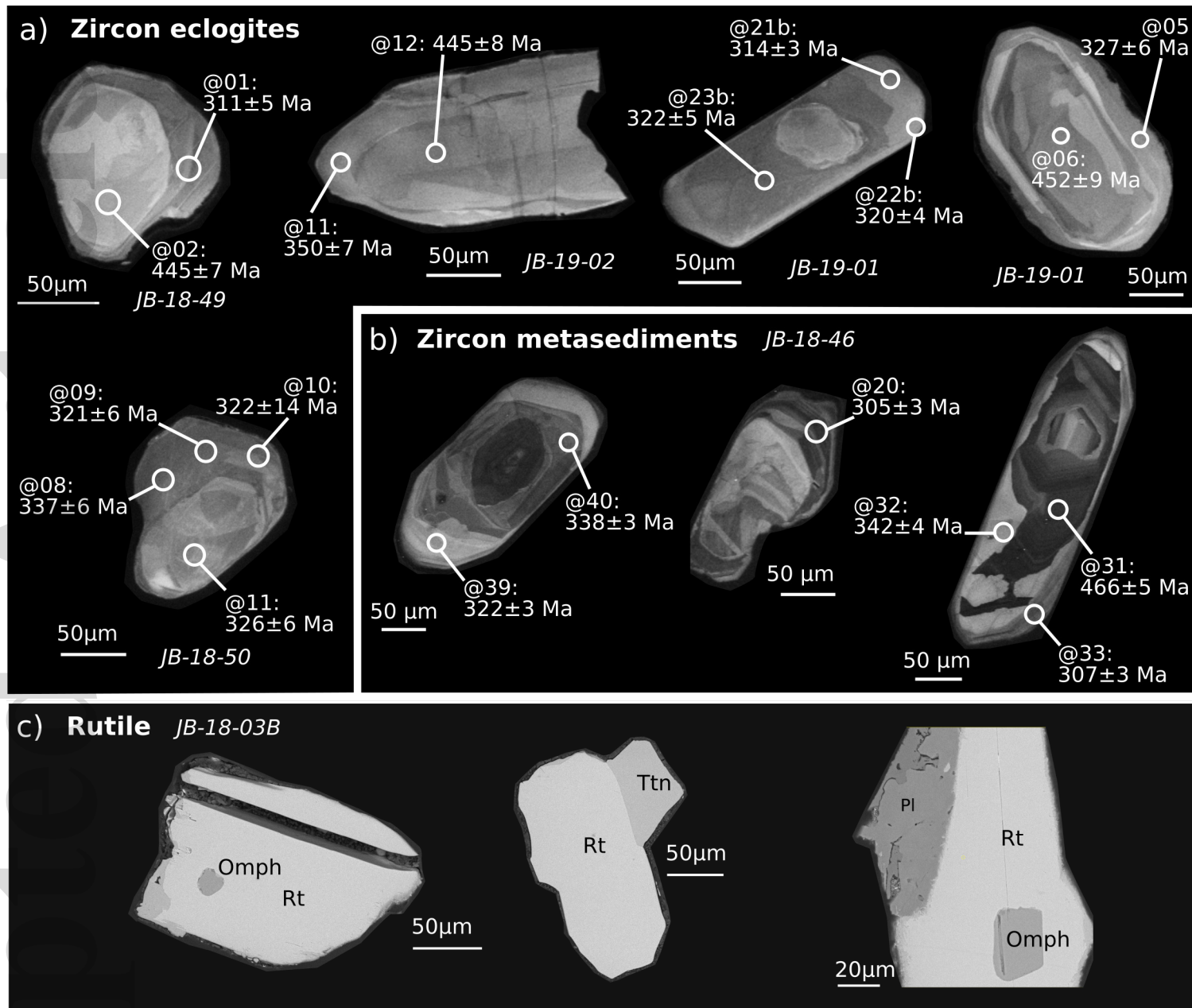


This article is protected by copyright. All rights reserved.



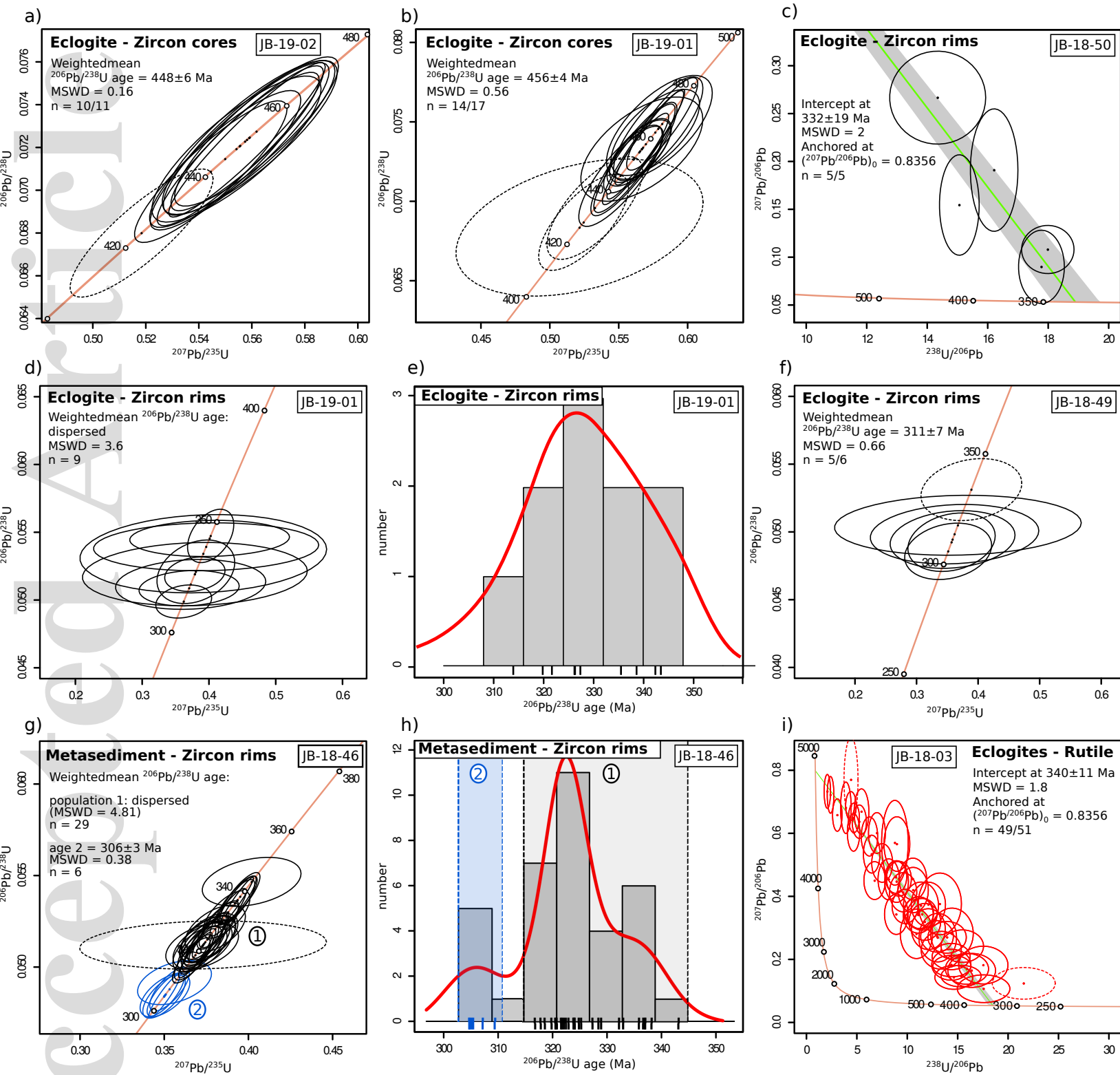


jmg\_12600\_f11.eps



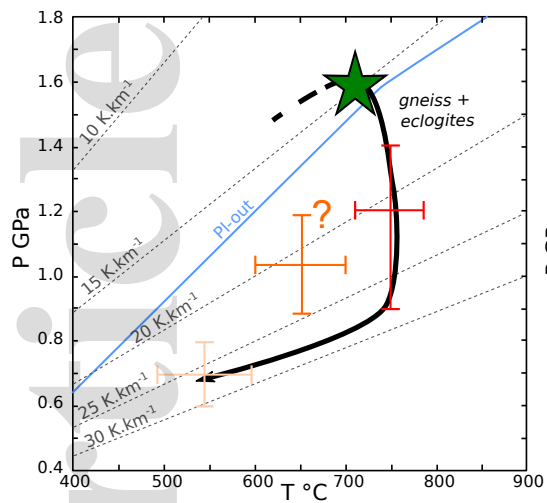
jmg\_12600\_f12.tif



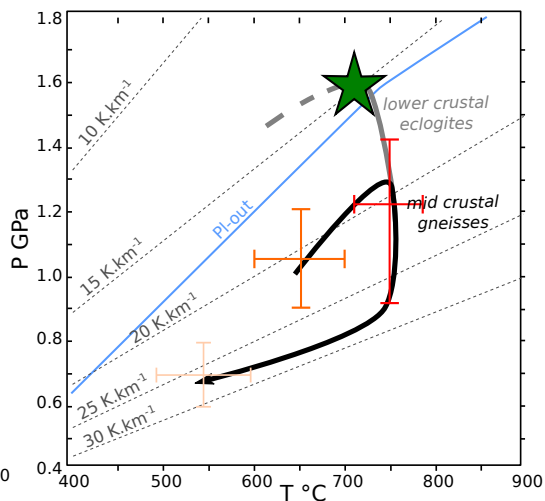


jmg\_12600\_f14.eps

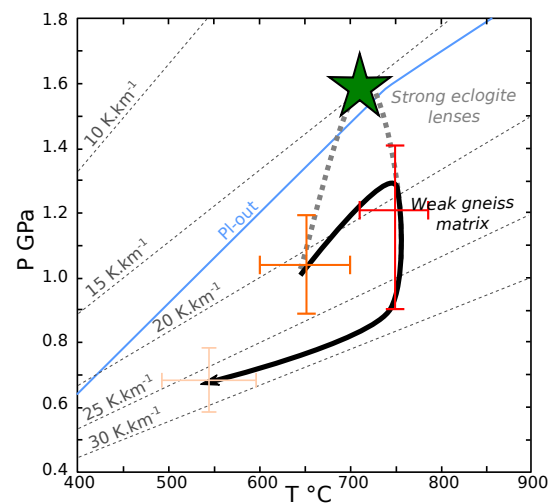
Scenario 1: obliteration of HP assemblage



Scenario 2: tectonic *mélange*



Scenario 3: tectonic overpressure



jmg\_12600\_f15.eps

Accepted Article